



**HAL**  
open science

# Fast-charging of Lithium-ion batteries with ohmic-drop compensation method

Mohd Hilmi Noh

► **To cite this version:**

Mohd Hilmi Noh. Fast-charging of Lithium-ion batteries with ohmic-drop compensation method. Electric power. Université Grenoble Alpes, 2017. English. NNT : 2017GREAI076 . tel-01718584

**HAL Id: tel-01718584**

**<https://theses.hal.science/tel-01718584>**

Submitted on 27 Feb 2018

**HAL** is a multi-disciplinary open access archive for the deposit and dissemination of scientific research documents, whether they are published or not. The documents may come from teaching and research institutions in France or abroad, or from public or private research centers.

L'archive ouverte pluridisciplinaire **HAL**, est destinée au dépôt et à la diffusion de documents scientifiques de niveau recherche, publiés ou non, émanant des établissements d'enseignement et de recherche français ou étrangers, des laboratoires publics ou privés.

## THÈSE

Pour obtenir le grade de

**DOCTEUR DE L'UNIVERSITÉ GRENOBLE ALPES**

Spécialité: MEP : Mécanique des fluides Energétique, Procédés

Arrêté ministériel : 25 mai 2016

Présentée par

**Mohd Hilmi NOH**

Thèse dirigée par **Yann BULTEL**, Professeur, Grenoble INP,  
et codirigée par **Pierre Xavier THIVEL**, Maître de conférences,  
Université Grenoble Alpes et **Christine LEFROU**, Maître de  
conférences, Grenoble INP.

préparée au sein du **Laboratoire d'Electrochimie et de Physico-  
Chimie des Matériaux et des Interfaces.**

dans l'**École Doctorale Ingénierie - Matériaux, Mécanique,  
Environnement, Energétique, Procédés, Production.**

**Charge rapide de batteries Lithium-ion  
basée sur la compensation de chute-  
ohmique.**

***Fast-charging of Lithium-ion batteries with  
ohmic-drop compensation method.***

Thèse soutenue publiquement le **19 Octobre 2017**,  
devant le jury composé de :

**M. Christophe FORGEZ**

Professeur des Universités - Univ. Technologique de Compiègne, Rapporteur

**Mme. Corinne ALONSO**

Professeur des Universités - Univ. de Toulouse III Paul Sabatier, Rapporteur

**M. Pascal VENET**

Professeur des Universités - Univ. Claude Bernard Lyon 1, Examineur

**M. Yann BULTEL**

Professeur des Universités - Grenoble INP, Directeur de thèse

**M. Pierre-Xavier THIVEL**

Maître de Conférences - Univ. Grenoble Alpes, Co-directeur de thèse

**Mme. Christine LEFROU**

Maître de Conférences - Grenoble INP, Co-directeur de thèse





*To my wife, my children and my family,*

*Love you all to the last breath!*

*“There is no beauty better than intellect”*

***Muhammad PBUH***



## Acknowledgement

Firstly, I would like to express my sincere gratitude to all of my supervisors Prof. Yann BULTEL, Pierre-Xavier THIVEL and Christine LEFROU for their continuous support of my Ph.D. study, for their patience, motivation, enthusiasm and immense knowledge. Their guidance helped me a lot throughout this research and writing of this thesis. I could not have imagined having better supervisors and mentors for my Ph.D. study. Without their precious support it would not be possible to conduct this research.

Besides my supervisors, I would like to thank the rest of my thesis committee: Christophe FORGEZ and Corinne ALONSO, for their insightful comments and encouragement, but also for the hard question which incited me to widen my research from various perspectives. My sincere thanks also goes to Pascal VENET who presided during the viva of this thesis.

I would also like to show my gratitude to Xavier FLEURY and Sylvie GENIES for their assistance and expertise in the post-mortem analysis studies of this research.

I would like to thank my fellow doctoral students for their feedback, cooperation and of course friendship. In addition I would like to express my gratitude to all hardworking people in LEPMI for giving such a good ambiance during these four years of research.

My thanks also goes to MARA (Majlis Amanah Rakyat), a Malaysian government agency for funding my scholarship to finish this research.

I am also grateful to all of my fellow Malaysians in France especially who live in Grenoble for giving me such a great and pleasant time throughout my stay in France.

Last but not the least, I must express my very profound gratitude to my parents and to my iron-lady wife, Nadzilahanim for providing me with unfailing support and continuous encouragement throughout my 12 years of study in France. Big hug also to all my little boys, Uthman, Zubayr and Yaseer for giving me the purpose to be a better person everyday personally and professionally. Special thanks also goes to my family-in-law for their understanding. This accomplishment would not have been possible without them.

Thank you



## Table of abbreviations and parameters

2D	Two dimensions
3D	Three dimensions
ACN	Acetonitrile
Al	Aluminum
C	Graphite
CC	Constant Current
CE	Coulombic Efficiency
CI	Current Interrupt method
$C_p$	Heat capacity at constant pressure
C-rate	Current rate relative to nominal capacity of the battery
Cu	Copper
CV	Constant Voltage
D	Diameter
DMC	Dimethyl carbonate
EC	Ethylene carbonate
EE	Energy Efficiency
EMC	Ethyl methyl carbonate
EoL	End of life
$e_{Sand}$	Total thickness of the jelly-roll sandwich
EV	Electric Vehicle
GC	Gaseous Chromatography
h	Height
$h$	Heat transfer coefficient
HEV	Hybrid Electric Vehicle
LAM	Loss of active materials

$L_c$	Characteristic dimension
LCO	Lithium Cobalt Oxide
LFP	Lithium Ferrous Phosphate
LLI	Loss of lithium inventory
LTO	Lithium Titanium Dioxide
$M_N$	Active material of negative electrode
$M_P$	Active material of positive electrode
MS	Mass spectrometry
MSD	Mass Selective Detector
NE	Negative electrode
NIST	National Institute of Standards
NMC	Nickel Manganese Cobalt oxide
OCV	Open Circuit Voltage
ODC	Ohmic Drop Compensation
PP	Positive electrode
SEI	Solid electrolyte interface
SEM	Scanning Electron Microscope
SOC	State Of Charge
SOH	State Of Health
$F$	Faraday constant
$I$	Battery cell current
$Nu$	Nusselt number
$Pr$	Prandtl number
$\dot{Q}_{in}$	Internal heat source of the battery
$\dot{q}_{in}$	Internal heat source generation per unit volume
$\dot{Q}_R$	Irreversible heat due to enthalpy change
$\dot{Q}_S$	Reversible heat due to entropy change

$Re$	Reynolds number
$R_i$	Internal resistance
$R_{Sand}$	Resistance of the jelly-roll sandwich
$S$	Lateral surface of the battery cell
$T$	Temperature
$T_a$	Environment temperature of the climatic chamber
$T_{radial}$	Cross-section temperature of the battery
$T_{surface}$	Surface temperature of the battery
$U$	Battery cell voltage
$U_f$	Upper-bound voltage limit (manufacturer)
$U'_f$	Upper-bound voltage limit (ODC method)
$U_{OCV}$	The voltage value of Open Circuit Voltage
$V$	Volume of the battery cell
$e$	Thickness of the materials
$m$	Mass of the battery cell
$n$	Number of mole
$\Delta_r G$	Free Gibbs energy
$\Delta_r H$	Enthalpy change
$\Delta_r S$	Entropy change
$\lambda$	Thermal conductivity
$\lambda_{eff}$	Effective thermal conductivity
$\xi$	Reaction progression (i.e. SOC progression)
$\rho$	Density
$\varphi$	Heat transfer flux
$\eta^{ohm}$	Over-potentials due to ohmic losses

## Contents

<b>Acknowledgement</b> .....	<b>5</b>
<b>Table of abbreviations and parameters</b> .....	<b>7</b>
<b>Contents</b> .....	<b>10</b>
<b>GENERAL INTRODUCTION</b> .....	<b>13</b>
<b>CHAPTER 1: LI-ION BATTERY; PRESENTATION, OPERATION, FAST-CHARGING AND AGEING</b> .....	<b>17</b>
<b>1. Battery technologies and application</b> .....	<b>19</b>
<b>2. Li-ion Batteries</b> .....	<b>21</b>
2.1. Principle of operation .....	21
2.2. Negative Electrode.....	22
2.3. Positive Electrode .....	24
2.4. Electrolyte.....	26
2.5. Separator and collector .....	27
<b>3. State of the art of fast charge</b> .....	<b>27</b>
3.1. Standard charging method .....	28
3.2. Fast charging methods.....	28
3.3. Ohmic-drop compensation fast charging method.....	32
<b>4. Lithium-ion battery ageing</b> .....	<b>33</b>
<b>5. Conclusion</b> .....	<b>36</b>
<b>6. References</b> .....	<b>38</b>
<b>CHAPTER 2: EXPERIMENTAL SETUP, MATERIALS, EQUIPMENT AND BATTERY CHARACTERIZATIONS</b> .....	<b>43</b>
<b>1. Introduction</b> .....	<b>45</b>
<b>2. Lithium battery</b> .....	<b>45</b>
2.1. Lithium iron phosphate battery, C/LFP.....	45
2.2. Nickel manganese cobalt oxide battery, C/NMC.....	46
2.3. Lithium titanate oxide - lithium iron phosphate battery, LTO/LFP .....	47
<b>3. Battery test bench, characterization and charging methods</b> .....	<b>47</b>
3.1. Test bench .....	47
3.2. Charging and discharging protocols.....	48
3.3. Battery characterizations.....	50
3.3.1. Internal resistance .....	50
3.3.2. State Of Charge, SOC .....	52

3.3.3. State Of Health, SOH.....	52
3.3.4. Energy and coulombic efficiencies .....	52
<b>4. The ventilation test bench: Conception of the air canal .....</b>	<b>53</b>
4.1. Air canal characteristics .....	53
4.2. Air flow measurements .....	54
4.3. Determination of heat transfer coefficient by forced convection.....	56
<b>5. Determination of heat capacity of C/LFP and the heat transfer coefficient inside climatic chamber .....</b>	<b>57</b>
<b>6. Post-mortem analysis methodology.....</b>	<b>60</b>
6.1. X-ray tomography .....	60
6.2. SEM Analysis .....	60
6.3. Gaseous Chromatography analysis.....	60
6.4. Electrochemical characterization with coin cell .....	61
<b>7. References .....</b>	<b>61</b>
<b>CHAPTER 3: FAST-CHARGING OF LI-ION BATTERIES .....</b>	<b>63</b>
<b>1. Introduction.....</b>	<b>65</b>
<b>2. Fast charge process for C/LFP battery .....</b>	<b>65</b>
2.1. Fast charge of the battery with normal method .....	65
2.2. Fast charge process of the C/LFP battery with ODC .....	67
2.2.1. High level ODC .....	67
2.2.2 Influence of the compensation rate .....	71
2.3. Temperature and thermal effect during fast charge of C/LFP Battery .....	73
2.3.1. Fast charge of C/LFP battery with normal method.....	73
2.3.2. Fast charge of C/LFP battery with ODC method .....	74
2.3.3. Ventilation system effect.....	75
<b>3. Fast charge of C/NMC battery with ODC method .....</b>	<b>78</b>
<b>4. Fast charge of LTO/LFP battery with ODC method .....</b>	<b>81</b>
<b>5. Comparison of the three batteries .....</b>	<b>85</b>
<b>6. Conclusions .....</b>	<b>88</b>
<b>7. Reference.....</b>	<b>89_Toc496651014</b>
<b>CHAPTER 4: C/LFP LI-ION BATTERY THERMAL MODELLING.....</b>	<b>91</b>
<b>1. Introduction.....</b>	<b>93</b>
<b>2. C/LFP Li-ion battery thermal model description.....</b>	<b>95</b>
2.1 Battery Description .....	95
2.2 Development of the thermal model .....	96
2.2.1 Heat sources in Li-ion battery during charge.....	97

2.3 Determination of the model parameters .....	98
2.3.1. Reversible heat source .....	98
2.3.2. Irreversible heat source .....	101
<b>3. 0D thermal model of Li-ion battery .....</b>	<b>101</b>
3.1. Thermal model description .....	101
3.2. Simulation results and validation .....	102
<b>4. "3D" thermal model of Li-ion battery.....</b>	<b>104</b>
4.1. 2D axi-symmetric battery model .....	104
4.2. Sensibility analysis of the thermal conductivity .....	107
4.3. Simulation of internal gradient of temperature .....	111
4.4. Influence of the ambient temperature .....	113
4.5. Influence of the battery cooling .....	114
<b>5. Conclusion .....</b>	<b>117</b>
<b>6. References: .....</b>	<b>117</b>
<b>CHAPTER 5: AGEING STUDY OF C/LFP BATTERY.....</b>	<b>121</b>
<b>1. Introduction.....</b>	<b>123</b>
<b>2. Cycling ageing .....</b>	<b>124</b>
<b>3. Characterization of the aged LFP batteries.....</b>	<b>127</b>
3.1. X-Ray tomography photographs of batteries .....	127
3.2. Internal visual inspection of the batteries .....	129
<b>4. Post-mortem electrochemical characterisation.....</b>	<b>130</b>
<b>5. Post-mortem analysis of the electrolyte by GC-MS .....</b>	<b>134</b>
<b>6. Conclusion .....</b>	<b>135</b>
<b>7. References .....</b>	<b>135</b>
<b>GENERAL CONCLUSION.....</b>	<b>137</b>

# General Introduction

---



## General Introduction

Nowadays, the present energy economy is widely based on fossil fuels and our dependency on these sources of energy brings several serious problems to our planet. The first and most important impact is the exhaustion of the fossil resources caused by the continuous and increasing demands for oil, gas and coal for example. The other problem is the production of greenhouse gasses emissions, primarily CO<sub>2</sub> and they are dramatically increasing during these last decades. The direct effect of these greenhouse gases is the global warming and climate change phenomenon which has been the main issues historically rectified during the COP21 in Paris with the Paris Agreement [1].

So, it is important to have an easy access to clean energy sources in different forms and for various applications. The challenge of our modern society is to explore new clean and suitable sources of energy and to minimize our energy needs. The need for renewable and efficient clean energy production grows as a consequence.

Wind, solar and tidal powers are some examples of renewable energy source but their irregularity makes that they require storage media to supply energy at the peak of demand and to consume when necessary. Electrochemical systems such as batteries can efficiently store and deliver energy on demand. Currently, rechargeable batteries or secondary batteries are the electrochemical storage systems that are frequently being used in various application fields. Portable applications are the main sector that depends on this type of energy storage, for example smartphones, tablets or laptops. For stationary applications such as for stand-alone power plants, secondary batteries are identified as a potential solution to mitigate both the intermittency and limited predictability of alternative energies. The transportation sector has also become very dependent on these rechargeable batteries over the past few years, as new electric and hybrid vehicles or EV/HEVs have been commercialized throughout the world. Moreover, portable transportation vehicles such as fordable electric scooters have also gain a huge popularity among urban commuters. Needless to say, the transportation sector has marked a turning point in the increased demand for more robust, energy efficient and high capacity rechargeable batteries. As a result, the Li-ion rechargeable battery has become the major technology system to satisfy this increased demand and we see in our electronic era, almost all of our electronic appliances use rechargeable battery as their main source of power. Usually, the Li-ion technology is used for this purpose.

In our everyday life, all of the electronic appliances which use rechargeable battery, at the end of the day, regardless of their battery technology, need to be recharge at some point. That's how rechargeable batteries work; they need to be recharge after every usage. Unfortunately, the

recharging process could consume a lot of time, usually depending on the technology of the batteries. As the old quote says, time is gold so, it is really critical to reduce the overall charging time. That's where fast charging technology comes to the rescue. In the case of portable devices arena nowadays like smartphones, fast charging are becoming a must-have feature as manufacturer adopt this capability with the rise of their own norms such as Quick Charge by Qualcomm [2,3] or VOOC by OPPO [4,5]. In the transportation sector, the fast charging process for rechargeable batteries is still a mystery box that yet to be unveiled because of their higher capacity and sensibility. Fortunately, there are already some studies underway orienting towards that objective and our work is conducted in the same direction. It will be developed and explained slowly throughout this manuscript.

Chapter 1 proposes a short overview of the lithium-ion technologies and the materials composition inside battery cell such as the negative and positive electrode, separator, electrolyte and current collector. The principal of operation of lithium-ion battery is also presented. Different methods of fast-charging protocols are also described based on a bibliography study. Our own fast-charging method is also detailed here along with the assessment of the battery ageing possibility.

Chapter 2 describes the experimental setup for this study such the apparatus, materials and the test bench used. Battery cells characteristics that are used in this thesis are detailed in this chapter. Some methods to determine important parameters and ageing post-mortem procedures are also described.

Chapters 3 and 4 give the main results obtained during the period of the thesis. Chapter 3 report the results of fast charging using ohmic-drop compensation method in term of charging time while Chapter 4 presents some simulation results regarding thermal analysis of the battery cell.

Finally, Chapter 5 depicts the results of the post-mortem analysis of the battery ageing caused by that same ohmic-drop compensation method.

# **Chapter 1: Li-ion battery; Presentation, operation, fast- charging and ageing**

---



## 1. Battery technologies and application

Today, there are several types of battery technology. The major differences between those technologies are the materials that constitute both electrodes. Some offer more advantages than the others and same go for the disadvantages. **Table 1.1** depicts some of the characteristics for several types of battery technology. If examine closely, Li-ion battery is superior in many aspects compared to others.

**Table 1.1: Characteristics of several types of battery technology [6]**

System	Voltage (V)	Specific Energy (Wh.kg <sup>-1</sup> )	Energy density (Wh.L <sup>-1</sup> )	Energy cost (€.kWh <sup>-1</sup> )	Advantages	Disadvantage
Sealed lead-Acid	2	30-40	60-75	50-150	Cheaper, widely available	Heavy, limited cycle life
Ni-Cd	1.2	20-60	20-150	250-400	Reliable, good low temperature behavior, any charge retention after prolonged discharge	Heavily toxic material, memory effect, High cell self-discharge rate
Ni-MH	1.2	50-80	90-300	300-700	High energy density, environmental friendly	Higher internal resistance, self-discharge
Lithium-ion with Li(Ni,Co,Al)O <sub>2</sub> - based positive electrode	3.6	100-160	160-315	800-2000	High specific energy, low self-discharge, voltage profile = f(SOC)	Expensive, requires safety electronics,
Lithium-ion with LiFePO <sub>4</sub> - based positive electrode	3.2	80-120	170-220	700-1400	Safe, voltage profile with a plateau between 20%<SOC<90%	Expensive, requires safety electronics,

Li-ion battery possesses higher energy densities per mass and volume than other types of batteries as shown also in **Fig. 1.1**. In addition, Li-ion technology provides higher voltages than nickel based systems for example. However, the energy cost of this Li-ion technology is the highest compared to others. Nevertheless, Li-ion batteries have gained a significant amount of popularity among the transportation manufacturers, as transport applications requires high energy density, long cycle life, safety, reliability; the cost and weight are also very important.

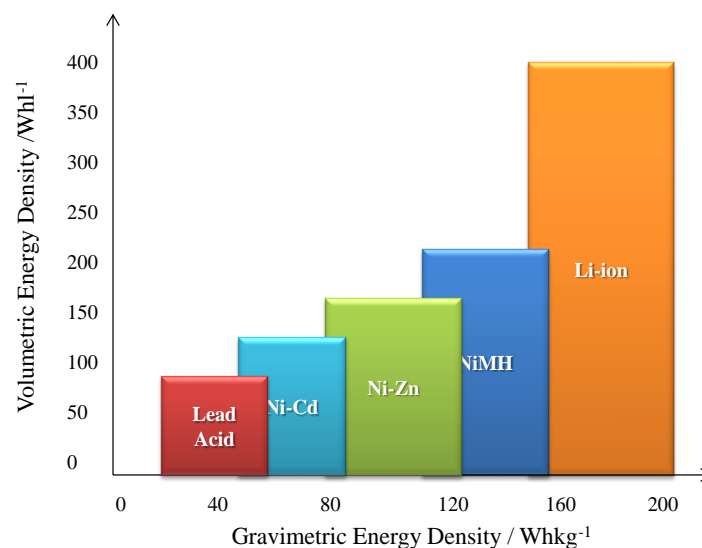


**Figure 1.1:** Comparison of varied electrical storage technologies [6].

It is obvious that the Li-ion batteries have suitable performances (high energy density, high power density, high discharge rate) for this application and as well as for portable transportation vehicle (i.e. electric scooters etc...). For individual electric transportation vehicle for example, the Li-ion battery seems to be unquestionable due to the required high specific energy. Li-ion batteries have energy density approximately three to seven times higher when compared to other technologies. They allow manufacturer to build electric vehicles with acceptable performance in term of range, speed and acceleration.

Now, the cost of Li-ion batteries is one of the most important issues for transportation application. The high cost is mainly attributed to the materials which constitute the batteries; positive electrode material represents 40-50% of the overall battery cost, and negative about 20-30%. Apart for safety issues of Li-ion batteries, one of the main setbacks of electric transportation vehicle is the recharging time of the battery packs. The charging procedures require suitable hardware and fast charging protocols for monitoring the battery cells and also shorten the overall charging time of the vehicles. Nowadays, the charging process still takes a lot of time and the problems need to be addressed quickly and thoroughly to cope with the consumers' demands as this type of vehicle starts flooding into the transportation market. Our study is pointing towards this objective as our base foundation.

However, even inside the Li-ion battery territories itself, there are also many types of technologies that have been implemented. The main difference between one another is the active materials which constitute their electrodes, but they all have a common essential point which is the exchange of Li<sup>+</sup> ions. The other differences between them could be their size, shape, electrolyte or separator

employed. Here, only Li-ion technologies that have been used in this study are presented but of course there are many others.

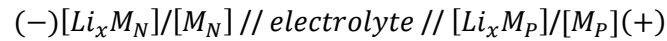
## 2. Li-ion Batteries

### 2.1. Principle of operation

A rechargeable battery cell is composed by two electrodes; each contains an active material and a current collector enabling the connection to the external electrical circuit. These active materials are those which are involved in the oxidation-reduction (redox) reactions which is the origin of the operation of any battery. These batteries therefore differ according to the technology used.

The electrodes are immersed in an electrolyte which allows the transport of charges in ionic form, necessary for the redox reactions to take place. The separator acts as an electrical insulation for both electrodes. It must prevent electron transfer internally but at the same time allows ionic transfer.

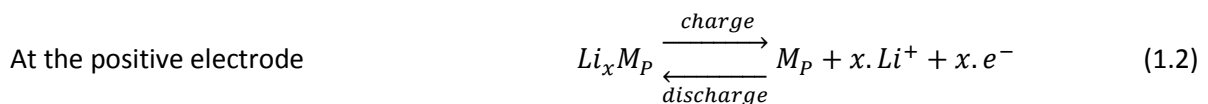
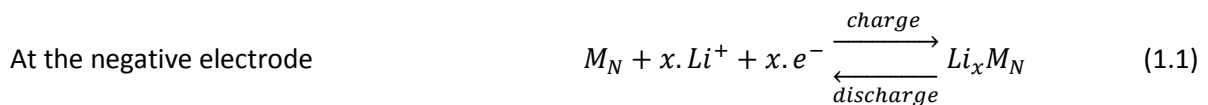
This basic assembly can be package in different ways depending on the shape of the battery. In a very general way, the electrochemical chain can be written as:



with:  $M_P$ : active positive material, operating at high potential from +3 to +5V vs.  $Li^+/Li$

$M_N$ : active negative material, operating at low potential below + 2 vs.  $Li^+/Li$

The operation of a battery cell consists of two redox half-reactions. The main mobile species in a Li-ion battery is the  $Li^+$  cation and when the half-reaction at either electrode takes place, this cation is inserted directly into or extracted therefrom the crystal structure of the active material of the electrodes. The chemical half-reactions which take place at the active material of the negative electrode,  $M_N$  and at the active material of the positive electrode,  $M_P$  can be written as follows [7]:



With  $x$ , the number of  $Li^+$  cations transported during charging or discharging.

The overall reaction of the electrochemical system is given by the equation:

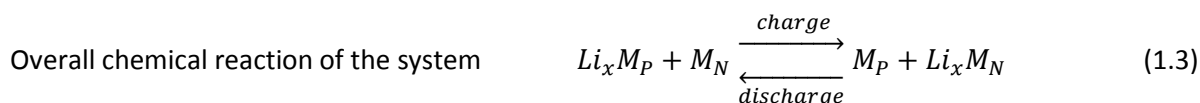


**Fig. 1.2** depicts the operation of the Li-ion battery cell during charging and also during discharging process.

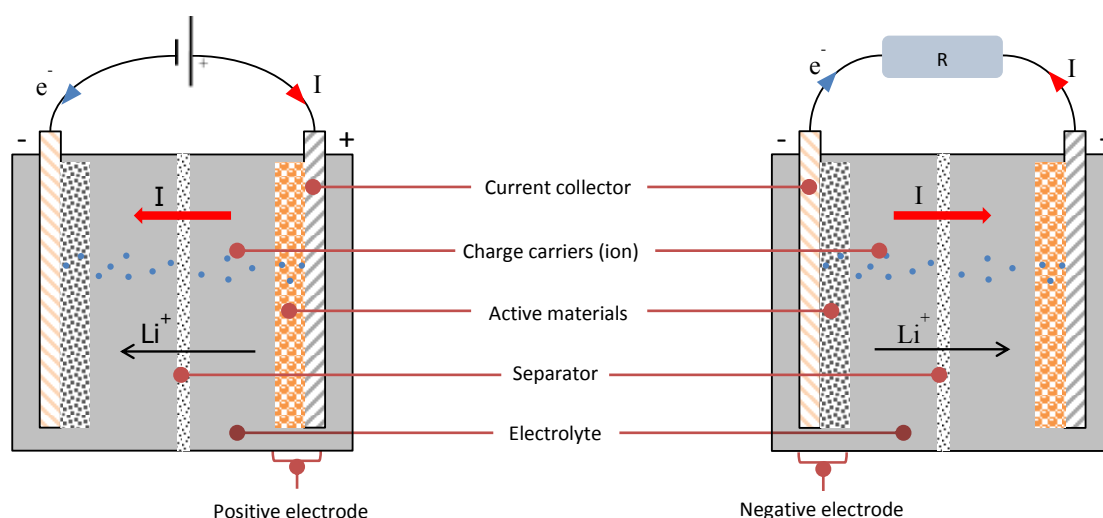


**Figure 1.2:** Operating principle of a Li-ion cell during charging (left) and discharging (right)[8].

In a Li-ion battery, there are two charge carriers: the  $Li^+$  cations in the electrolyte which was presented earlier and also the electrons in the active materials of both electrodes. These two types of charge carriers are called mobile species [9]. As shown in **Fig. 1.2**, these two mobile species move at an opposite direction from each other in both cases; charging and discharging.

## 2.2. Negative Electrode

There are a few types of negative electrode: those with lithium metal oxide and those based on carbon or other compound as shown in **Table 1.2**. They have their own advantages and inconvenient.

Materials	Graphite $\text{LiC}_6$	LTO $\text{Li}_4\text{Ti}_5\text{O}_{12}$	Si $\text{LiSi}_{22}$
Crystal structure	Graphene planes	Spinel	Alloying material
Mass capacity (theoretical /practical) (mAh/g)	372 / 350	175 / 160	4200
Volumic capacity (theoretical) (mAh/cm <sup>3</sup> )	837	613	9786
Average potential in delithiation (V)	0.1	1.55	0.4
Lithiation potential vs. $\text{Li}^+/\text{Li}$ (V)	0.07, 0.10, 0.19	1.55	0.05, 0.21
Delithiation potential vs. $\text{Li}^+/\text{Li}$ (V)	0.1, 0.14, 0.23	1.58	0.31, 0.47
Voltage range (V)	[1.5 – 0.01]	[2.0 – 1.0]	[1.2 – 0.01]
Volume change (%)	10%	0.20%	270%
Cost	Medium	High	Low
Advantages	Long cycle life, abundant	"zero strain" material , good cycling and efficiency	High capacity, abundant
Inconvenient	Relatively low energy density, inefficiencies due to SEI formation	High voltage, low capacity (low energy density), gassing phenomena	Volume expansion (nanometric particles), Li consumption for new SEI (electrolyte consumption)

However, the most common negative electrode is graphite because of its cost and abundancy. The lithium titanium dioxide (LTO) electrode for example is less common but nevertheless gains more interest these past years. The most important problem that the negative electrode faces is the problem of dendrite. This problem occurs during charging process when the deposition of lithium ions form a non-uniform layers. The dendrites could grow by time and puncture through the separator which then would create a short circuit.

However, carbon-based electrode is much less sensitive to the problem of dendrites to be used as lithium intercalation materials. It has a low and flat working voltage profile at about  $-2.7\text{V}/E_{\text{SH}}$  which makes it an excellent negative electrode for lithium battery [11]. Moreover, since carbon is used under its crystalline form (graphite), it has a high capacity and stability to receive the  $\text{Li}^+$  ions reversibly without altering its properties [12]. Graphite is an insertion material in which Li-ions come to lodge into. The structure of graphite allows a high reversibility because it is constituted of multi-layered plane of graphene where the lithium ions penetrate right through and form a lithium/carbon intercalation compound  $\text{Li}_x\text{C}_6$  (**Fig. 1.3**).

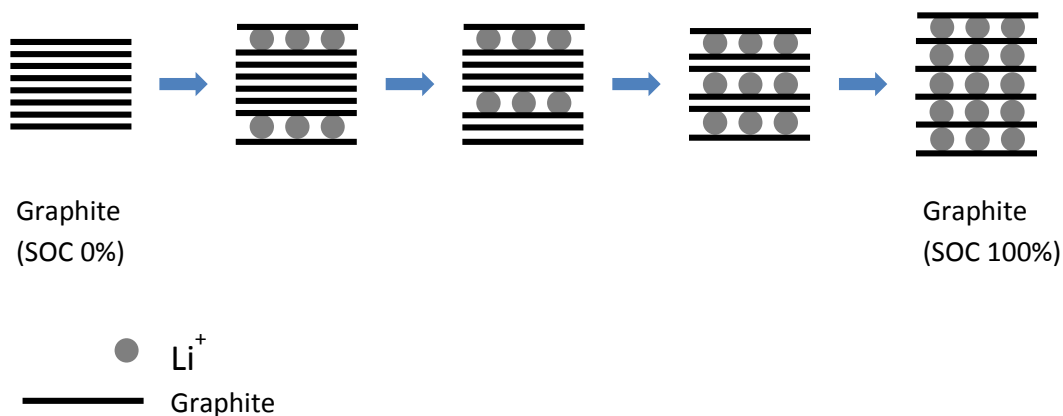


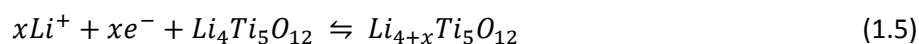
**Figure 1.3:** Intercalation of lithium ions in graphite [13]

The general electrochemical reaction for the graphite material negative electrode is:



For lithium titanium dioxide (LTO) electrode, even though it is more prone to have the problem of dendrite, its high chemical and thermal stability makes it a really good alternative towards graphite materials. Moreover, this compound is also really promising for the EV and HEV due to its capability for fast charging. Indeed, for this material, the insertion of lithium is made at an electrochemical potential superior to the one of metallic lithium. ( $\sim 1.55\text{V}$  vs.  $\text{Li}^+/\text{Li}$ ). Thus, it can accept high currents of charge without risk of lithium metal forming at the interface, contrary in the case of graphite.

The general electrochemical reaction for the LTO negative electrode is:



### 2.3. Positive Electrode

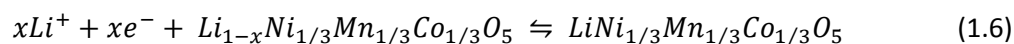
There are many types of technologies for the active materials of the positive electrode. **Table 1.3** shows some major characteristics of the materials used. As usual, they have their advantages and also their inconvenients.

However, only two materials for the positive electrode are considered for this study. First, it is the lithium iron phosphate (LFP) and secondly the nickel-manganese-cobalt (NMC).

Materials	NCA $\text{LiNi}_{0.8}\text{Co}_{0.15}\text{Al}_{0.05}\text{O}_2$	NMC 111 $\text{LiNi}_{1/3}\text{Mn}_{1/3}\text{Co}_{1/3}\text{O}_2$	LFP $\text{LiFePO}_4$	LMO $\text{LiMn}_2\text{O}_4$	LCO $\text{LiCoO}_2$
Crystal structure	Layered	Layered	Olivine	Spinel	Layered
Mass capacity (theoretical /practical) (mAh/g)	279 / 200	280 / 170	170 / 165	148 / 120	274 / 148
Volumic capacity (theoretical /practical) (mAh/cm <sup>3</sup> )	1284 / 700	1333 / 600	589	596	1362 / 550
Average potential vs. Li <sup>+</sup> /Li (V) [voltage range]	3.7 [3.0 – 4.25]	3.7 [2.6 – 4.3]	3.4 [2.0 - 4.0]	4.1 [3.5 – 4.3]	3.8 [3.6 – 4.85]
Cost	Medium	Medium	Low	Low	High
Advantages	High capacity and voltage Excellent rate performance	High voltage, moderate safety	Excellent safety, cycling, rate capability, abundance of Fe, low toxicity	Abundance of Mn, high voltage, moderate safety, excellent rate performance	Performance
Inconvenients	Safety, resource: limitation of Ni and Co	Resource: limitation of Ni and Co	Low voltage and capacity (substituted variants), low energy density	Limited cycled life, low capacity	Safety, resource: limitation of Co, low capacity

For so long, lithium cobalt oxide,  $\text{LiCoO}_2$  (LCO) which is the first used and still widely used materials as the positive electrode. Unfortunately, the high costs of the cobalt material due to its limited worldwide reserves, some other alternatives materials for positive electrode are developed. Moreover, LCO becomes unstable at high temperature and releasing oxygen which could reacts with the organic electrolyte solvent with high risk of inflammation or explosion. This material is also toxic. Thus, for that reasons, the NMC material is one of the materials that have been developed as a substitution to the lithium cobalt oxide. This material harbors with a more moderate cost, higher specific capacity and better thermal tolerance.

The general electrochemical reaction for NMC positive electrode is:



For the past few years now, a new alternative of the lithiated metal oxide is introduced. The new positive electrode is constituted by phosphates of transition metals. In this study, the lithium iron phosphate  $\text{LiFePO}_4$  is the main battery technology that is used as the reference. This materials crystalline structure is isomorphic and allows the reversible insertion of lithium. They are very attractive materials because in spite of a nominal voltage lower than that of other materials, they are less dangerous in case of abuse conditions [14,15].

The general electrochemical reaction for LFP positive electrode is:



## 2.4. Electrolyte

There are many types of electrolyte such as liquid electrolyte, solid electrolyte and gel electrolyte. Liquid electrolytes are the most common electrolytes used in the rechargeable battery domain. Practically, a Li-ion does not pass directly from one electrode to the other but is transferred from one solvent molecule to the next and reaches the other electrode [16]. So, these electrolytes can only be used in a Li-ion battery if they contain lithium salt which is dissolved in an organic solvent. An example of the latter is the lithium salt  $LiPF_6$  which is dissolved in an organic electrolyte called ethylene-dimethyl-carbonate. However, this type of electrolyte presents two big inconvenient which are low conductivity and also strong inflammability. All of the battery that has been used in this study possesses this type of electrolyte.

For solid electrolyte, the lithium salts are incorporated into a polymer material and, after various manufacturing steps, a film is obtained. This film can also be used directly as a separator. Solid electrolytes have low conductivity at room temperature and often required heating ( $60^\circ\text{C}$  to  $80^\circ\text{C}$ ) for the battery to be operational. The first solid electrolytes have been developed for negative electrode cells in lithium metal, in order to mechanically restrain the growth of dendrites. They now have also been used for lithium-ion cells. However, a difficulty exists at the solid graphite/electrolyte interface. In fact, the contact is bad compared to the liquid electrolyte which can infiltrate inside the pores of the graphite.

The gel electrolytes are obtained by dissolving a solid membrane in a solvent. Compared to solid electrolytes, they provide better contact with the electrodes and a sufficient conductivity at room temperature. They have the advantage over liquid electrolytes of allowing cells to be made in a flexible package (pouch cells), but the contact resistance of the batteries remains higher than that of batteries with liquid electrolyte [17].

## 2.5. Separator and collector

The separator is an important part of the battery. It is a mono or multilayer microporous polyethylene and polypropylene sheet isolating both electrodes. It must therefore have these following properties [18]:

- Good mechanical strength in order to avoid electrical contact between the electrodes
- low electronic conductivity
- A good wettability which allows the separator to soak with electrolyte and thus obtain a good ionic conductivity
- Chemical neutrality with respect to other elements of the battery, i.e. it must not react with the different chemical components of the battery.

Some separators play an active role in the safety of the cell by becoming impermeable to ions from a certain temperature, which blocks the chemical reaction in case of thermal runaway. These separators are called "shutdown separator" [19] and it should be noted that this phenomenon is irreversible.

The current collector is responsible for transferring the electrons from the active material of the electrode to the external circuit. Aluminum is a good candidate for this, very light and good electrical conductor. However, it reacts with Li-ions below 0.7V vs  $\text{Li}^+/\text{Li}$ . Copper, also a very good electrical conductor, is interesting but oxidizes above 3.2V vs  $\text{Li}^+/\text{Li}$ .

The graphite has a potential of 0.3 V vs  $\text{Li}^+/\text{Li}$  and most of the positive electrode materials presented above have, at the end of the charge, a voltage greater than 3.2 V vs  $\text{Li}^+/\text{Li}$ . Hence the choice frequently encountered: aluminum collector for the positive electrode and copper for the negative electrode.

## 3. State of the art of fast charge

Fast charging for Li-ion battery is crucial for our everyday use of electronic devices and transportation. However, Li-ion batteries still have some serious drawbacks especially for fast charging protocols. Many of the problems can be related for one part to surface phenomena

occurring on the negative and positive electrodes and for another part to structural modifications (expansion-contraction, crystal disorder), in simpler words, internal degradations of active materials. Moreover, safety protocol is also the main concern during the manipulation of this type of battery especially during high temperature elevation because of its high specific energies. In regards of fast charging process, the high temperature elevation is something that is unavoidable.

Thus, reliable indicators and reliable fast-charging protocols have to be developed and improved to properly charge the battery until a certain state of charge and monitor the state of health of the battery.

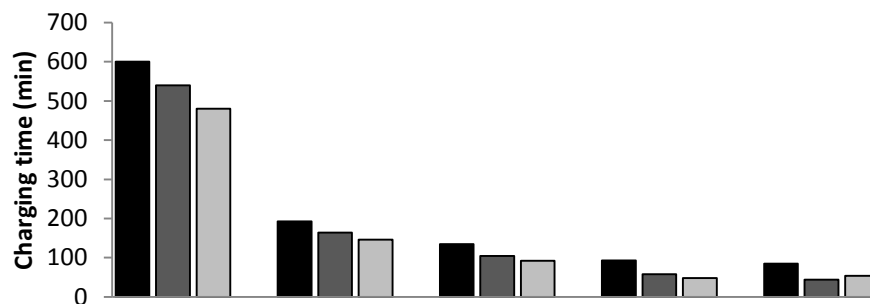
### **3.1. Standard charging method**

Generally, the charging process of a Li-ion battery is divided into 2 charging stages; these are the constant current stage (CC) and constant voltage stage (CV). During the CC stage, the battery is charged at a chosen constant current (i.e. charging rate) until a certain upper voltage limit  $U_f$  is reached before switching to CV stage. The upper voltage limit  $U_f$  is predetermined by the manufacturer; it is designed to ensure longer battery life-span by avoiding side reactions. During the CV stage, the battery is normally charged more slowly with a degrading current to maintain the battery at a constant voltage until the current limit called  $I$  cut-off, is attained. Even though the CV stage is slow, it allows the relaxation of the species concentrations inside the electrolyte and electrode materials. The duration of the total charging period depends on the charging rate applied during the CC stage.

### **3.2. Fast charging methods**

In the context of EV applications, Li-ion batteries are faced with reliability and durability issues. Nevertheless, it is a mandatory requirement in EV applications to minimize the battery charging time; so, a fast-charging method must be developed properly. If fast-charging is applied, theoretically the battery can be recharged in a shorter period, which is not the case for current EVs.

Different methods are proposed in the literature for fast-charging. The fast-charging process for the Li-ion battery can be performed by increasing the C-rate of the CC stage [20, 21, 22].



Charging C-rate	0.1C	C/3	C/2	C	1.5C
100% of C (min)	600	193	135	93	85
90% of C (min)	540	164	104	58	44
80% of C (min)	480	146	92	48	34

**Figure 1.4:** Charging time (minutes) and battery discharged capacity (% C) when different charging rates (from 0.1C to 1.5C) are used in the constant current step: the constant voltage step finishes in each case when battery capacity reaches the desirable value [20].

*Lopez and al.* [20] observed that the total charging time is reduced quite significantly when the charging C-rate increases as shown in **Fig. 1.4**. For example, they save about 42% of charging time for a fast charge at 1.5C-rate compared to the nominal C-rate of C/2 to reach 90% of C-rate. Nevertheless, their results show that the energy efficiency of the charging process decreases greatly when the charging C-rate rises and their result mainly focus on the first stage of charging process which is the constant current stage.

On the other hand, *Huang and al.* improve their fast charging strategies by evaluating and characterizing Li-ion battery [21]. Brief current of charging and discharging interrupts the charging process during constant current period to restrict the hysteresis effect. There's also a fast charging strategy of implying a multistage charging process during the constant current (CC) period [22] and constant voltage (CV) period [23] to reduce the charging time as shown in **Fig 1.5**.

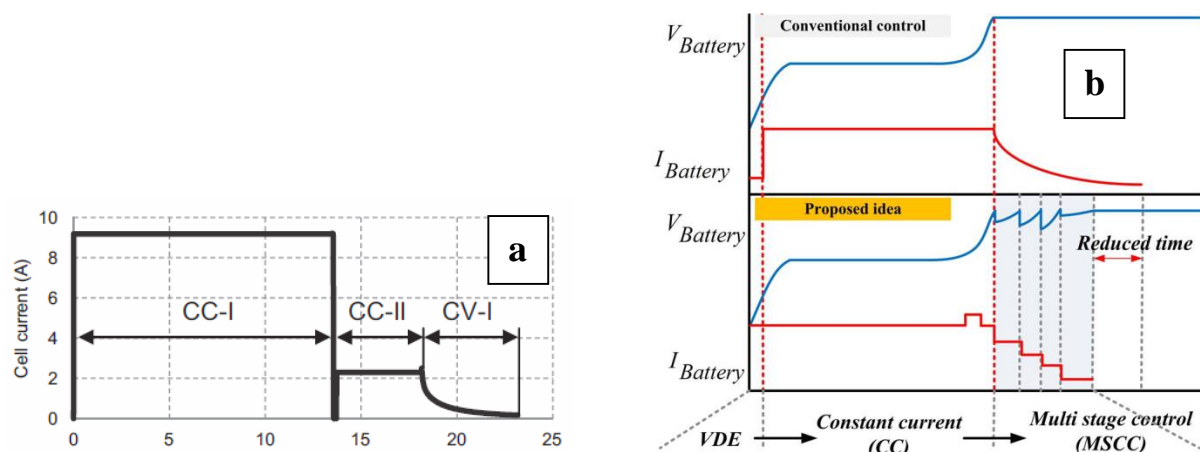


**Figure 1.5:** Multistage fast charging strategy during (a) constant current stage [22] and (b) constant voltage stage [23]

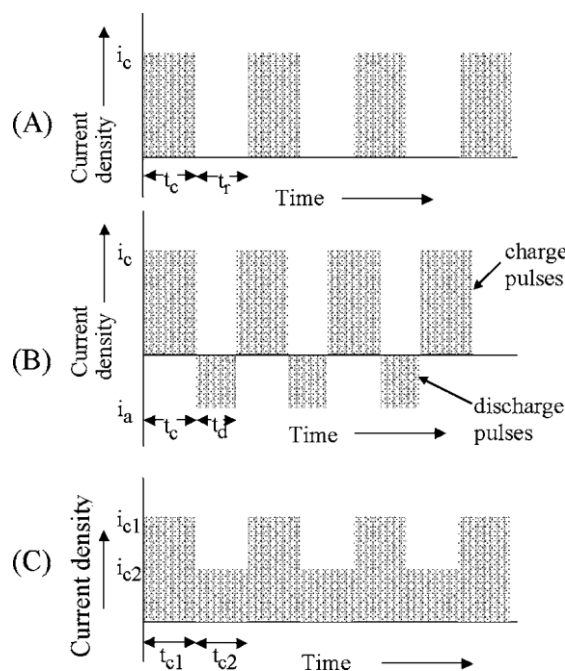


**Figure 1.6:** Schematic of fast charging process of different pulse sequences. (A) Constant amplitude pulsed current interspersed with identical rest periods; (B) constant amplitude pulsed current interspersed with alternating constant amplitude discharge pulses; and (C) pulsed current consisting of a sequence of different amplitudes charge current density pulses [24].

Other methods for fast-charging are also proposed in the literature based on pulsing current [24, 25, 26]. This latter method has shown good global performance, but an optimal configuration remains a challenge. For its part, the pulse charging is based on constant current steps of short duration followed by relaxation periods. The sequences can vary depending on the pulse amplitude and

duration, as well as on the relaxation time as shown in **Fig. 1.6**. This method is highly recommended for fast-charging purpose as the current imposed is really high. Pauses are required to reduce or prevent the metallic lithium formation. The metallic lithium formation can greatly interfere with the charging process according to *Purushothaman and al.* [24]. However, their studies only focus on the empirical calculation and simulation without any real experiment implementation.

Finally, Ohmic Drop Compensation (ODC) method might also be used for fast-charging. As far as we know, this latter electrochemical method [27, 28], has never been used for Li-ion battery fast-charging. Nonetheless, there are some studies that are based on this method for developing fast-charging chargers [29, 30, 31, 32, 33]. For instance, *Saint-Pierre* [29] conducted his studies, which focused on the charger's electronic circuitry rather than the impact of this method on the battery itself, which is in contrary, the main purpose of this paper. His study shows that with this method, the charging time is reduced by more than 30 minutes. *Lin and al.* [30, 31] also proposed a fast-charging charger with built-in resistance compensator (BRC) to achieve a fast and stable charging process on Li-ion battery packs.

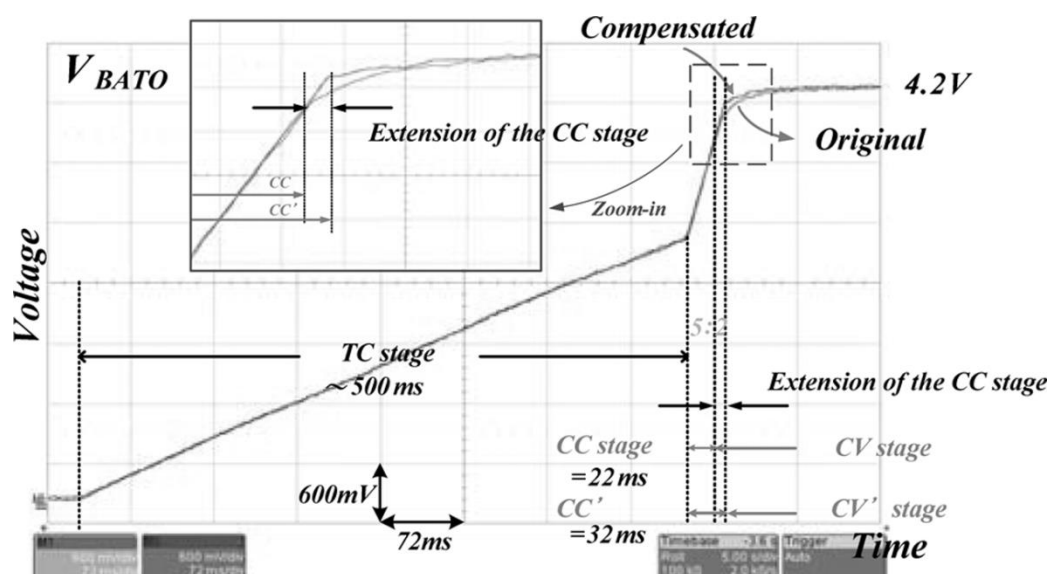


**Figure 1.7:** Waveforms of the voltage with and without the BRC technique. The CC stage of the original design is extended to the CC' stage with the BRC design [31].

*Huang and al.* and *Peng and al.* also conducted their study on a similar area to improve their fast-charging charger [32, 33]. *Lin and al.*'s system is able to charge the battery pack with adequate current and speed up the charging process time. They managed to shorten the charging time by using an ohmic-drop compensation method. This technique is applied to a battery pack and the compensated resistance consists of the external resistance of the battery pack as well as the

connections. The compensation technique is performed for a very short delay as shown in **Fig. 1.7**. The results establish the improvement of the charging time by means of external resistance compensation technique of the battery pack.

### 3.3. Ohmic-drop compensation fast charging method

Our fast charging method, called ohmic-drop compensation (ODC) method, which consists in compensating the ohmic-drop of the battery voltage caused by the internal resistance of the battery cell by changing the upper-bound voltage limit at the end of CC stage. This section will explain on how this method functions.

As in any electrochemical system, the cell voltage consists of the interfacial terms ( $U_{interface}$ ) and volumic ones ( $U_{volumic}$ ):

$$U = \sum U_{interface} + \sum U_{volumic} \quad (1.8)$$

$U_{interface}$  is the voltage between the both electrode/electrolyte interfaces at open circuit voltage ( $U_{OCV}$ ) and both overpotentials and given by:

$$\sum U_{interface} = U_{OCV} + \eta_+ - \eta_- \quad (1.9)$$

$U_{volumic}$  is the ohmic drop induced by the charge transport in each volume of cell elements (current collectors, electrolyte, connections).

This ohmic drop is proportional to the current when considering the ohm's law:

$$\sum U_{volumic} \approx R_i I \quad (1.10)$$

where  $R_i$  is the internal resistance of the cell.

The main and side reactions are dominated only by interfacial terms. The upper-bound voltage limit  $U_f$  predetermined by the manufacturer to maintain cycling performances is an indication of maximum interfacial voltage ( $U_{interface,max}$ ) to minimize side reactions.

Considering the current profile during the charging process, this maximum value of interfacial voltage is reached at the end of the CV stage:

$$\Sigma U_{interface,max} = U_f - R_i I_{cut-off} \quad (1.11)$$

When the cut-off current ( $I_{cut-off}$ ) is achieved.

The ohmic-drop compensation (ODC) method consists in changing the upper-bound voltage limit at the end of CC stage taking into account the internal resistance of the battery. Nonetheless, this new upper-bound voltage limit  $U'_f$  has to respect the maximum interfacial voltage value whatever the current rate ( $I$ ), especially, at the end of the CC stage:

$$U'_f = \Sigma U_{interface,max} + R_i I \quad (1.12)$$

Combining **Eq. 1.11** and **Eq. 1.12**, the new upper-bound voltage limit  $U'_f$  is then given by:

$$U'_f = U_f + R_i (I - I_{cut-off}) \quad (1.13)$$

Generally,  $I_{cut-off}$  is negligible as regards to the charge current  $I$ .

This latter ODC method is performed on a Li-ion battery considering a higher upper-bound voltage limit of the CC stage  $U'_f$  taking into account the ohmic-drop resistance of the battery. In order to avoid the risk of side reactions in the case of over-compensation, a rate of compensation,  $\alpha$ , is defined as a percentage of the internal resistance measured of the battery (see next section). In this condition, the new upper-bound limit voltage is given by:

$$U'_f = U_f + \alpha R_i I \quad (1.14)$$

$\alpha$  being the compensation rate and  $U_f$  is the upper-bound limit voltage from manufacturer.

The following charging stage which follows is the conventional constant voltage, CV stage where the voltage is maintained at the upper-bound limit voltage from manufacturer,  $U_f$ .

#### 4. Lithium-ion battery ageing

Even though the fast-charge method is able saving a lot of total charging time, it also impacts the battery cell life cycle and may induce fast ageing. Indeed, the fast-charge may involve side reaction occurrence owing to both the high temperature increases and the high cell voltage. Regarding the battery temperature change, the heat generation originates in the electrochemical processes inside the cell [34,35,36,37], and its propagation depends on the thermal [38] and geometric properties of

the cell [35, 39]. For a normally operated cell, even a combination of low thermal conductivity and inadequate cooling [40,41,42] is unlikely to generate sufficient heat to cause an increase in temperature that initiates exothermic side reactions [43]. Nevertheless, during fast-charging protocol, heat production rises leading to likely significant temperature increase of the cell. A thermal investigation of a cylindrical Li-ion battery (C/LFP) was performed by *Forgez and al.* [44]. The outer surface and internal temperature of the battery were measured using a thermocouple, and subsequently the heat transfer coefficient and heat capacities were determined. They used the current-pulse method (2 Hz) of different current magnitudes for the charging and discharging processes of the battery. Their results show that the internal battery temperature rises to 55°C for their charging/discharging conditions and there is about 10°C maximum gap between the inner and outer surface temperatures. Similarly, *Onda and al.* [45] have also led their studies on thermal behaviour of the Li-ion battery during rapid charge and discharge. In their studies, they undertook charging and discharging processes ranging from 1 C-rate to 3 C-rate. Their results show that the battery temperature rises to 100°C and 80°C during discharge and charge respectively at a regime of 3 C-rate.

Lithium-ion batteries experience different degrees of degradation depending on operation (calendar and cycling), due to various ageing mechanisms. Moreover, the ageing phenomena are highly complicated to characterize due to the factors cross-dependence. *A. Barré et al.* [46] presented a review of the main ageing mechanism of lithium-ion batteries for automotive application. *Paul et al.* [47] investigated the capacity fade of a lithium battery under cycling and calendar ageing, as well as heterogeneity of ageing in a battery pack. This work shows the importance of the consideration of cell-to-cell variation and different thermal conditions in order to investigate battery system ageing. *Shim et al.* [48] for their part have studied cycling ageing of a lithium-ion battery. They were able to observe a decrease in the battery capacity which depends on the operating temperature. This loss of capacity is accompanied by an increase in impedance. According to *Safari and Delacourt* [49] the complex ageing mechanism manifests itself in both cell impedance increases together with capacity fade. All studies demonstrate that, high temperatures are more detrimental for cell life upon storage by activating parasitic reactions. Capacity fade may result from two commonly reported degradation modes [50]. On one hand, cyclable lithium-ions may be shunt by parasitic reactions, such as surface film formation (i.e SEI growth), decomposition reactions, lithium plating, etc. In that case, a certain amount of lithium ions becomes no longer available for cycling between the positive and negative electrode, leading to capacity fade. This first phenomenon is called loss of lithium inventory (LLI). On the other hand, active mass of either the negative electrode (NE) or the positive electrode (PE) is no longer available for the insertion of lithium due to particle cracking and loss of electrical contact or

blocking of active sites by resistive surface layers. This second phenomena is called the loss of active material (LAM). *Birkl et al.* [50] propose a comprehensive list of degradation mechanisms, their causes, effects and links to degradation modes. A fault tree of the capacity fade base on [50] in case of Li-ion batteries can be presented on **Fig. 1.8**.

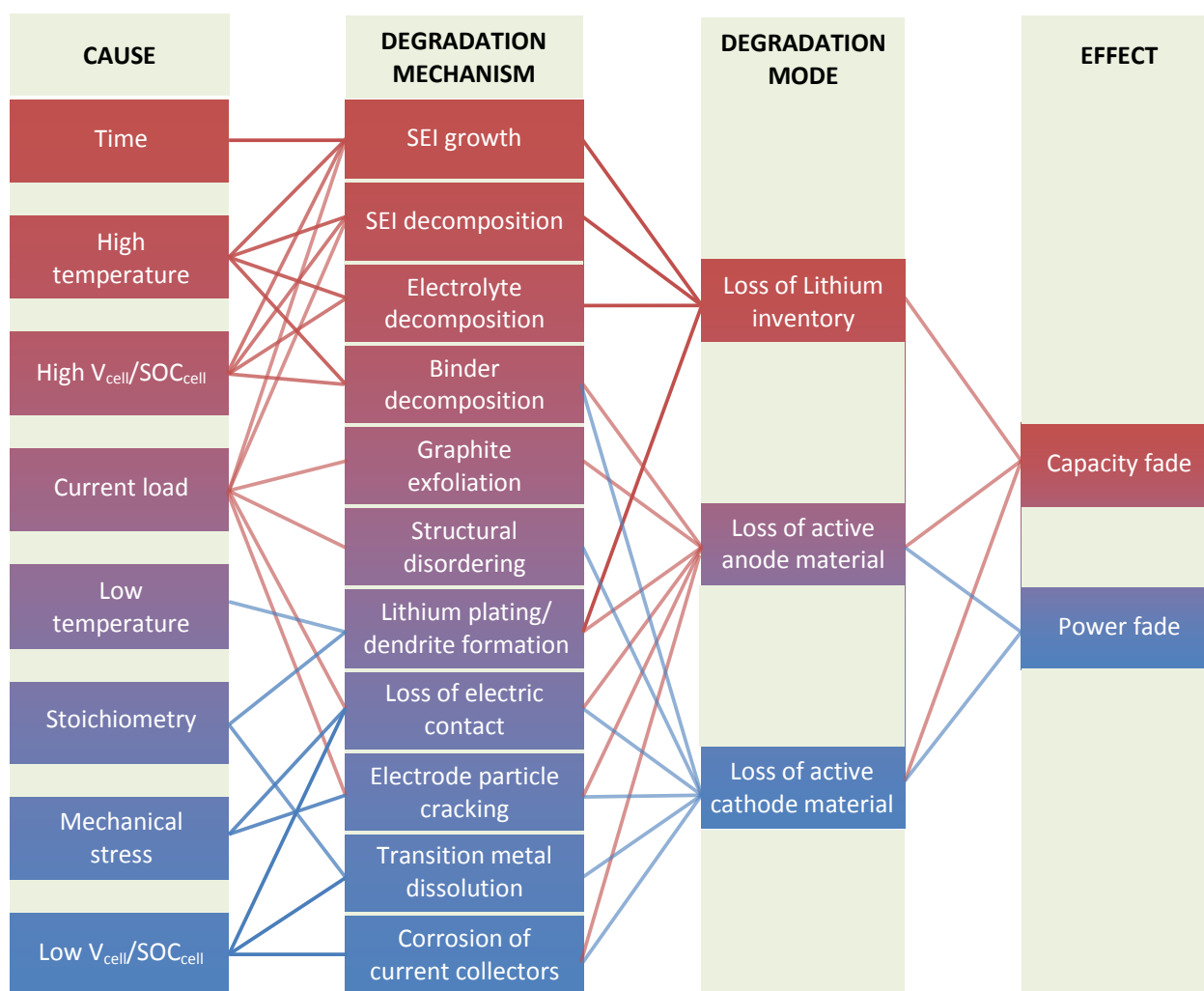


**Figure 1.8:** Fault tree for capacity fade and power fade of lithium-ion battery [33]

Regarding our fast charging protocol with ODC, loss of lithium inventory may be induced by SEI growth or electrolyte/binder decomposition. These both degradation mechanisms are accelerated at high cell voltage and temperature. Moreover at high voltage or high temperature electrolyte or electrolyte additive components could form gas bubbles inside the cell [51, 52, 53]. The second possible cause of capacity fade under fast charging with ODC is the loss of active material (LAM), i.e.

the modification of the electrode's materials which results from the electrode particle cracking, graphite exfoliation, structural disordering as well as loss of electric contact of the electrode when increasing the current load.

Whatever the routes are, the capacity or power fade of the battery primarily originated from high temperature elevation or/and high load of current and voltage. These degradations could also lead to the increase of the internal resistance of the battery. **Fig. 1.9** graphically illustrates some of the reported degradation mechanisms in Li-ion cells just now.

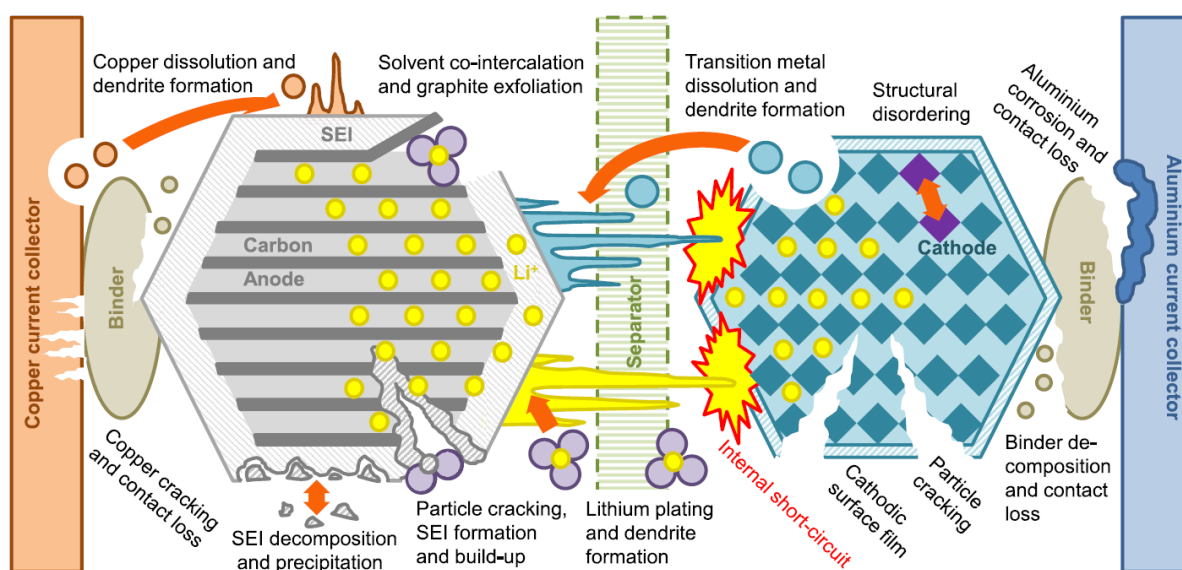


**Figure 1.9:** Degradation mechanism inside Li-ion battery [50]

## 5. Conclusion

Li-ion battery has become the major player in the electronic worlds as energy storage solutions. Meanwhile, transportation manufacturers are also catching up with new innovations with their electric and hybrid vehicles. Li-ion battery proves to be the major turning point for EVs and HEVs as this type of energy storage technology could satisfy the needs of a more efficient and performance power supply. However, the electric vehicle sector progression still hinders by a major problem of refuelling those energy supplies and in this particular case; recharging the batteries pack. Many studies have been pointed out towards that direction with the main objective is to shorten the charging period. So, fast-charging procedures are crucial for the future of EVs and HEVs.

There are many possibilities to perform fast-charging protocols. High current C-rates, multistage charging process and pulsation charging process are some methods that have been highlighted in this chapter. However, fast-charging procedure based on ohmic-drop compensation (ODC) method caught our eyes. Indeed, this thesis will try to elaborate and understand the ODC fast charging method in term of its overall performance on different Li-ion battery technology especially on total charging time, thermal aspect and ageing mechanism. The base of this ODC fast charging method is to try to compensate the ohmic-drop contribution during charging process caused by the internal resistance of the cell. Further in this manuscript, the results of ODC fast-charging will be detailed for different Li-ion batteries.

## 6. References

- [1] United Nations Treaty Collection, Status of Treaties, CHAPTER XXVII: ENVIRONMENT, (7d) Paris Agreement (Paris,12 Decmber 2015).  
[https://treaties.un.org/pages/ViewDetails.aspx?src=TREATY&mtdsg\\_no=XXVII-7-d&chapter=27&clang=\\_en](https://treaties.un.org/pages/ViewDetails.aspx?src=TREATY&mtdsg_no=XXVII-7-d&chapter=27&clang=_en)
- [2] <http://www.androidauthority.com/quick-charge-explained-563838/>
- [3] <https://www.qualcomm.com/products/features/quick-charge>
- [4] <http://www.androidauthority.com/vooc-fast-charging-686000/>
- [5] <http://www.oppo.com/en/technology/vooc/>
- [6] N. Kircheva, Contribution de l'émission acoustique pour la gestion et la sécurité des batteries Li-ion (2013), Doctoral dissertation, Université Grenoble Alpes.
- [7] L. Ménard, G. Fontès and S. Astier, Dynamic energy model of a lithium-ion battery, *Mathematics and Computer in Simulation*, 81(2) (2010), pp. 327 - 339.
- [8] E. Riviere, Détermination in-situ de l'état de santé de batteries lithium-ion pour un véhicule électrique (2016), Doctoral dissertation, Grenoble Alpes.
- [9] J. Newman and K. E. Thomas-Alyea, *Electrochemical Systems*, Chapter 8: Models for Electrode Kinetics, John Wiley & Sons, (2004), pp. 212 - 213.
- [10] N. Nitta, F. Wu, J. T. Lee and G. Yushin, Li-Ion battery materials: present and future, *Materials Today*, Vol. 18, Number 5, June 2015, pp. 252 – 264.
- [11] F. Miomandre, S. Sadki, P. Audebert and R. Méallet-Renault, *Electrochimie: Des concepts aux applications*, DUNOD, Chapter 11 (2011), pp. 205 - 224.
- [12] A. Manthiram, Materials challenges and opportunities of lithium ion batteries, *The Journal of Physical Chemistry Letters*, 2(3) (2011), pp. 176 - 184.
- [13] C. Sole, N. E. Drewett, and L. J. Hardwick, In-situ Raman study of lithium-ion intercalation into microcrystalline graphite, *Faraday discussions*, 172(2014), pp. 223-237.

[14] A. K. Padhi, K. S. Nanjundaswamy, C. Masquelier, S. Okada and J. B. Goodenough, Effect of structure on the  $\text{Fe}^{3+}/\text{Fe}^{2+}$  redox couple in iron phosphates, *Journal of the Electrochemical Society*, 144(5) (1997), pp. 1609 - 1613.

[15] A. K. Padhi, K. S. Nanjundaswamy and J. B. Goodenough, Phospho-olivines as positive-electrode materials for rechargeable lithium batteries, *Journal of the Electrochemical Society*, 144(4) (1997), pp. 1188 - 1194.

[16] C. Glaize and S. Geniès, *Les accumulateurs électrochimiques au lithium, haute température et à circulation d'électrolyte*, Lavoisier (2013).

[17] S. Martinet, *Nouvelles voies dans les accumulateurs lithium et les électrolytes de batteries*, Clefs CEA, n° 50-51 (2004-2005), pp. 130 - 133.

[18] F. P. Savoye, *Impact des impulsions périodiques de courant sur la performance et la durée de vie des accumulateurs lithium-ion et conséquences de leur mise en oeuvre dans une application transport*, (2012), Doctoral dissertation, Université Claude Bernard-Lyon I.

[19] S. S. Zhang, A review on the separators of liquid electrolyte Li-ion batteries, *Journal of Power Sources*, 164(1) (2007), pp. 351 - 364.

[20] J. Lopez, M. Gonzalez, J. C. Viera and C. Blanco, Fast-charge in lithium-ion batteries for portable applications, INTELEC 2004 26th Annual International Telecommunications Energy Conference, IEEE, (2004), pp. 19 - 24.

[21] S. J. Huang, B. G. Huang and F. S. Pai, Fast Charge Strategy Based on the Characterization and Evaluation of  $\text{LiFePO}_4$  Batteries, *IEEE Transactions on Power Electronics*, 28(4) (2013), pp. 1555 - 1562.

[22] D. Anseán, M. González, J.C. Viera, V.M. García, C. Blanco and M. Valledor, Fast charging technique for high power lithium iron phosphate batteries: A cycle life analysis, *Journal of Power Sources*, 239 (2013), pp. 9 - 15.

[23] Y. D. Lee and S. Y. Park, Rapid Charging Strategy in the Constant Voltage Mode for a High Power Li-Ion Battery, *IEEE Energy Conversion Congress and Exposition (ECCE)*, (2013), pp. 4725 - 4731.

[24] B. K. Purushothaman and U. Landau, Rapid Charging of Lithium-Ion Batteries Using Pulsed Currents - A theoretical analysis, *Journal of Electrochemical Society*, 153(3) (2006), pp. A533-A542.

- [25] J. Li, E. Murphy, J. Winnick and P. A. Kohl, The effects of pulse charging on cycling characteristics of commercial lithium-ion batteries, *Journal of Power Sources*, 102(1-2) (2001), pp. 302 – 309.
- [26] B. K. Purushothaman, P. W. Morrison Jr. and U. Landau, Reducing Mass-Transport Limitations by Application of Special Pulsed Current Modes, *Journal of Electrochemical Society*, 152(4) (2005), pp. J33 – J39.
- [27] A. J. Bard and L. R. Faulkner, *Electrochemical Methods: Fundamentals and Applications* 2<sup>nd</sup> edition, Wiley, (2000), pp. 645 – 650.
- [28] G. S. Popkirov, A technique for series resistance measurement and ohmic-drop correction under potentiostatic control, *Journal of Electroanalytical Chemistry*, 359(1-2) (1993), pp. 97 – 103.
- [29] R. Saint-Pierre, A Dynamic Voltage-Compensation Technique for Reducing Charge Time in Lithium-Ion Batteries, *IEEE The 15<sup>th</sup> Annual Battery Conference on Applications and Advances*, (2000), pp. 179 - 184.
- [30] C. H. Lin, C. L. Chen, Y. H. Lee, S. J. Wang, C. Y. Hsieh, H. W. Huang and K. H. Chen, Fast charging technique for Li-Ion battery charger, *IEEE International Conference on Electronics, Circuits and Systems*, (2008), pp. 618 - 621.
- [31] C. H. Lin, C. Y. Hsieh and K. H. Chen, A Li-Ion Battery Charger With Smooth Control Circuit and Built-In Resistance Compensator for Achieving Stable and Fast Charging, *IEEE Transactions on Circuits and Systems - I: Regular Papers*, 57(2) (2010), pp. 506-517.
- [32] T. C. Huang, R. H. Peng, T. W. Tsai, K. H. Chen and C. L. Wey, Fast Charging and High Efficiency Switching-Based Charger With Continuous Built-In-Resistance Detection and Automatic Energy Deliver Control for Portable Electronics, *IEEE Journal of Solid-State Circuits*, 49(7) (2014), pp. 1580 – 1594.
- [33] R. H. Peng, T. W. Tsai, K. H. Chen, Z. H. Tai, Y. H. Cheng, C. C. Tsai, H. Y. Luo, S. M. Wang, L. D. Chen, C. C. Yang and J. L. Chen, Switching-based Charger with Continuously Built-in Resistor Detector (CBIRD) and Analog Multiplication-division Unit (AMDU) for Fast Charging in Li-ion Battery, *IEEE European Solid-State Circuits Conference (ESSCIRC)*, (2013), pp. 157 – 160.

[34] A. Nyman, T. G. Zavalis, R. Elger, M. Behm and G. Lindbergh, Analysis of the polarization in a Li-ion battery cell by numerical simulations, *Journal of The Electrochemical Society*, 157(11)(2010), pp. A1236-A1246.

[35] V. Srinivasan and C. Y. Wang, Analysis of electrochemical and thermal behavior of Li-ion cells, *Journal of The Electrochemical Society*, 150(1)(2003), pp. A98-A106.

[36] L. Song and J. W. Evans, Electrochemical-thermal model of lithium polymer batteries, *Journal of the Electrochemical Society*, 147(6)(2000), pp. 2086-2095.

[37] X. Zhang, Thermal analysis of a cylindrical lithium-ion battery, *Electrochimica Acta*, 56(3)(2011), pp. 1246-1255.

[38] H. Maleki, S. Al Hallaj, J. R. Selman, R. B. Dinwiddie and H. Wang, Thermal Properties of Lithium-Ion Battery and Components, *Journal of the Electrochemical Society*, 146(3)(1999), pp. 947-954.

[39] W. B. Gu and C.Y. Wang, Thermal-Electrochemical Coupled Modeling of Lithium-Ion Cell, *Electrochemical Society Proceedings*, 99(1)(2000), pp. 748 - 762.

[40] C. R. Pals and J. Newman, Thermal modeling of the lithium/polymer battery: I. Discharge behavior of a single cell, *Journal of the Electrochemical Society*, 142(10)(1995), pp. 3274-3281.

[41] C. R. Pals and J. Newman, Thermal modeling of the lithium/polymer battery: II. Temperature profiles in a cell stack, *Journal of the Electrochemical Society*, 142(10)(1995), pp. 3282-3288.

[42] W. B. Gu and C. Y. Wang, Thermal-electrochemical modeling of battery systems, *Journal of The Electrochemical Society*, 147(8)(2000), pp. 2910-2922.

[43] H. Maleki and J. N. Howard, Internal short circuit in Li-ion cells, *Journal of Power Sources*, 191(2)(2009), pp. 568-574.

[44] C. Forgez, D. V. Do, G. Freidrich, M. Morcrette and C. Delacourt, Thermal modeling of a cylindrical LiFePO<sub>4</sub>/graphite lithium-ion battery, *Journal of Power Sources*, 195(9) (2010), pp. 2961-2968.

[45] K. Onda, T. Ohshima, M. Nakayam, K. Fukuda and T. Araki, Thermal behavior of small lithium-ion battery during rapid charge and discharge cycles, *Journal of Power Sources*, 158(1) (2006), pp. 535-542.

[46] A. Barré, B. Deguilhem, S. Grolleau, M. Gérard, F. Suard and D. Riu, A Review on Lithium-ion Battery Ageing Mechanisms and Estimations for Automotive Applications, *Journal of Power Sources*, 241 (2013), pp. 680–689.

[47] S. Paul, C. Diegelmann, H. Kabza and W. Tillmetz, Analysis of Ageing Inhomogeneities in Lithium-ion Battery Systems, *Journal of Power Sources*, 239 (2013), pp. 642 – 650.

[48] J. Shim, R. Kostecky, T. Richardson and X. Song, Electrochemical Analysis for Cycle Performance and Capacity Fading of a Lithium-ion Battery Cycled at Elevated Temperature, *Journal of Power Sources*, 112 (2002), pp. 222 – 230.

[49] M. Safari and C. Delacourt, Aging of a Commercial Graphite/LiFePO<sub>4</sub> cell, *Journal of The Electrochemical Society*, 158(10) (2011), pp. A1123 - A1135.

[50] C. R. Birkl, M. R. Roberts, E. McTurk, P. G. Bruce and D. A. Howey, Degradation diagnostics for lithium ion cells, *Journal of Power Sources*, 341 (2017), pp. 373 - 386.

[51] S. S. Zhang, K. Xu and T. R. Jow, A thermal stabilizer for LiPF<sub>6</sub>-based electrolytes of Li-ion cells, *Electrochemical and Solid-State Letters*, 5(9) (2002), pp. A206–A208.

[52] N. Nagasubramanian, Comparison of the thermal and electrochemical properties of LiPF<sub>6</sub> and Li(SO<sub>2</sub>C<sub>2</sub>F<sub>5</sub>)<sub>2</sub> salts in organic electrolytes, *Journal of Power Sources*, 119-121 (2003), pp. 811 – 814.

[53] J. Garche, C. K. Dyer, P. T. Moseley, Z. Ogumi, D.A. J. Rand and B. Scrosati, *Encyclopedia of Electrochemical Power Sources, Secondary Batteries – Lithium Rechargeable Systems / Electrolytes: Nonaqueous*, Newnes, (2013), pp. 80-81.

# **Chapter 2: Experimental setup, materials, equipment and battery characterizations**

---



## 1. Introduction

The purpose of this chapter is to present different materials, instruments, methods and test protocols used throughout the study of fast charging Li-ion battery. Different battery technologies are used for the latter purpose and will be presented in this chapter. All of the batteries have their advantages and their own inconvenient. The charging methods and their protocols along with some electrochemical notions are also explained in this chapter. Besides that, the conception of a cooling test bench for heat evacuation of the battery cell will also be described here. Lastly, some analysis methodologies for post-mortem study are also described.

## 2. Lithium battery

In this study, three different 18650 Li-ion battery are used; graphite-lithium iron phosphate battery (C/LFP) by PHET, graphite-lithium nickel manganese cobalt oxide battery (C/NMC) by Samsung and lithium titanate oxide - lithium iron phosphate battery (LTO/LFP) also by PHET. Next section will describe more about their characteristics.

### 2.1. Lithium iron phosphate battery, C/LFP

The main Li-ion batteries used in this paper are C/LFP cells manufactured by PHET. C/LFP means that the two electrodes used in this battery are graphite for the negative electrode material and lithium iron phosphate for the positive electrode materials. The C/LFP battery was chosen because of its thermal stability, which allows it to undergo a fast charging process at high current. The nominal voltage for this battery is about 3.3V at open-circuit. The usage temperature ranges between 0°C to 45°C and -20°C to 60°C respectively during charge and discharge. The nominal capacity of these batteries is 1.1Ah. It must be pointed out that throughout this work; C-rate values are referred to the nominal capacity. Manufacturer claims that this battery can perform fast charging process up until 4C-rate using the normal method of CCCV. **Table 2.1** recapitulates the characteristics of the battery.

**Table 2.1:** 18650 C/LFP characteristics (PHET)

Type	C-LiFePO <sub>4</sub>
Dimensions	65mm x 18mm
Weight	41g
Nominal Capacity	1100mA.h
Nominal voltage	3.2 – 3.3V
Standard charge	3.65V ; 1C (1.1A) ; 10mA cut-off
Standard discharge	1.5C (1.65A) ; 2V cut-off
Fast charging	4C (4.4A) ; 10mA cut-off
Temperature ranges	0 to 45°C (charge) and -20 to 60°C (discharge)

## 2.2. Nickel manganese cobalt oxide battery, C/NMC

The C/NMC cells are the second technology of battery used in this study. The main difference is the material used for the positive electrode that consists of nickel manganese cobalt oxide. This type of battery is also widely used in the EVs or HEVs and also for remote energy storage. Its nominal capacity is a little higher at about 1500mA.h compared to C/LFP battery cell. This battery from Samsung is rated for fast-charging purposes until a current of 4A which is roughly at 2.67C-rate. Other details regarding the battery characteristic can be found in the **Table 2.2**.

**Table 2.2:** 18650 C/NMC characteristics (Samsung)

Type	C-LiNiMnCoO <sub>2</sub>
Dimensions	64.85mm x 18.15mm
Weight	45g
Nominal Capacity	1500mA.h
Nominal voltage	3.6V
Standard charge	4.2V ; 0.5C (0.75A) ; 100mA cut-off
Standard discharge	1C (1.5A) ; 2.5V cut-off
Fast charging	4A ; 100mA cut-off
Temperature ranges	0 to 45°C (charge) and -20 to 60°C (discharge)

### 2.3. Lithium titanate oxide - lithium iron phosphate battery, LTO/LFP

The third type of the Li-ion battery that is used in this study is the lithium titanate oxide - lithium iron phosphate battery (LTO/LFP) manufactured by PHET. This time around the main difference lies on the material used for the negative electrode which is the lithium titanate oxide (LTO). The battery cell still uses lithium iron phosphate as its positive electrode. Its nominal capacity is just a little bit lower at about 1000mA.h compared to C/LFP battery cell. The most interesting characteristic of this battery is its fast charging capability suggested by the manufacturer. Indeed, it is listed that the battery can manage fast charging process up to 10C-rate, which is roughly at 10A. However, its nominal voltage is the lowest if compared to the two other batteries. All other characteristics concerning this LTO/LFP battery could be found in **Table 2.3**.

**Table 2.3:** 18650 LTO/LFP characteristics (PHET)

Type	LTO-LiFePO <sub>4</sub>
Dimensions	65mm x 18mm
Weight	39g
Nominal Capacity	1000mA.h
Nominal voltage	1.8V
Standard charge	2.4V ; 1C (1A) ; 10mA cut-off
Standard discharge	1C (1A) ; 1.1V cut-off
Fast charging	10C (10A) ; 10mA cut-off
Temperature ranges	0 to 45°C (charge) and -20 to 60°C (discharge)

## 3. Battery test bench, characterization and charging methods

### 3.1. Test bench

The potentiostat system used in this study is a VSP type coupled with a booster of 2A, 5A or 20A manufactured by the Bio-Logic Science Instrument Company. This potentiostat is controlled by the EC-Lab software which is used to setup the charging and discharging protocol. The connection between the battery and the potentiostat is fixed by a C-clamp. To keep track of the thermal behaviour of the Li-ion battery during the study, a Pt100 probe is fixed on the outer surface. A climatic chamber is used to control the surrounding temperature of the battery. The illustration of these materials and their configuration is shown in **Fig. 2.1**.



**Figure 2.1:** (a) Computer, potentiostat and the climatic chamber and (b) Connection's configuration of the Li-ion battery throughout the study.

### 3.2. Charging and discharging protocols

For all those three types of battery presented earlier, three charging methods are used in this study. Firstly, the reference charging method in which the battery is charge at reference C-rate with an upper-bound voltage limit,  $U_f$  (both given by the manufacturer). Secondly, the standard or normal method, which is exactly the same as the reference method but which runs at different or higher C-rate. The standard/reference charging process involves two charging stages: a constant current stage (CC) and constant voltage stage (CV). During the CC stage, the battery is charged at a chosen constant current (i.e. charging C-rate) until a certain upper-bound voltage limit,  $U_f$  is reached before switching to CV stage. As said earlier, the upper-bound voltage limit,  $U_f$  is predetermined by the manufacturer and it is designed to ensure longer battery life-span by minimizing side reactions. During the CV stage, the battery is normally charged slower with a degrading current to maintain the battery at a constant voltage until the current limit called I cut-off, is attained. Lastly, the third method it the ohmic-drop compensation (ODC) charging method, in which the battery is charged at C-rate ranging from 1 C-rate and up to 15 C-rate, until a new upper-bound voltage limit of  $U'_f$ , taking into account the measured ohmic-drop resistance,  $R_i$  of the battery where:

$$U'_f = U_f + \alpha R_i I \quad (2.1)$$

It is worth mentioning that the CV stage is always performed at upper-bound voltage limit,  $U_f$  given by the manufacturer until the cut-off current whatever the charging method. After each charging process, the battery is discharged at a constant current using reference discharge method given by the manufacturer until the lower-bound cut-off voltage is reached. When this cut-off voltage is reached, the discharging process is finished. The relax time between charges/discharges is set at 1

hour for the battery to cool down before launching another test. **Fig. 2.2** depicts the voltage and current curves of the batteries during their reference charge and discharge cycling.

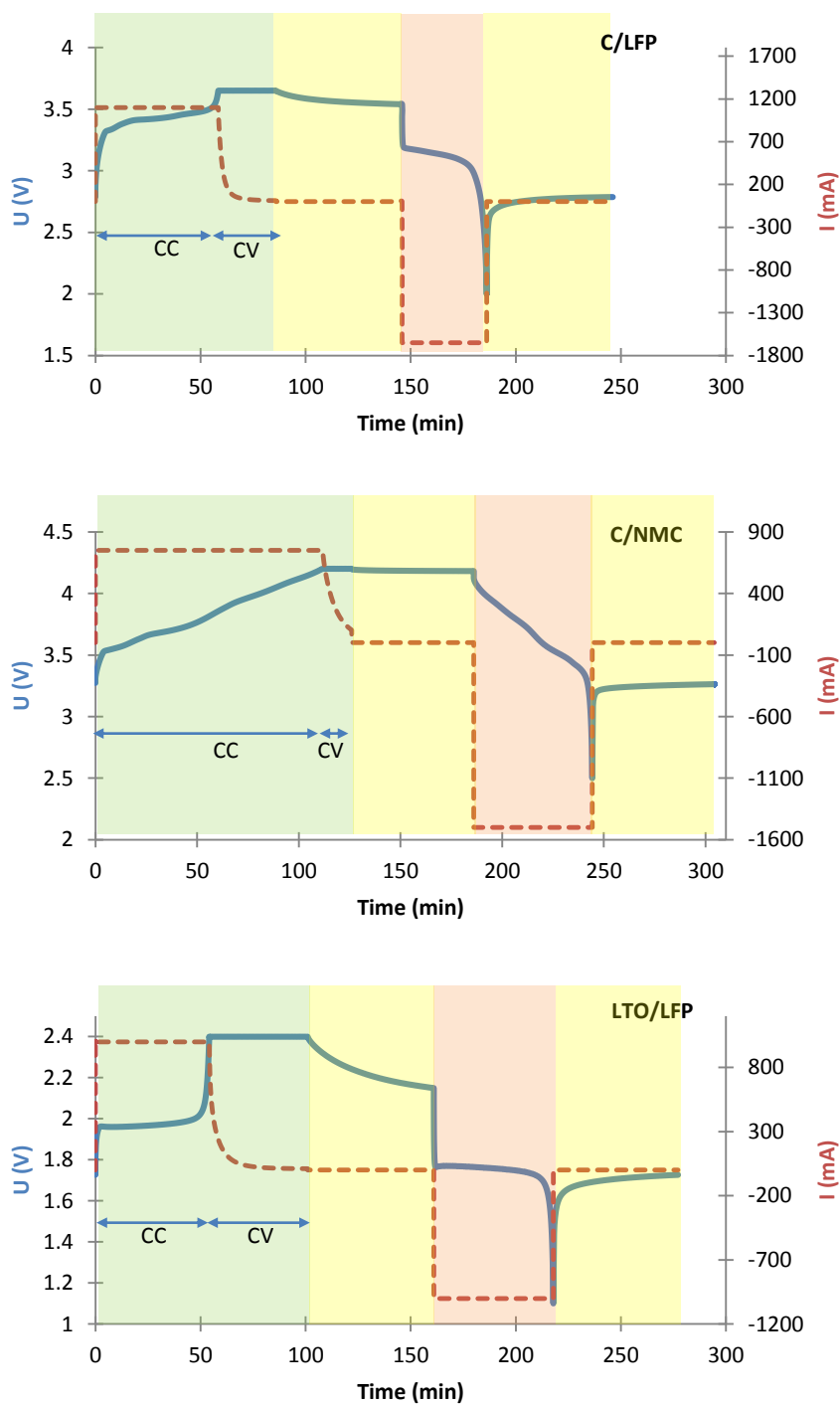


**Figure 2.2:** Voltage and current curves of C/LFP, C/NMC and LTO/LFP battery during their reference charging process, relax period and reference discharging process.

In these graphics above, the reference charging process, relax period and the reference discharging process are colour coded. Green, yellow and orange areas represent the charging, relax and

discharging periods respectively. Moreover, CC and CV stages are also outlined for each charging process. C/LFP battery is normally charged until 100% of SOC in about 90 min, C/NMC battery in about 125 min and LTO/LFP in about 100 min. As shown, the form of the curves of C/LFP and LTO/LFP battery is quite similar. This is mainly the case because of the similarity of the active materials used for their positive electrode. They also show the classical voltage plateau for LFP based battery at about 3.3 V for C/LFP and 1.9V for LTO/LFP. Contrariwise, the voltage and the current curves of C/NMC battery are portrayed in a completely different form, both during charging and also during discharging. Additionally, the CV stage during its reference charging process is notably short compared to others. Whatever the duration, the CV stage is still a crucial stage where the battery is being charged slowly until the battery reaches its full state of charge.

### 3.3. Battery characterizations

#### 3.3.1. Internal resistance

The current interrupt (CI) technique in the EC-Lab software by BioLogic is used to facilitate the value acquisition. The internal resistance,  $R_i$  is then determined at the beginning of the charge, during the steep change of the current from 0 to 400mA for 10 to 15 impulsions. Then, the average value of the internal resistance is calculated. **Fig. 2.3** shows an example of this CI technique for the C/LFP battery.

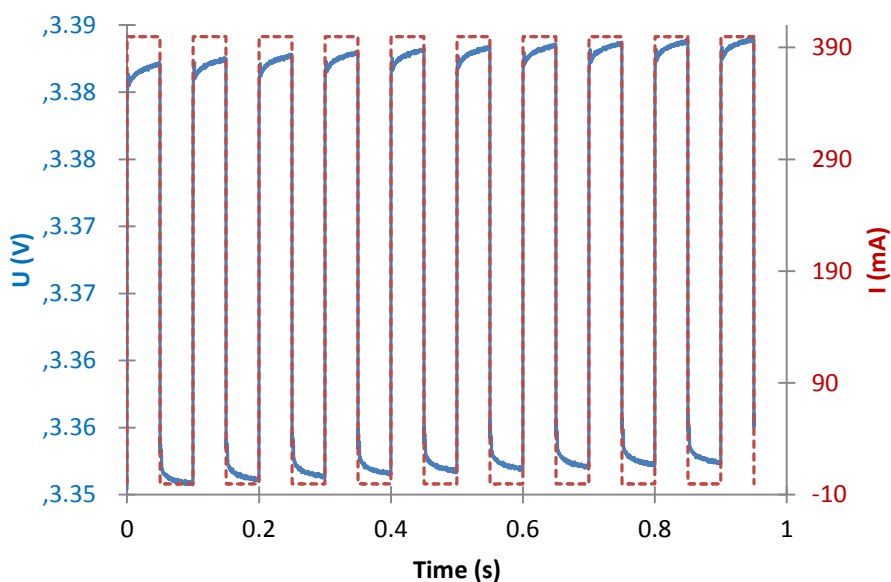


**Figure 2.3:** Example of CI (Current Interrupt) technique in the EC-Lab for the C/LFP battery

The internal resistance,  $R_i$  is estimated at 0.05 ms (i.e approximately 20 kHz) as:

$$R_i = \frac{V_{t=0s} - V_{t=0.05ms}}{I_{t=0s} - I_{t=0.05ms}} \quad (2.2)$$

The internal resistance measured at high frequency corresponds to ohmic contribution induced by the charge transport in each volume of cell elements (current collectors, electrolyte and connections).

In this paper, the internal resistance is measured at ambient temperature which is about 25°C and it is also important to point out that the internal resistance varies from one battery to another. **Table 2.4** represents the average value of the internal resistance measured for all three types of battery used in this study.

Battery types	Average internal resistance measured, $R_i$ (mΩ)
C/LFP	75
C/NMC	30
LTO/LFP	53

Furthermore, there is no significant variation of the internal resistance at different temperature and SOC. **Fig. 2.4** below depicts the internal resistance of C/LFP battery for two different temperature at different SOC.

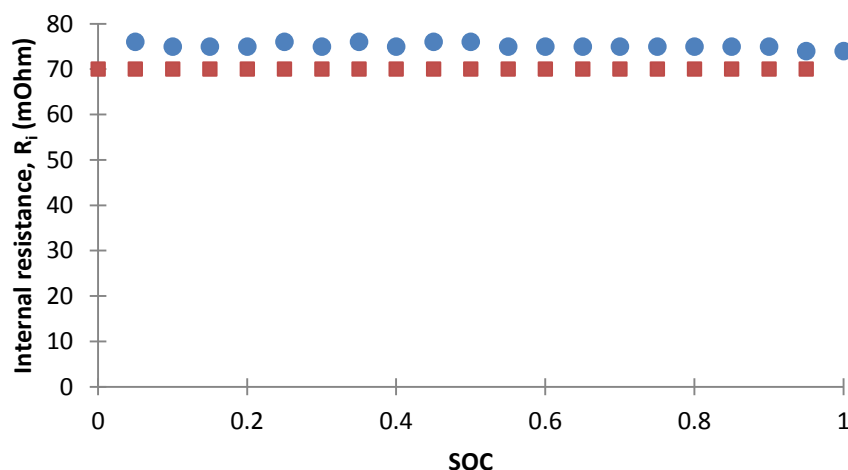


**Figure 2.4:** Internal resistance of C/LFP battery at (a) 25°C ● and (b) 45°C ■ at different value of SOC

### 3.3.2. State Of Charge, SOC

On one hand, the state of charge, SOC is an indication of quantity of electricity remaining in the battery. The SOC is determined as the ratio between the amount of remaining electricity and the nominal capacity of the battery itself. This SOC is determined using the reference discharge method during the cycling.

$$SOC = \frac{Q_{Remaining}}{Q_{Nominal}} \quad (2.3)$$

### 3.3.3. State Of Health, SOH

On the other hand, the state of health (SOH) of a battery which is an indication of wear and tear on a battery is related to the capacity decrease of the battery. It is obtained by calculating the ratio between the actual discharge capacity and the initial discharge capacity of the battery:

$$SOH = \frac{Q_{discharge,act}}{Q_{discharge,init}} \quad (2.4)$$

Where  $Q_{discharge,act}$  is the actual discharge capacity of the battery cell (Ah) and  $Q_{discharge,init}$  the initial discharge capacity of the battery (Ah) measured in the standard discharge condition.

### 3.3.4. Energy and coulombic efficiencies

There are two types of efficiency that are being examined during this study; the Coulombic Efficiency (CE) and the Energy Efficiency, (EE). The first one is the Coulombic Efficiency which is defined as a ratio between the discharged capacity measured at reference discharge C-rate and the charged capacity for different C-rates:

$$CE = \frac{\text{Discharged capacity}}{\text{Charged capacity}} = \frac{\int I(t).dt_{discharged}}{\int I(t).dt_{charged}} \quad (2.5)$$

And the other one is the Energy Efficiency which is also similarly defined as the ratio between the discharged energy at reference discharge C-rate and the charged energy for different C-rates:

$$EE = \frac{\text{Energy recovered during discharged}}{\text{Energy supplied during charged}} = \frac{\int U(t).I(t).dt_{discharged}}{\int U(t).I(t).dt_{charged}} \quad (2.6)$$

## 4. The ventilation test bench: Conception of the air canal

### 4.1. Air canal characteristics

In order to cool Li-ion battery, it is necessary to develop a ventilation system (air canal) capable of cooling down the latter to be able to study the influence of the temperature on its parameters. The test bench is created using these following elements:

- A DC fan Axial Fans model 3110KL-04W-B50 (cooling fan of computer CPU)
- A structure made of wood

The air canal has a dimension approximately of 85mm x 85mm x 340mm. The following **Fig. 2.5** shows the configuration of the test bench of the air canal:

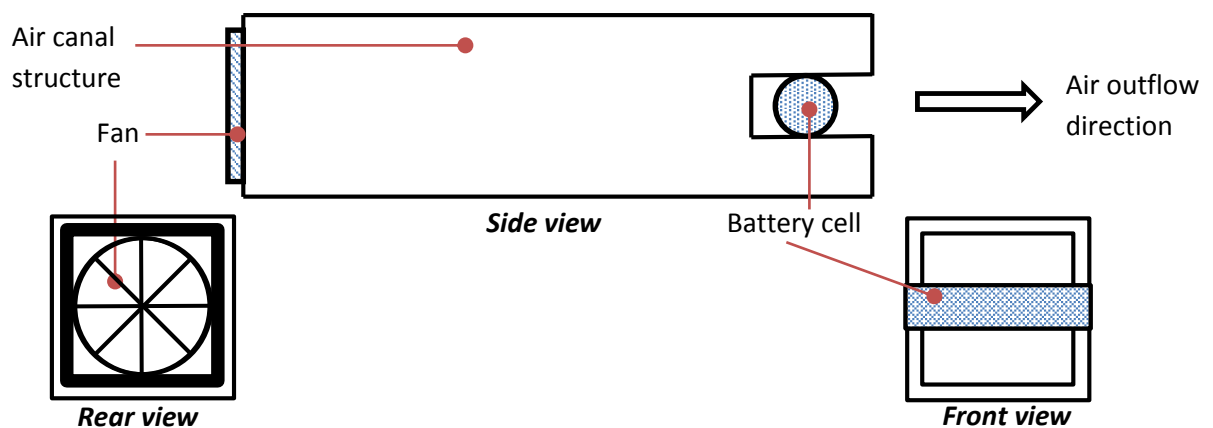


**Figure 2.5:** Schematic diagram of the air canal installation

This air canal is not optimal; the aim here is to be able to carry out a feasibility study. In this study, the air canal forces an air flow towards the battery cell in order to limit the heating of the latter during its charging process. Through the results, it is possible to estimate the influence of air flow velocity on the battery temperature during fast-charging using the ODC method principally.

## 4.2. Air flow measurements

In order to determine the air flow type, a preliminary study of the air flow must be carried out. These air flow velocity measurements are carried out using an anemometer which is located at different distances from the fan at its maximum rotation speed in order to determine whether the air flow is established or not at the output of the air canal. The average air flow velocities along the channel length are presented in **Fig. 2.6**.

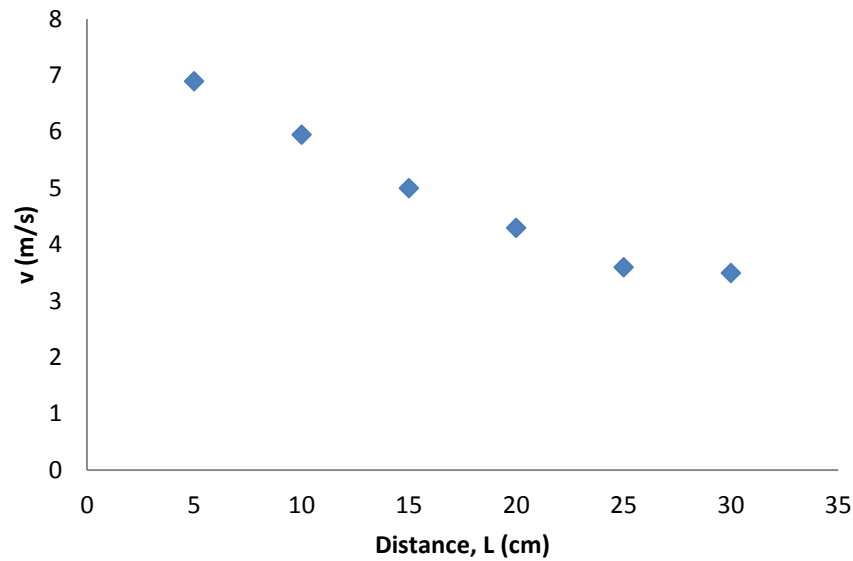


**Figure 2.6:** Determination of air flow velocity inside the canal

The air flow regime is visibly established at about 25cm away from the fan. This distance will be the reference point chosen as the location of the battery inside the air canal.

**Fig. 2.7** shows the air velocity change with the input electric power at  $L=25\text{cm}$  where the battery cell is located.

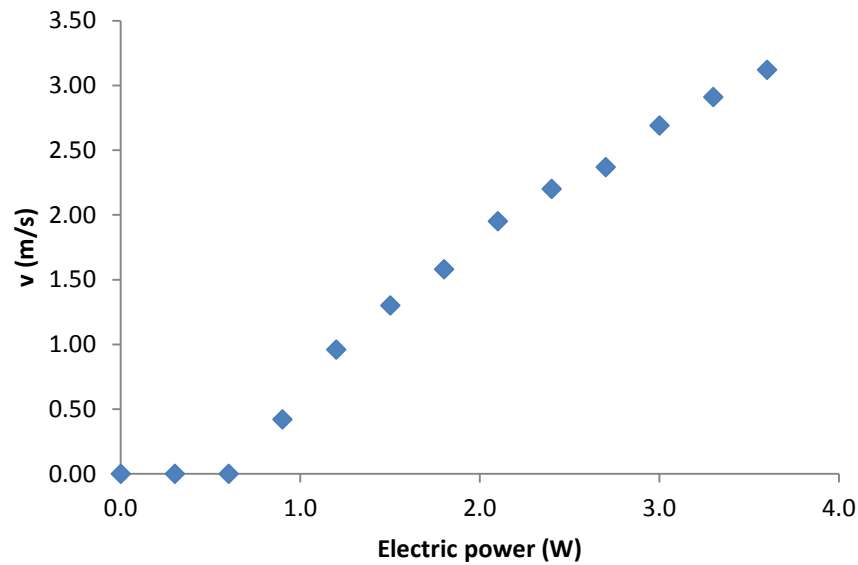


**Figure 2.7:** Air flow velocity as functions of the input electric power of the fan (L=25cm)

The vertical air flow velocity profile is also determined by using the anemometer at L = 25 cm. The velocity is measured at different heights, H from the bottom to the top of the air canal. The air flow profile is presented in the **Fig. 2.8**.

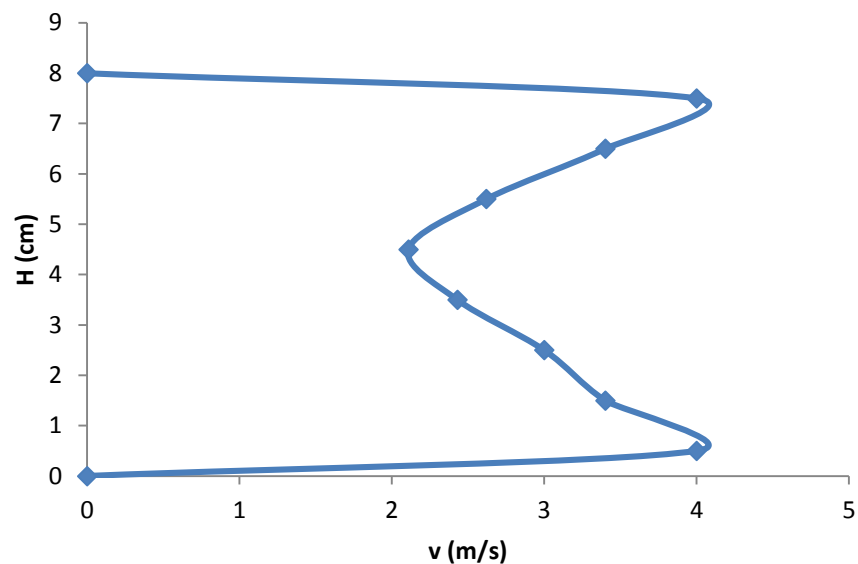


**Figure 2.8:** Air flow profile at L = 25 cm with maximum fan power output

The air flow velocity profile in **Fig. 2.8** shows that there are three different "drop" of air flow. Close to the air canal walls the velocity becomes equal to zero due to friction. The air flow velocity strongly depends on the geometry of the fan. Indeed, the axial fan which is used to cool down a computer

CPU, consists of an electric motor at the center. So, the air circulating at the center of the air canal will have a lower velocity than elsewhere inside the air canal (excluding at the extremities of the air canal walls). The battery undergoes air velocity from 2 to 4 m/s

### 4.3. Determination of heat transfer coefficient by forced convection

In order to determine the heat transfer coefficient of forced convection, three dimensionless numbers are used:

- Reynolds number
- Prandtl number
- Nusselt number

The calculation of the Reynolds number is necessary in order to determine the dynamic air flow pattern of the air inside the canal. The latter is calculated using the equation below:

$$Re = \frac{\rho v L_c}{\mu} \quad (2.7)$$

Where  $\rho$  is the air density,  $v$  is the air velocity,  $\mu$  is dynamic viscosity and  $L_c$  is the characteristic dimension, in this case the battery cell diameter.

At full power, the air flow delivered by the fan is high enough to observe a turbulent flow regime ( $Re > 5000$ ), which will help to maximize the heat exchanges.

The Prandtl number on the other hand indicates whether or not the fluid environment has a proportional relationship between its temperature profile and its velocity profile. It is calculated as follows:

$$Pr = \frac{\mu C_p}{\lambda} \quad (2.8)$$

Where  $C_p$  is the specific heat capacity and  $\lambda$  is the heat conductivity of air.

In the case of air, the Prandtl number is very small (i.e. 0.71 considering the properties are taken at ambient temperature).

Finally, the Nusselt number represents the proportion of heat exchange between the conductive and convective heat transfer. It is calculated by this relation below:

$$Nu = \frac{h.L_c}{\lambda} \quad (2.9)$$

Where  $h$  is the heat transfer coefficient.

The Nusselt number used here is calculated using the *Churchill-Berstein* correlation [1]. Note that this correlation is only valid when  $Re.Pr \geq 0.2$  which is the case in this study:

$$Nu = 0,3 + \frac{0,62.Re^{1/2}.Pr^{1/3}}{\left[1 + \left(\frac{0,4}{Pr}\right)^{2/3}\right]^{1/4}} \cdot \left[1 + \left(\frac{Re}{282000}\right)^{5/8}\right]^{4/5} \quad (2.10)$$

**Fig. 2.9** below depicts the value of heat transfer coefficients for different values of the mean air flow velocity enforced by the fan. Note that, at full fan power, the forced convection heat transfer coefficient is about  $44.0 \text{ W / m}^2$ .

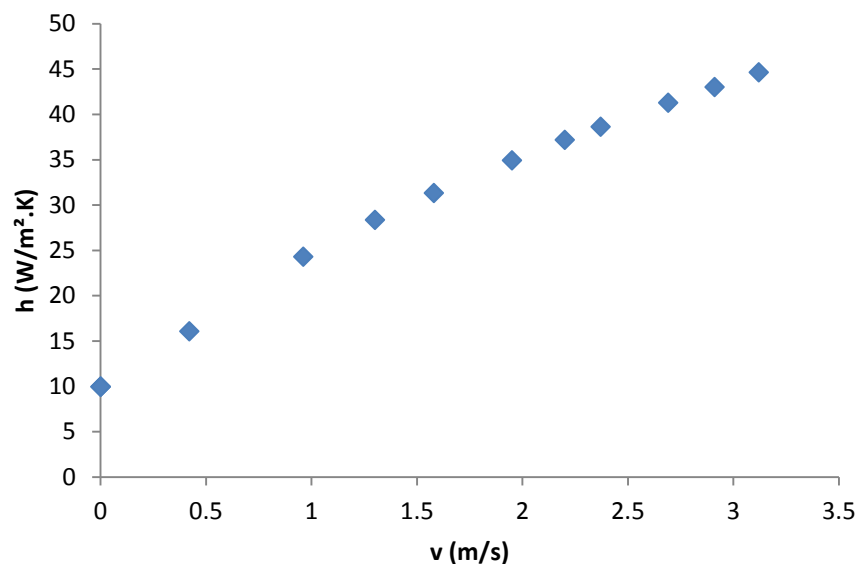


**Figure 2.9:** heat transfer coefficients at different air velocity ( $L=25\text{cm}$ )

## 5. Determination of heat capacity of C/LFP and the heat transfer coefficient inside climatic chamber

Thermal characterizations were carried out using the battery cell itself as well as a bar of copper metal having the same dimensions. These experiments are performed in order to estimate the convective heat transfer coefficient,  $h$  inside the climatic chamber and the “effective” specific heat

capacity,  $C_p$  of the battery. These values are needed for the thermal simulation studies and the results of the latter are presented in **Chapter 4**. Both systems underwent a multiple echelon of temperature inside the climatic chamber and the temperature variation was recorded as a function of time.

Considering that no heat production takes place, some assumptions were also considered for the resolution the differential equation:

- The battery cell/copper bar are considered as thermally thin (low value of Biot number),
- The values of specific heat capacity,  $C_p$  and also heat transfer coefficient,  $h$  are assumed independent to the temperature.

The model used to fit the experimental data is similar to the one presented in the **Section 3** of **Chapter 4** considering no heat sources. The ordinary differential equation is solved considering:

- Initial condition: at  $t = 0$  seconds, the battery cell/copper bar temperature is  $T(0) = T_i$
- Final condition: when  $t \rightarrow \infty$ , the battery cell/copper bar temperature is  $T(\infty) \rightarrow T_a$

The resolution of the differential equation (**Eq. 4.12**) gives the theoretical temperature change with time [2]:

$$T(t) = T_a + (T_i - T_a)e^{-\frac{hS}{mC_p}t} \quad (2.11)$$

$T(t)$  being the temperature of battery cell/copper bar as a function of time,  $T_a$  the climatic chamber temperature,  $T_i$  the initial temperature of battery cell/copper bar,  $S$  the lateral surface area of the battery cell/copper bar,  $m$  the mass of the battery cell/copper bar and  $t$  the time.

Log-linearization method is used to solve and analyze the non-linear temperature data acquired of both the copper bar and battery cell:

$$\ln \frac{(T(t)-T_a)}{(T_i-T_a)} = -\frac{hS}{mC_p}t \quad (2.12)$$

First, the heat transfer coefficient inside the climatic chamber,  $h$  is deduced from the slope of the line in **Fig. 2.10a** for the copper bar because the specific heat capacity is well-known for this material and equal to  $385 \text{ J}/(\text{kg}\cdot\text{K})$ . Second, the “effective” specific heat capacity,  $C_p$  is deduced from the slope of the line in **Fig. 2.10b** for the battery cell. It is then assumed that the heat transfer coefficient,  $h$ , is the same for the copper bar and the battery.

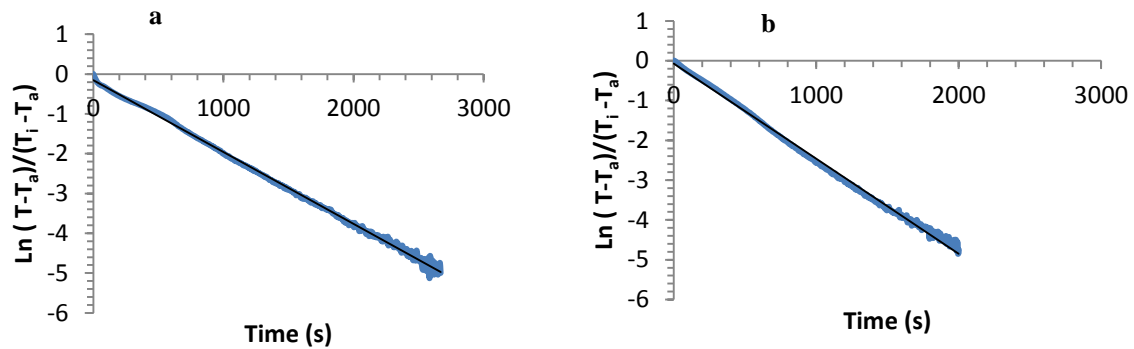


**Figure 2.10:** Example of log-linearized surficial temperature — of a) copper bar and b) battery cell for an echelon of temperature from ambient temperature to  $50^\circ\text{C}$

The corresponding heat transfer coefficient and specific heat capacity of the C/LFP battery values obtained in this study are summarized in **Table 2.5**.

<b>Table 2.5.</b> Values of $C_p$ and $h$	
Heat exchange coefficient inside climatic chamber, $h$ [ $\text{W}\cdot\text{m}^{-2}\cdot\text{K}^{-1}$ ]	27
Specific heat capacity of the battery cell, $C_p$ [ $\text{J}\cdot\text{kg}^{-1}\cdot\text{K}^{-1}$ ]	992

Compared to the literatures, our value of specific heat capacity for C/LFP battery is not far off. For example *M. Fleckenstein et al.* [3] measured the specific heat capacity of their C/LFP battery using Thermal Impedance Spectroscopy (TIS) and they found the value of about  $958 \text{ J}\cdot\text{kg}^{-1}\cdot\text{K}^{-1}$ . Another example is from *E. Prada et al.* [4] who manage to measure about  $1100 \text{ J}\cdot\text{kg}^{-1}\cdot\text{K}^{-1}$  for specific heat capacity of their C/LFP battery.

## 6. Post-mortem analysis methodology

These experiments were performed in collaboration with Xavier Fleury from CEA Grenoble.

### 6.1. X-ray tomography

The X-ray tomography scans were performed on the batteries using a NANOTOM 180S Phoenix (GE Technologie). The batteries were rotated 360° about their long axis whilst 1500 projections were captured with the focus tube operating at 120 kV and 130  $\mu$ A. The sample and detector were positioned in projection magnification providing an effective pixel size of 24.42  $\mu$ m for the high resolution imaging.

### 6.2. SEM Analysis

SEM was used to investigate the surface of the electrodes. Multiple areas per sample were analyzed in an LEO 1530 Gemini from Zeiss (Germany) without additional treatments at an acceleration voltage of 5 kV.

### 6.3. Gaseous Chromatography analysis

GC/MS spectroscopy was carried out with an Agilent 5975C Series GC/MSD using GC/MSD ChemStation software. The chromatographic separation was performed on a "DB200" Trifluoropropyl-methylpolysiloxane based capillary column (30 m  $\times$  0.25 mm i.d., 0.25  $\mu$ m) from SGE. All products could be identified clearly with the National Institute of Standards (NIST) 08 library. 1  $\mu$ L of the diluted samples (30:100, ACN) was injected at a temperature of 280°C. The system was run with helium as carrier gas with a column flow of 1.2 mL.min<sup>-1</sup>, a split of 1:100 and the following column oven program: starting with 40°C for 4.36 min, the temperature was increased with a rate of 10°C.min<sup>-1</sup> to 250°C and held for 2 min. It was measured in the electron ionization mode at an ion source temperature of 230°C, a filament voltage of 70 V, a detector voltage, which was chosen relative to the particular tuning result ( $\approx$ 1 kV) in a range of 10-350 m/z with an increment of 4.15 scan.s<sup>-1</sup> and a GC-MS interface temperature of 250°C.

#### 6.4. Electrochemical characterization with coin cell

Finally, electrochemical tests were performed with coin half-cells consisting of graphite-based electrode and LFP-based electrode (Diameter=16 mm) harvested from the commercial cell and Celgard® 2400 separator (Diameter=18.5 mm) with a metal lithium electrode (16 mm) in 1:1:1 wt EC:DMC:EMC + 1M LiPF<sub>6</sub> electrolyte. The capacity of lithium de/re-intercalation into both graphite and LFP electrodes recovered from aged cells is investigated with coin half-cells. Charge and discharge cycling were carried out at 0.1 C-rate in order to know their own capacities and compare their performances to the full-cells ones.

### 7. References

- [1] S. W. Churchill, M. Bernstein, A Correlating Equation for Forced Convection From Gases and Liquids to a Circular Cylinder in Crossflow, *Journal of Heat Transfer, ASME*, 99(2) (1977), pp. 300–306.
- [2] J.F. Sacadura, *Initiation aux transferts thermiques*, Technique et Documentation (1980)
- [3] M. Fleckenstein, S. Fischer, O. Bohlen, B. Bäker, Thermal Impedance Spectroscopy-A method for the thermal characterization of high power battery cells, *Journal of Power Sources*, 223 (2013), pp. 259-267.
- [4] E. Prada, D. Di Domenico, Y. Creff, J. Bernard, V. Sauvant-Moynot, F. Huet, Simplified electrochemical and thermal model of LiFePO<sub>4</sub>-graphite Li-ion batteries for fast charge applications. *Journal of the Electrochemical Society*, 159(9) (2012), pp. A1508-A1519.



# Chapter 3: Fast-charging of Li-ion batteries

---



## 1. Introduction

Developing fast-charging protocols for Li-ion batteries is a key issue for a wider deployment of electric vehicles and portable electrical devices. In this chapter, fast-charging of lithium-ion batteries is investigated with different protocols namely the normal CCCV method and ohmic-drop compensation, ODC method. For the latter, high charging rates are used for both methods ranging from 1C-rate up to 15C-rate depending on the battery technology. The protocol details for both methods have been presented beforehand in **Chapter 2**. As a reminder, the ODC method can be carried out with an extended constant current period thanks to a higher limit voltage based on the ohmic-drop compensation principle. This chapter will put forward all of the results comparisons for both fast charging procedures in term of charging time and also thermal behavior. Comparisons of the effectiveness of the fast charging ODC method between the batteries are also set forth.

## 2. Fast charge process for C/LFP battery

In this section, the influence of the fast-charging process with or without ODC on C/LFP battery is evaluated regarding charging duration and thermal behaviour. All of the characteristics of this battery can be found in **Table 2.1** of **Chapter 2**.

### 2.1. Fast charge of the battery with normal method

**Fig. 3.1** shows the current/cell voltage curves and the SOC evolution during charging process at 6C-rate and 2C-rate without ODC respectively using normal CCCV method (normal method).

It can be observed in **Fig. 3.1** that even the charging C-rate is increased from 2C up to 6C, the total charging time is slowly decreased from 56 min down to 48 min respectively. Indeed, at 6C-rate the CC stages are extremely short compared to one at 2C-rate. Namely, the CC stage lasts only about 6 seconds at 6C-rate against about 28 min at 2C-rate. This latter phenomenon is related to the larger contribution of the ohmic drop when the current increases. That means that the battery charging process is performed totally at CV stage when the C-rate becomes too high (i.e. 6C-rate). It is important to note that during its CV stage, the current stays around 3-4 A (i.e. 3 or 4C-rate) during more than 15 minutes before a large drop.

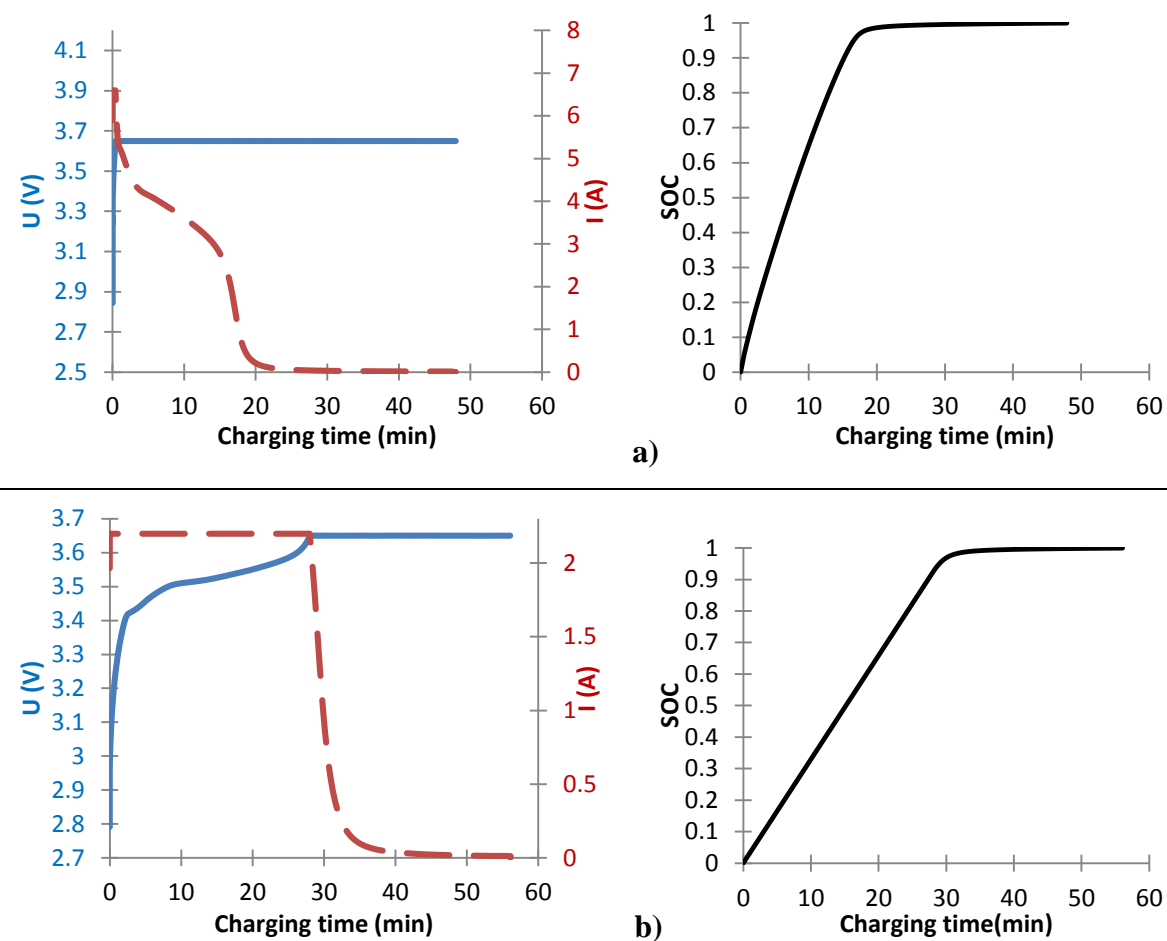


**Figure 3.1:** Current - cell voltage and SOC variation during charging process (normal method) at (a) 6C-rate and (b) 2C-rate.

As shown in **Fig. 3.2**, throughout this study of C/LFP battery, the charging processes are tested for C-rate ranging from 1C to 9C. The total charging time decays when the charging rate increases before reaching a plateau value for C-rate higher than 4C-rate. Charging rate higher than 4C-rate has approximately the same total charging time of about 45 to 48 minutes because the charging process always occurs only under CV condition whatever the CC rate. This observation is in agreement with the manufacturer information affirming that the battery could be fast charge at 4C.

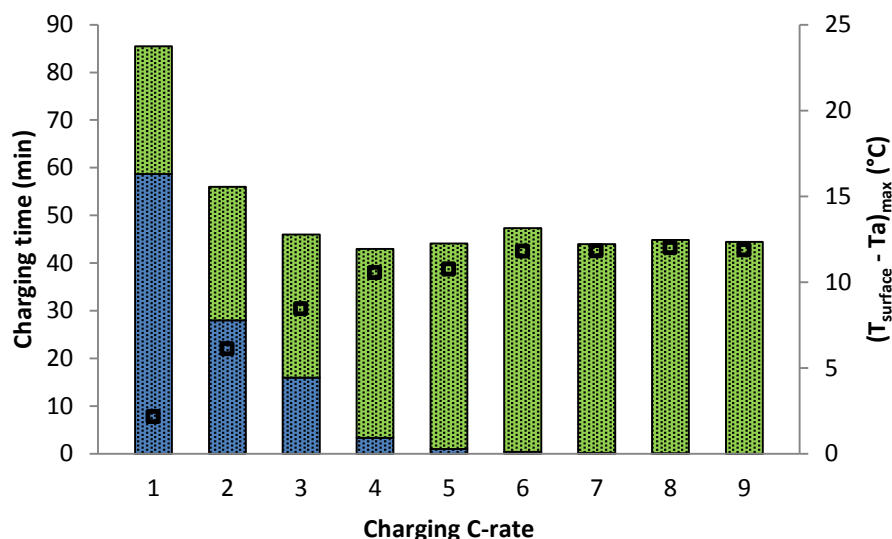


**Figure 3.2:** Charging time until 100% of SOC for normal method. CC stages are in the blue color while CV stages are in the green color.  $\square$  is the maximum outer surface temperatures elevation of the cell ( $T_a=25^\circ\text{C}$ ).

For fast charging with normal method, the maximal temperature rises until 4C-rate before reaching a plateau value of  $37^\circ\text{C}$ . For a C-rate larger than 4C, the charging process is mainly performed during the CV stage (see **Fig. 3.2**) with a similar current profile that contributes to comparable maximum temperature elevation.

## 2.2. Fast charge process of the C/LFP battery with ODC

### 2.2.1. High level ODC

**Fig. 3.3** represent respectively the current/cell voltage curves and the SOC evolution during fast charging at 6C-rate and 2C-rate with the ODC method (with  $\alpha = 93\%$ ). For 6C-rate, the total charging time drops to 25 minutes with the ODC method while it is about 48 minutes for the normal method presented in the above section. However, for 2C-rate, the total charging time is almost the same using both methods (i.e. 58 min for the normal method and 56 min with the ODC method).

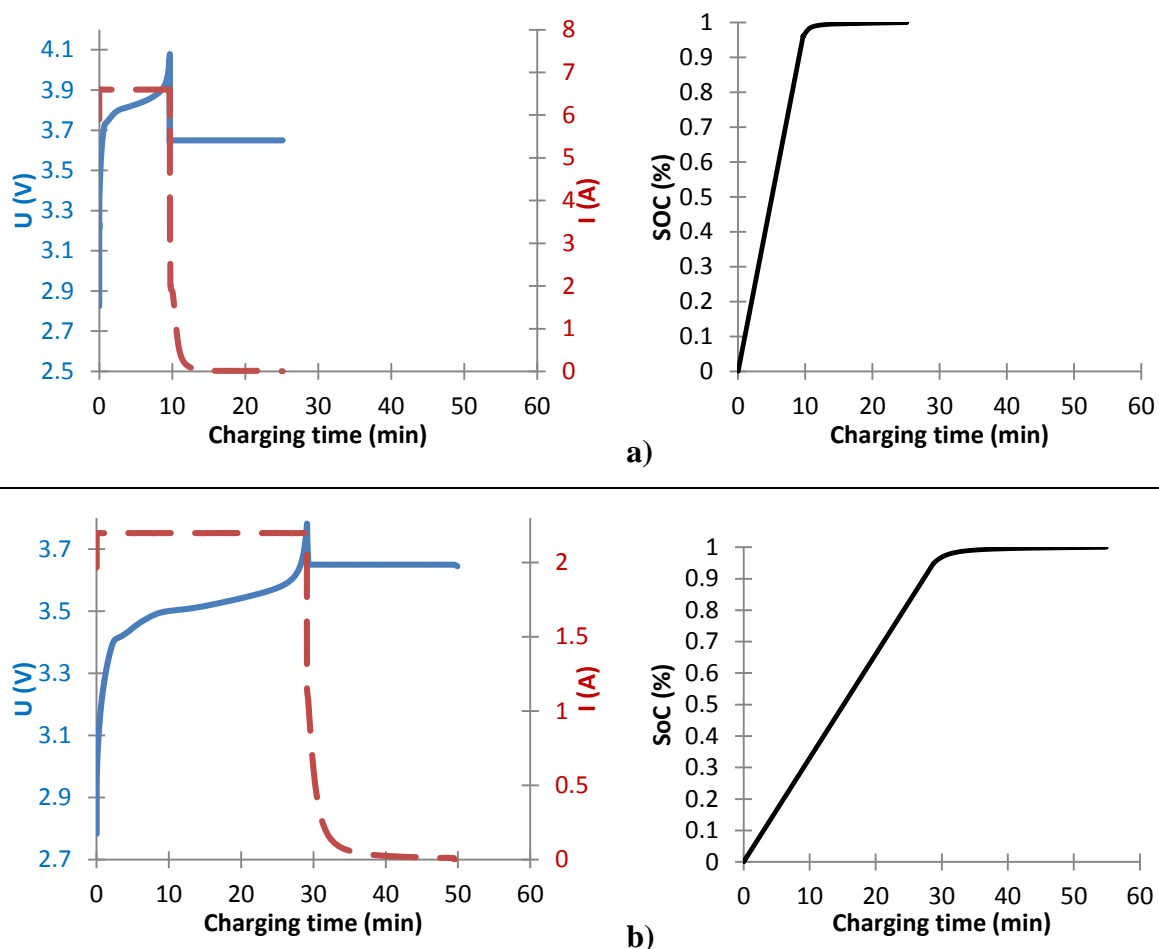


**Figure 3.3:** Current - cell voltage and SOC variation during charging process at (a) 6C-rate and (b) 2C-rate using high level ODC method. The CC stage forms a straight line for the SOC because the current applied is constant.

At 6C-rate, the fast charging process is performed partly during CC stage for a period of about 10 minutes whereas the CV stage lasts for 15 minutes with ODC method. This latter method is able to overcome the issue observed with the normal method and the total charging time decreases when the C-rate increases beyond 4C-rate as shown in (Fig. 3.4). Indeed, the CC stage remains long enough to charge partially the battery whatever the C-rate. As a consequence, the period of CV stage remains lower even at high charge regime. However, for C-rate lower than 4C, fast charge with ODC method has no impact on the total charging time. Fig. 3.4 recapitulates the comparison of both methods in terms of charging time and temperature at different charging rates.

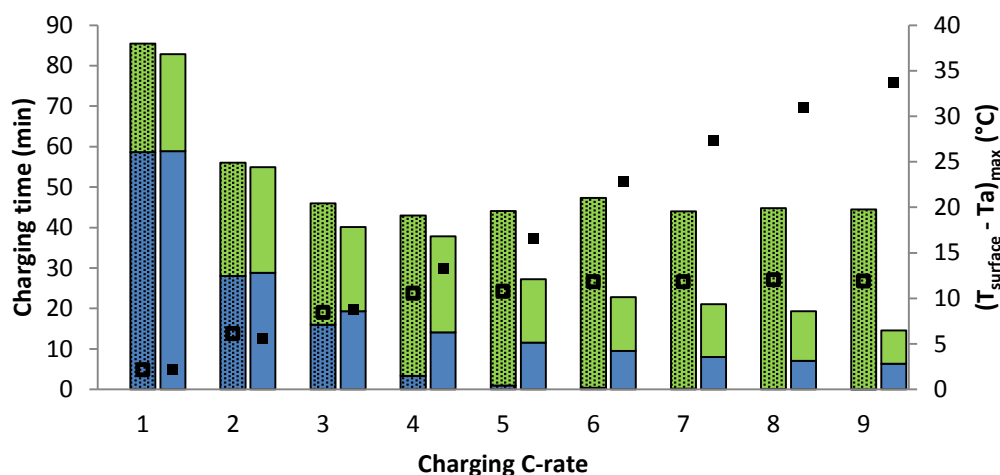


**Figure 3.4:** Charging time until 100% of SOC for normal method (left) and ODC method (right) for 1C-rate until 9C-rate. CC stages are in the blue color while CV stages are in the green color.  $\square$  and  $\blacksquare$  are the maximum outer surface temperatures elevation of the cell for both methods ( $T_a=25^\circ\text{C}$ ).

Nevertheless, the temperature of the battery rises from  $25^\circ\text{C}$  up to  $60^\circ\text{C}$  for ODC method when the C-rate ranges from 1C to 9C principally due to the joule effect proportional to the current applied during the CC stage. The temperature rises are well beyond the constructor limit of  $45^\circ\text{C}$  from C-rate higher than 6C with the ODC method as shown in **Fig. 3.4**. This issue will be discussed further in the next section.

Even with the ODC method, the total charge of the battery requires a quite long process because of the CV stage. A faster charging process should be observed for a partial charge performed until a SOC of 95% instead of 100%. In this peculiar case, the battery is mainly charged under the CC.

Another aspect that is really interesting to point out is the effectiveness of this ODC method. Two types of the efficiency are calculated; the Coulombic Efficiency (CE) and the Energy Efficiency, (EE) as defined in **Chapter 2**.

**Fig. 3.5** shows the results of Coulombic Efficiency (CE) and the Energy Efficiency, (EE) for both methods at different C-rates.

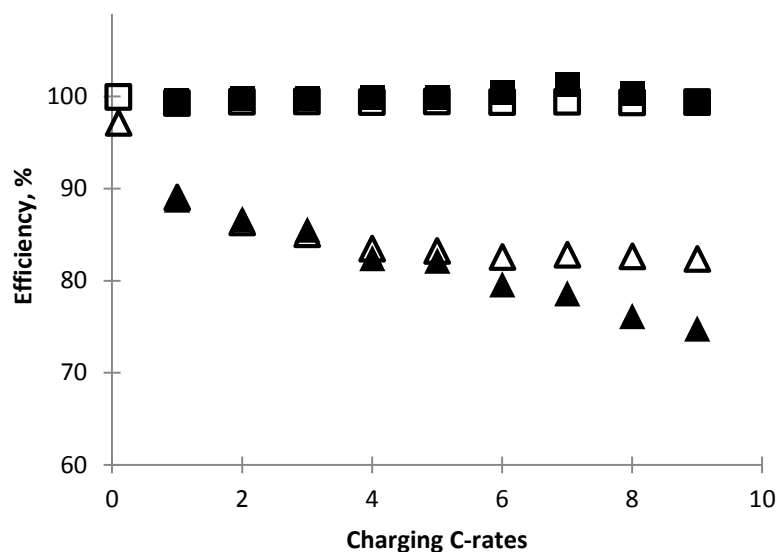


**Figure 3.5:** The coulombic and energy efficiency of both methods at various charging C-rates.  $\square$  is the CE for normal method and  $\blacksquare$  is the CE for ODC method.  $\triangle$  is the EE for normal method, and  $\blacktriangle$  is the EE for ohmic-drop compensation method.

According to **Fig. 3.5**, the CE is approximately at 100% whatever the charging C-rates and for both methods. It is a really good indication that the ODC method does not seem to affect the capacity efficiency. However, it is worth mentioning that for both methods, the EE decreases when the C-rate increases. Nevertheless, the EE reach a plateau value for the normal method for C-rates higher than 4C. Contrariwise, the higher the charging C-rates the higher is the energy loss during the charging process for the ODC method. It means that the increase of the charging C-rates leads to an augmentation of the energy losses. This latter energy loss rise manifests itself as a higher temperature increase during fast charge with ODC.

### 2.2.2 Influence of the compensation rate

The rate of compensation,  $\alpha$ , could range from 0 (normal method) to 100% (full compensation). **Fig. 3.6** shows the evolution of the overall charging time at 6C-rate for different rates of compensation. In order to improve significantly the charging time, a rate of compensation larger than 50% is required.

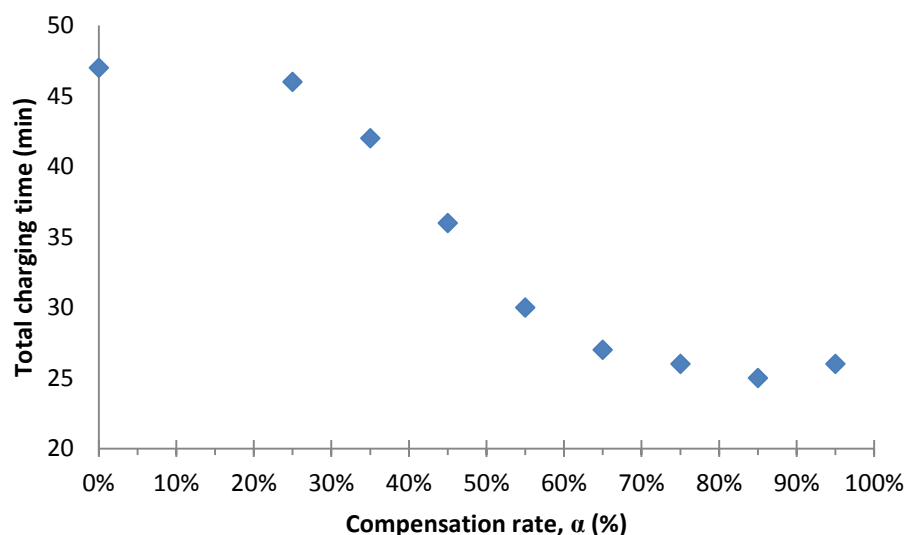


**Figure 3.6:** Total charging time at 6C-rate for different compensation rate ( $\alpha$ ).

According to **Fig. 3.6**, two levels of ODC were used in this study. Low and high level ODC correspond respectively to a compensation rate,  $\alpha$  of 57% and 93%.

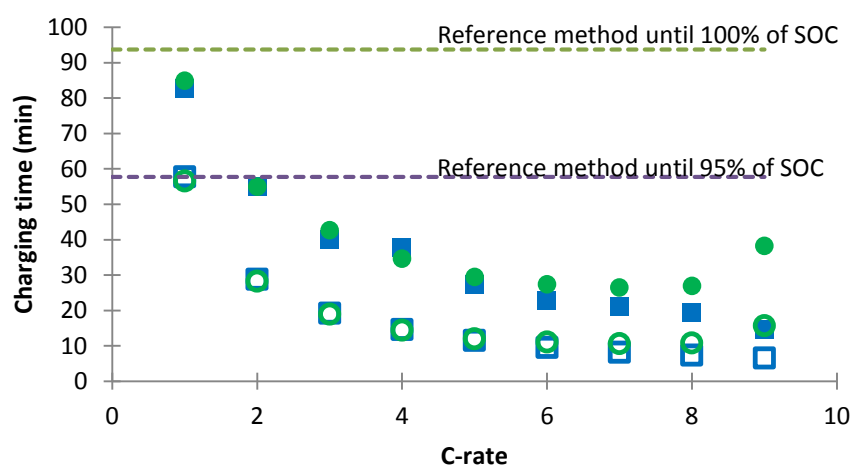


**Figure 3.7:** Charging time with ODC method: high level ODC with end-of-charge at 95% [■] and 100% [●] of SOC and low level ODC with end-of-charge at 95% [◻] and 100% [●] of SOC ( $T_a=25^\circ\text{C}$ )

**Fig. 3.7** and **Table 3.1** summarize the experimental data for those two levels of compensation. **Fig. 3.7** shows the total charging time to reach either 95% or 100% of SOC considering a high or low level of ODC. Whatever the C-rate and level of ODC, the charging time up to 95 % of SOC decreases significantly. In the both cases, the battery charge is made principally under the CC stage to reach the 95% of SOC.

**Table 3.1:** Charging time and percentage of SOC at both CC and CV stages using ODC method with high and low level compensation

High level compensation ODC							
C-rate	$V_f'$ for 93% of ODC (V)	CC stage		CV stage		Charging time (min)	$T_{max}(^{\circ}C)$
		$\Delta t$ (min)	$\Delta SOC$	$\Delta t$ (min)	$\Delta SOC$		
1	3.72	58.9	0.97	24.0	0.03	82.8	27.0
2	3.78	28.8	0.95	26.1	0.05	54.9	29.1
3	3.85	19.4	0.96	20.8	0.04	40.1	33.4
4	3.91	14.1	0.94	23.7	0.06	37.8	37.2
5	3.98	11.6	0.96	15.6	0.04	27.2	41.1
6	4.05	9.5	0.93	13.3	0.06	22.8	45.5
7	4.11	8.0	0.93	13.1	0.07	21.1	48.8
8	4.18	7.1	0.92	12.3	0.08	19.3	52.8
9	4.24	6.3	0.91	8.3	0.08	14.6	57.4
Low level compensation ODC							
C-rate	$V_f'$ for 57% of ODC (V)	CC stage		CV stage		Charging time (min)	$T_{max}$
		$\Delta t$ (min)	$\Delta SOC$	$\Delta t$ (min)	$\Delta SOC$		
1	3.70	57.6	0.97	27.3	0.03	84.9	28.1
2	3.75	28.3	0.95	26.7	0.05	55.0	31.6
3	3.79	18.7	0.94	24.0	0.06	42.6	35.6
4	3.84	13.8	0.93	20.8	0.07	34.6	39.8
5	3.89	10.7	0.90	18.8	0.10	29.5	43.6
6	3.94	8.1	0.82	19.3	0.18	27.4	46.6
7	3.99	6.3	0.74	20.2	0.26	26.5	48.2
8	4.04	4.8	0.64	22.2	0.36	26.9	47.2
9	4.09	1.3	0.19	37.0	0.81	38.3	31.6

In order to investigate the effect of the ODC level including the risk of over-compensation, two different levels are tested. **Fig. 3.7** shows the results on the charging time. It is worth pointing out that, up to 6C-rate, even with the low level ODC; the charging time until 95% of SOC is quite similar to the high level which is at about 10-11min. Moreover, the total charging time at 6C-rate for the low level ODC method is approximately the same as the high level ODC method with a difference of just 4 min. High level ODC takes about 23 min while the low level ODC takes about 27 min for a total charge.

However, for low level ODC, the charging time begins to increase from 8C-rate onwards. At 8C, the CC stage lasts for about 5 minutes compared to about 7 minutes for the high level ODC method. Even though, CC charging times are closer together, the capacities charged during that CC stage are very different. As shown in **Table 3.1**, the SOC at the end of the CC stage reaches 92% and 64% respectively for high and low level ODC. As a consequence, the remaining capacity to be charged during the CV stage is larger for low level ODC. This explains the increase in the total charging time for C-rate larger than 8C-rate using the low level ODC.

## 2.3. Temperature and thermal effect during fast charge of C/LFP Battery

### 2.3.1. Fast charge of C/LFP battery with normal method

**Fig. 3.8** depicts the surface temperature of the battery cell during fast charging at 6C-rate using normal method, with and without ventilation. For the reference charging process, a very low temperature increase is observed.

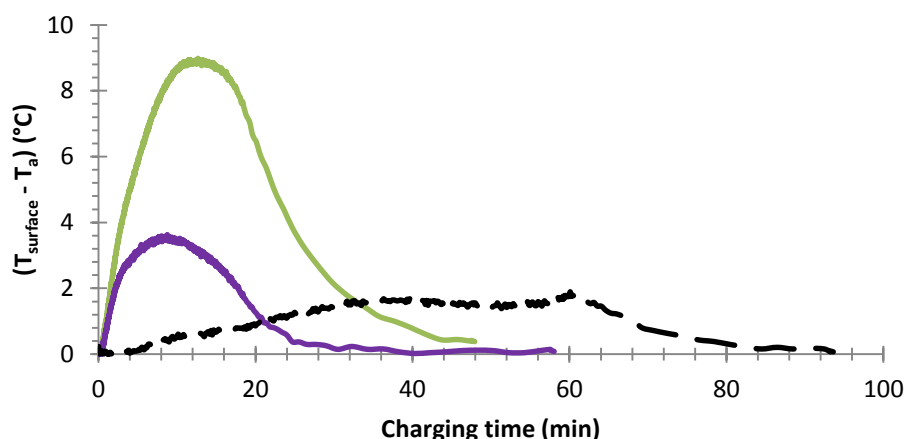


**Figure 3.8:** Surficial temperature of the battery cell versus time for 6C-rate for normal methods. — without ventilation, — with ventilation and - - Reference charging process ( $T_a=25^\circ\text{C}$ ).

For fast charge with the normal method at 6C-rate, the battery temperature first increases before dropping when the current decline at the end of the CV stage. The maximum temperature is reached during the CV stage when the current is about 3A to 4A. Without ventilation, the temperature rise until attains its maximum temperature approximately at 34°C before decreasing. The same situation is observed with ventilation but with a lower temperature increase at about 28.5°C. This highlights the efficiency of the cooling method which is able to maintain the battery temperature close to the ambient one. Indeed, the temperature increase with ventilation is quite similar to the one recorded with reference charging process.

### 2.3.2. Fast charge of C/LFP battery with ODC method

During the charging process, the battery experiences temperature increases that depend on both the C-rate and charging method (**Fig. 3.4**). **Fig. 3.9** represents the variation of temperature elevation on the outer surface of the battery cell during charging process using reference method and ODC method at 6C-rate with different level of ODC. The maximal temperature is always concomitant with the end of the CC stage whatever the charge process for the ODC method, in contrary with the normal method. This means that the battery is heated up during the CC stage because of the joule effect while it is cooled down during the CV stage. During the CV stage, as the current plunges to a lower value (see **Fig. 3.3**), the joule effect becomes negligible and the temperature drops.

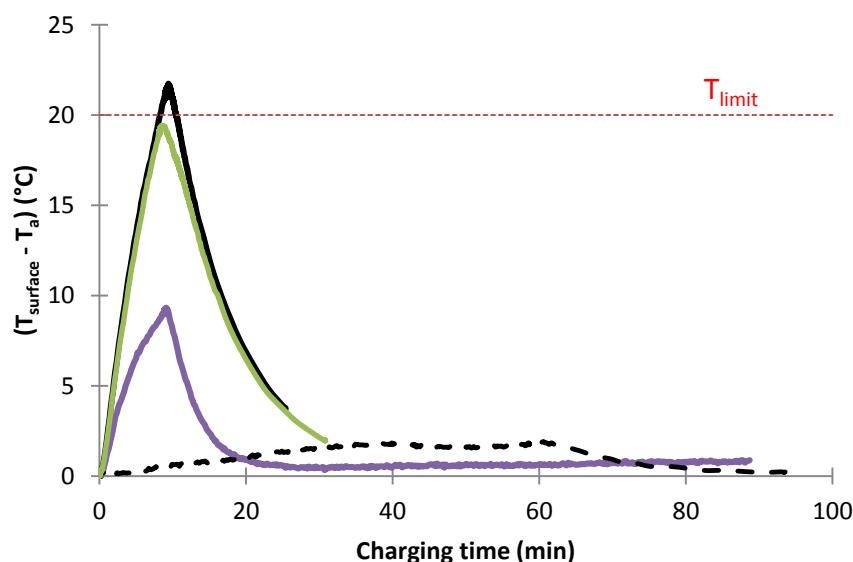


**Figure 3.9:** Surficial temperature of the battery cell versus time for 6C-rate for various methods. — High level ODC, — Low level ODC, — high level ODC with ventilation and - - Reference charging process ( $T_a=25^\circ\text{C}$ )

Unfortunately, this temperature upsurge gets worse with the ODC method. Indeed, with this method, the temperature limit defined by the manufacturer (45°C) is greatly exceeded during the fast-charging process. As shown in **Fig. 3.9**, for high level ODC, the temperature increases rapidly and reaches its maximum value of 49 °C at the end of the CC stage and exceeds the limit temperature. While for the low level ODC, the temperature is not far behind at 45°C, right at the limit. This temperature elevation during fast charge with ODC could shorten the life time of the battery by accelerating the ageing phenomena. The battery itself could be damaged. High temperature degrades the battery components and may induce thermal runaway. A sensitivity analysis of the value of compensation resistance should be performed to optimize both the charging time and battery temperature.

### 2.3.3. Ventilation system effect

A cooling system is used to overcome the temperature increase of the battery during fast charge with high level ODC. The use of a fan to provoke forced air convection to cool the battery allows a significant decrease in the outer surface temperature as shown in **Fig. 3.9**. As explained earlier, a fan imposed the forced air convection around the battery outer surface to improve heat management.

**Fig. 3.10** illustrates the maximum temperature elevation  $\Delta T_{\max}$  of the battery cell outer surface at different CC charging rates with and without ventilation. As shown, for the high level ODC method in both situations, the  $\Delta T_{\max}$  of the battery cell keeps increasing with the charging C-rate.

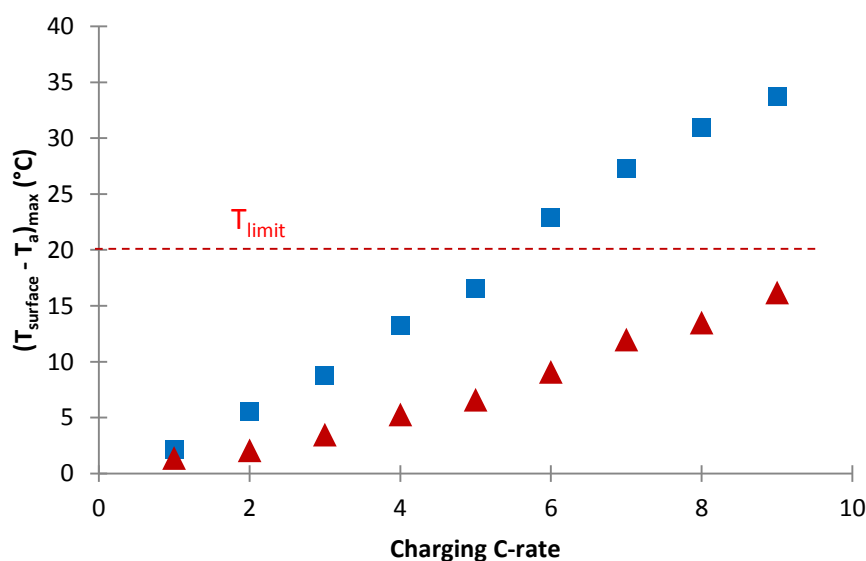


**Figure 3.10:** Comparisons of maximum difference of outer surface temperature at different charging C-rate for ODC method ■ and ODC method with ventilation system ▲. The line - - - represents the manufacturer's temperature limit of 45°C during charging. ( $T_a=25^\circ\text{C}$ )

As stated before, the temperature upsurge is quite high during charging for the high level ODC method. For example, at 9C-rate, the  $T_{\max}$  of the battery cell reaches 59°C without battery cooling. In fact, for charging C-rate higher than 6C-rate, the upper bound temperature limit during charging process is surpassed.

However, with a ventilation system, a substantial amount of heat is evacuated and the battery cools down. The  $T_{\max}$  of the battery cell only reaches 41°C at 9C-rate, which is still lower than the maximum allowed value. So, in all, fast-charge using the ODC method can be carried out to minimize the ageing process if there is a cooling system for the battery.

**Fig. 3.11a** represents the charging time with and without ventilation until 95% and 100% of SOC while **Fig. 3.11b** and **Fig. 3.11c** point out the charging time for each charging stages, CC and CV, for different charging C-rates. Even though the ventilation system is essential to cool down the battery during fast-charge, the total charging time seems to be longer.

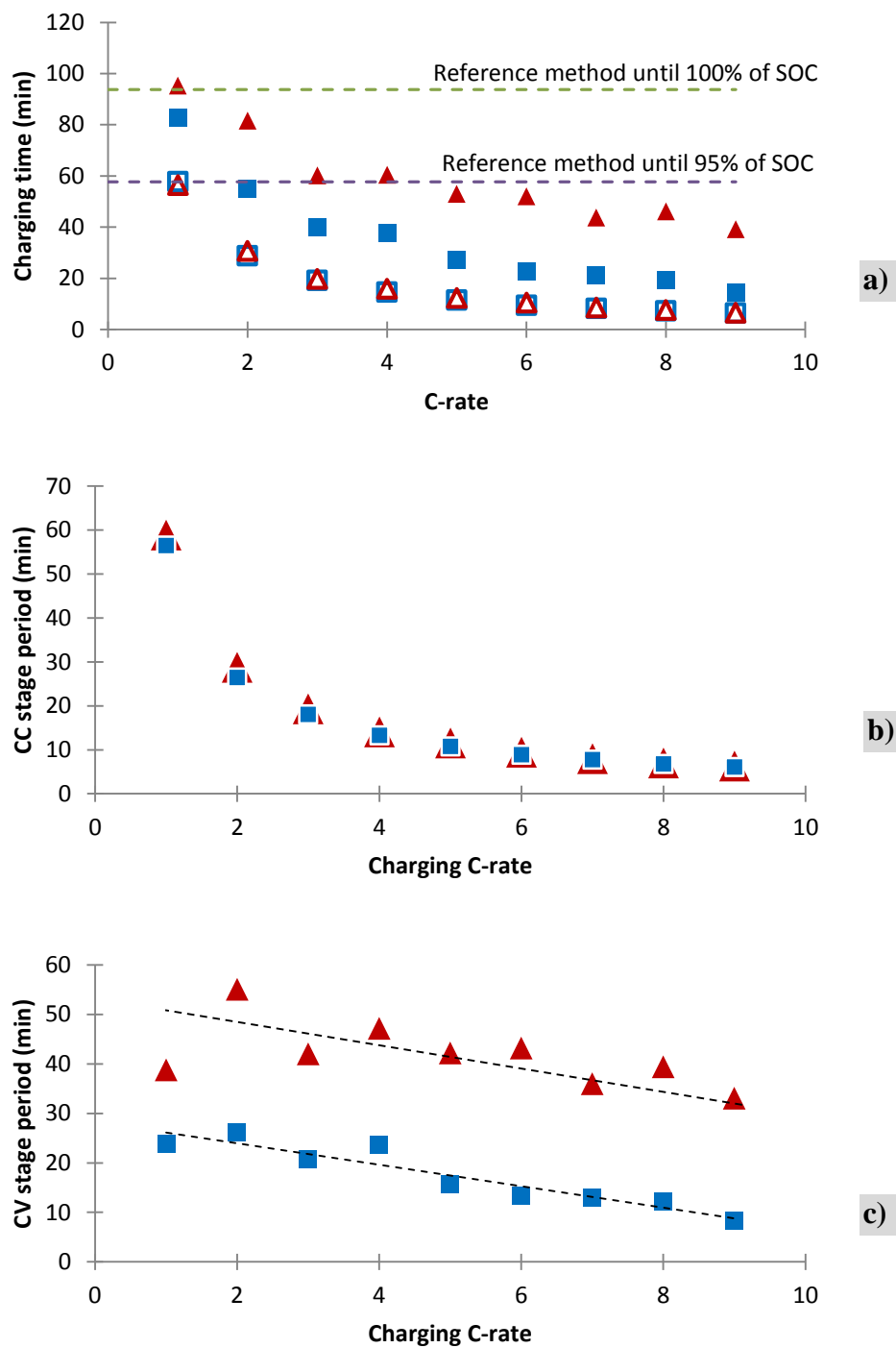


**Figure 3.11:** Charging time for different charging C-rate with ODC method until 100% of SOC ■ and 95% of SOC □. Total charging time at different charging C-rate with ODC method with ventilation until 100% of SOC ▲ and 95% of SOC △ (a) Total charging time (b) CC stages period and (c) CV stages period

As shown in **Fig. 3.11a**, the total charging time (100% of SOC) with cooling system is larger than the one without, but still faster than the reference charge until 100% of SOC. Conversely, the charging times up to 95% SOC are quite similar in the both cases.

It is worth mentioning that the charging times for both situations are close for CC stage whatever the air convection condition (**Fig. 3.11b**) while the charging times for CV stage are significantly different between those charging situations (**Fig. 3.11c**). With a ventilation system, the charging time during CV stage is much higher than the one without ventilation. This behaviour could be related to the temperature change along the CV stage (see **Fig. 3.9**). In order to confirm this behaviour, the charging processes using only the CV stage are carried out at different temperatures. Indeed, for this charging procedure, the charging time seems to be longer as the temperature decreases as shown in **Table 3.1**. The charging time at 27°C is 2 times higher than the one at 45°C (**Table** Erreur ! Source du renvoi introuvable.). It can be stated that either charge transfer or diffusion limitations can occur at lower temperatures [1]. This explains why the charging time is way too high at CV stage for a high level ODC method with ventilation system.

**Table 3.2:** Charging time with only CV stage at different temperature,  $T_a$

Chamber temperature, $T_a$ (°C)	CV charging time (min)
10	93
27	39
45	21

Nevertheless, for the ODC method, at the end of the CC stage, the battery reached approximately 90% to 95% of SOC depending on the situations. The charging time during CV stage is really low and makes the charging process slower even though there is only 10 to 5% of SOC left.

### 3. Fast charge of C/NMC battery with ODC method

During this study, other types of Li-ion batteries have also been investigated. For example, in this section the study of fast charging method is carried out for the C-NMC battery. This means that the 2 electrodes used in this battery are graphite for the negative electrode material and nickel manganese cobalt oxide (NMC) for the positive electrode materials. The nominal voltage for this

battery is about 3.6V at open-circuit. The usage range of temperature is different between charge and discharge just like the LFP batteries; at 0°C to 45°C and -20°C to 60°C respectively. The nominal capacity of these batteries is 1.5Ah. The overall characteristic of the battery that has been used could be found in **Chapter 2**.

The battery has gone through the same procedure of studies as the previous C/LFP battery for the fast charging method. The normal CCCV method and the ODC method are used and their overall protocols stay the same as before. **Fig. 3.12** represents the current and cell voltage curves during charging using normal method and ODC method at 6C-rate and 2C-rate.

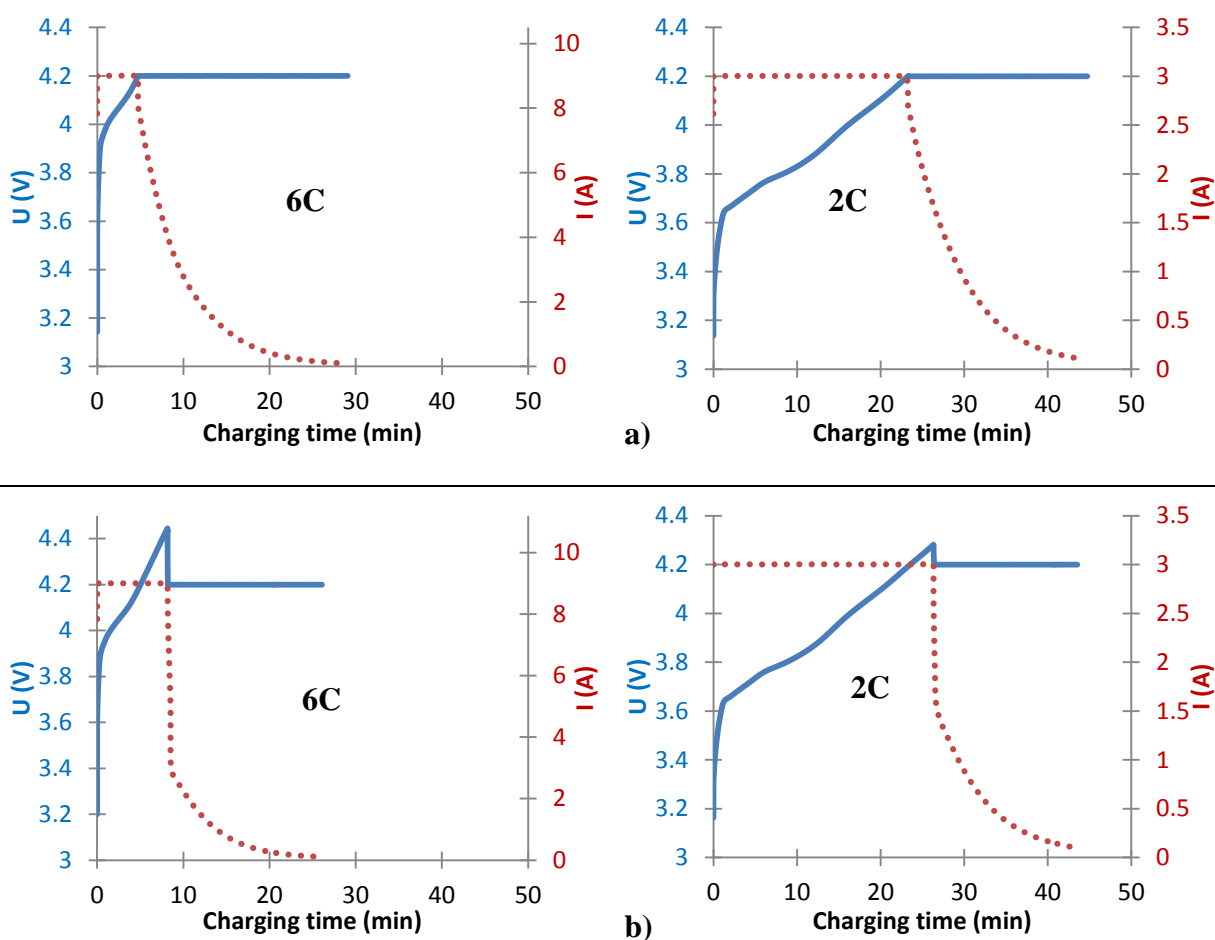


**Figure 3.12:** Current and cell voltage variation during charging process at 6C-rate (left) and 2C-rate (right) using (a) normal method and (b) high level ODC method ( $\alpha=95\%$ ).

As shown for the normal method, at 2C-rate, the voltage curve is really different compared to the one from C/LFP battery. The C/LFP battery has a more flat voltage response during 2C-rate CC-stage charging process while the one from the NMC battery has a quite linear response for normal

method. At 6C-rate with the normal method, the CC stage for NMC battery lasts about 5 min, while as discussed earlier in the above section, the CC stage lasts only 6 sec for the C/LFP battery at the same C-rate. The current drop during CV stage is also not as steep as the one from the C/LFP battery. In term of total charging time, the 6C-rate is faster than the 2C-rate as expected. Indeed, the normal charging process ends at 29 min and 45 min respectively.

When the ODC method is applied to the C/NMC battery, the charging time has not been really improved compared to the normal method. In fact, the charging times are 43.5 min and 26 min at 2C-rate and 6C-rate respectively for NMC battery using the ODC method. At high charging 6C- rate, the time gained by using the ODC method is just about 3 min compared to the normal method. For meaningful comparison, the C/LFP battery time gained was about 22 min. **Fig. 3.13** recapitulates the comparison of both charging methods in terms of charging time and temperature at different charging rates for NMC battery.

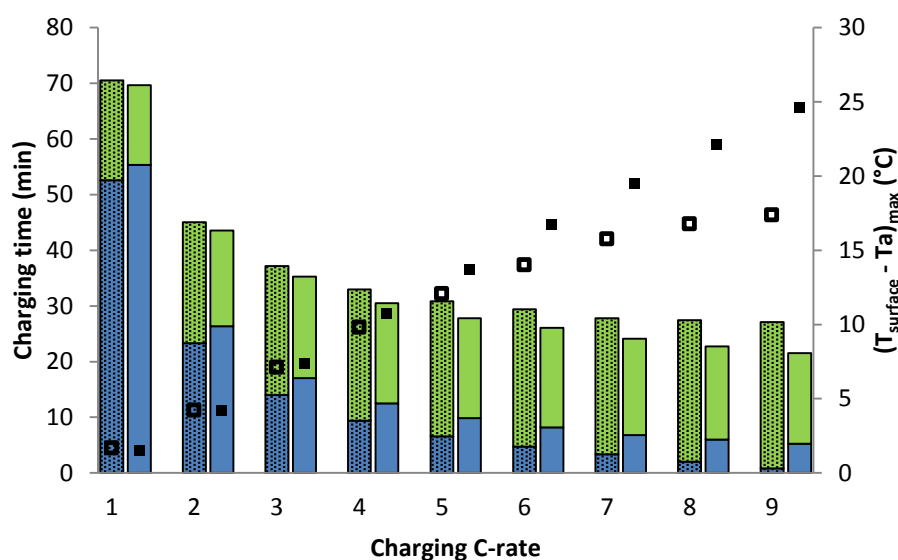


**Figure 3.13:** Charging time until 100% of SOC for normal method (left) and ODC method (right) for 1C-rate until 9C-rate for NMC battery. CC stages are in the blue color while CV stages are in the green color. □ and ■ are the maximum outer surface temperatures elevation of the cell for both methods ( $T_a=25^\circ\text{C}$ ).

As represented in **Fig. 3.13**, the ODC fast charging method has no significant impact on the charging time. The time gained of about 1 to 7 min recorded is really minimal compare to the C/LFP case. Moreover, this conclusion is also true whatever the level of compensation. It is worth mentioning that similar thermal behavior is observed as for C/LFP battery. So, **Fig. 3.14** shows the total charging time for ODC method at 6C-rate for NMC battery at different compensation rate. The compensation

rate has no significant effect on the charging time. The time gained is just about 3 min between 25% and 95% of compensation for example.

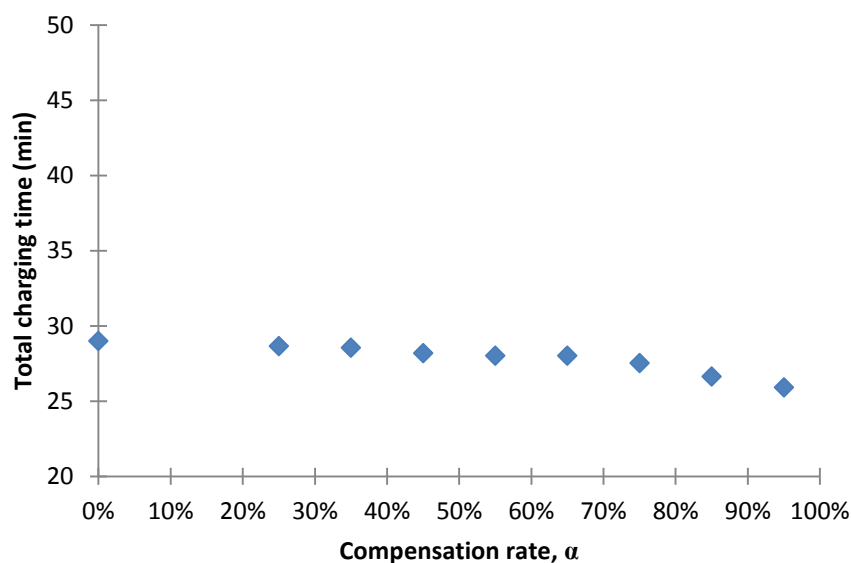


**Figure 3.14:** Total charging time at 6C-rate for different compensation rate ( $\alpha$ ) for NMC.

As a partial conclusion, the fast charge with ODC method cannot be applied for the NMC battery. This latter phenomenon can be related to the shape of the battery cell voltage curve. The ODC method may be only applied to batteries that have similar flat cell voltage profile as C/LFP battery.

#### 4. Fast charge of LTO/LFP battery with ODC method

The fast charging method has also been performed onto the LTO/LFP battery. This time around the difference between this battery and the C/LFP battery cell lies with the negative electrode materials. Indeed as explained in **Chapter 1**, this battery uses lithium-titanate-oxide (LTO) as the negative electrode. The details characteristics of this battery have been presented in **Chapter 2** and the interesting part of this battery cell is that it is mentioned by the manufacturer as capable to undergo the normal fast charging procedure until 10C-rate.

As for all the batteries investigated in this study, this LTO/LFP battery cells has gone through the same procedure of study as the previous C/LFP and C/NMC batteries for the fast charging methods. The normal CCCV method and the ODC method are used. **Fig. 3.15** represents the overall results of fast charging procedures of both methods; normal method and ODC method (low and high level)

regarding the total charging time and maximum temperature at different charging rates for LTO/LFP battery.

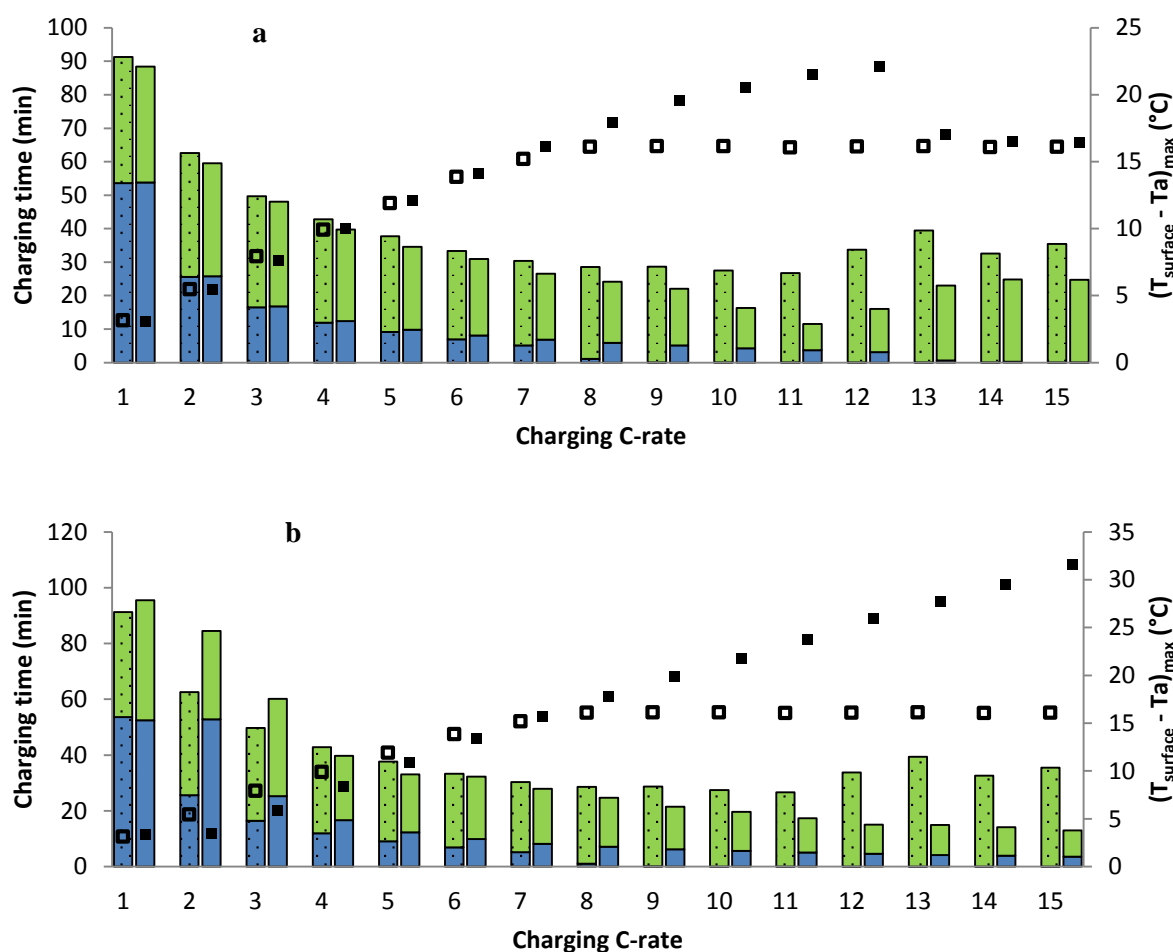


**Figure 3.15:** Charging time until 100% of SOC for normal method (left) as well as (a) low ( $\alpha=50\%$ ) and (b) high ( $\alpha=93\%$ ) level ODC method (right) for C-rate ranging from 1C until 15C for LTO/LFP battery. CC stages are in the blue color while CV stages are in the green color. □ and ■ are the maximum outer surface temperatures elevation of the cell for both methods ( $T_a=25^\circ\text{C}$ ).

Using this ODC method, the battery can endure the fast charging procedure up until 15C-rate as shown in **Fig. 3.15b**, even at high level ODC. At low level ODC method, the charging time seem to exhibit a minimal value of 12 min at 11C-rate as shown in **Fig. 3.15a**. This means that low level ODC reach its optimal value at 11C-rate. For higher C-rate, the LTO/LFP is charged principally during the CV stage as the CC stage is inexistent. At high level, the total charging time steadily decreases when the C-rate increases. At 15C-rate, the battery is charged the fastest at about 13 min with the maximum surficial temperature of  $56.6^\circ\text{C}$ . At the same C-rate using the normal fast charging method, the battery takes about 35 min to be fully charged. The total charging time gain is about 62% if the high level ODC method is used at 15C-rate. The total charging time gain at 10C-rate is only

33% but the maximum temperature remains really close to the one recommend by the manufacturer which is about 45°C.

As shown, this type of battery can really withstand fast charging procedure far more in term of charging C-rates if compared to the two other batteries beforehand. Remarkably, LTO/LFP battery can endure the normal fast charging method up until 8C-rate before it reaches its limit (where at higher C-rates, the battery is charged principally and only at CV stage, CC stage is skipped altogether). Fast charges with ODC method decrease the total charging time up until 15C for the high compensation rate. The latter reaches value lower than 20 min for C-rate larger than 10C. At the same time, the temperature of the battery exhibits high temperature increase induced by the joule effect. Indeed, the surface temperature exceeds 45°C for C-rates higher than 10C. The ODC method seems to be applicable for LTO/LFP battery with higher C-rate as reported by the manufacturer which is not the case when normal method is applied.

As like the other batteries, the study of the influence of compensation rate has been performed for the LTO/LFP battery. **Fig. 3.16** shows the impact of the compensation rate on the total charging time at 6C and 11C.

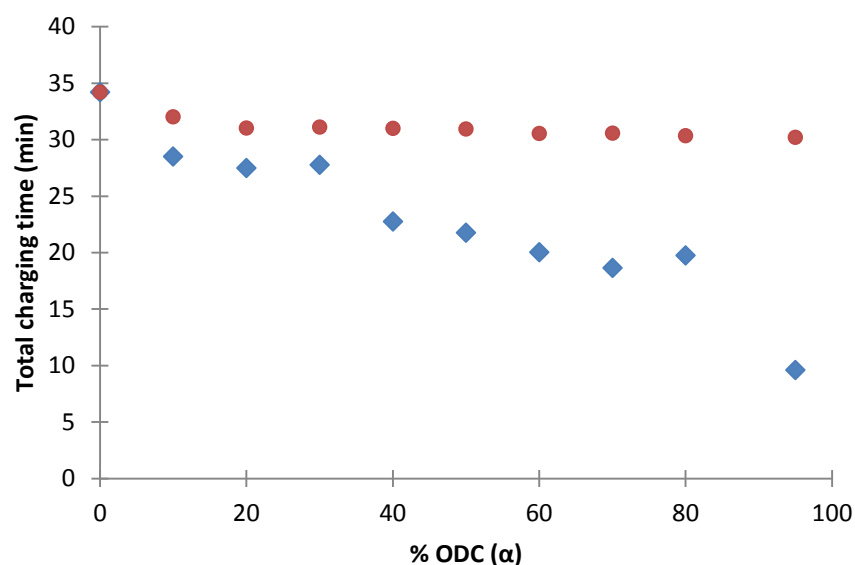


**Figure 3.16:** Total charging time for different compensation rate ( $\alpha$ ) for LTO/LFP battery at 6C-rate ● and 11C-rate ◆.

As expected, the compensation rate does not have any impact at 6C. There is no significant improvement of charging time. In contrary, the total charging time seems to decrease quite linearly when the compensation rate rises at 11C-rate. So, the higher the compensation rate, the lower the

total charging time is. Indeed, the fast charge at 11-C ODC with  $\alpha=95\%$  (high level) allows saving 25 min at least by comparison to the normal method ( $\alpha=0\%$ ).

These latter results show that in order to have a significant effect of the fast charge with ODC on LTO/LFP battery, investigations must be made using a high C-rate as well as high compensation rate. In our particular case of LTO/LFP battery, the C-rate should be higher than 8C with a high compensation rate. These conditions of operation are rather different to the ones obtained with C/LFP battery. Indeed, for the C/LFP, the effect of ODC method starts to be noticeable from 5C-rate onwards. So, 6C-rate can be used for the compensation rate investigation for C/LFP battery as shown in **Fig. 3.6** earlier

Finally, **Figure 3.17** shows the percentage of capacity charged during the CC stage at different C-rate and for the normal and high level ODC methods.

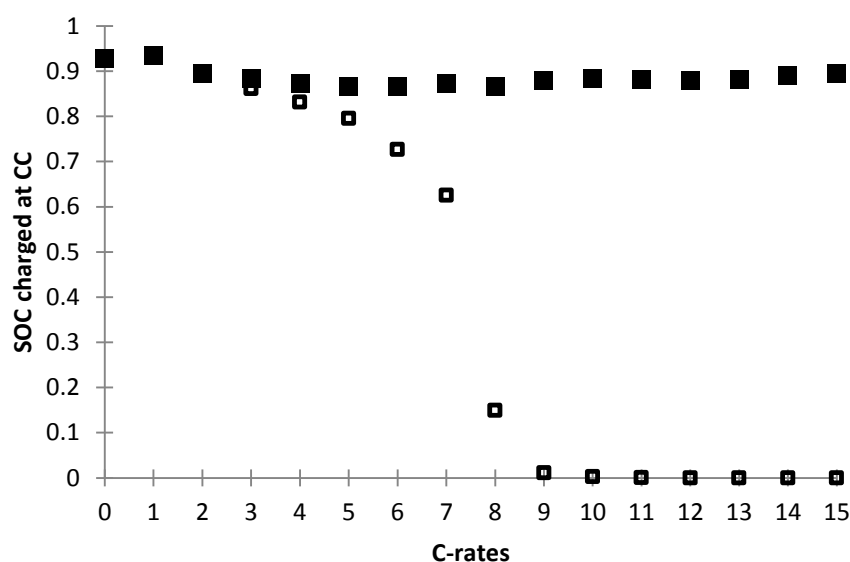


**Figure 3.17:** SOC charged during CC stage at different charging C-rates for normal method  $\square$  and high level ODC method  $\blacksquare$ .

As shown, at low C-rates, the battery is mainly charged during the CC stage. However, for normal method, the CC stage seems to be skipped totally as the charging C-rates reach 7C-rate. This means that when normal method is used, the LTO/LFP battery is charged totally at CV stage from 8C-rate onwards. Conversely, for high level ODC method, the battery is charge principally at CC stage whatever the C-rate. As depicted by **Fig. 3.17**, the battery is charge almost 90% of total SOC during the CC stage up until 15C-rate. However, considering the high temperature elevation, fast charge

with high level ODC for C-rate higher than 10C-rate could damage the battery and also cause a high security concern. This latter's results is consistent with the manufacturer information in term of the maximum temperature allowed.

## 5. Comparison of the three batteries

**Fig. 3.18** and **Fig. 3.19** present the curves of battery voltage as a function of SOC during the CC stage for all the three types of battery using both the normal charging method and the ODC method.

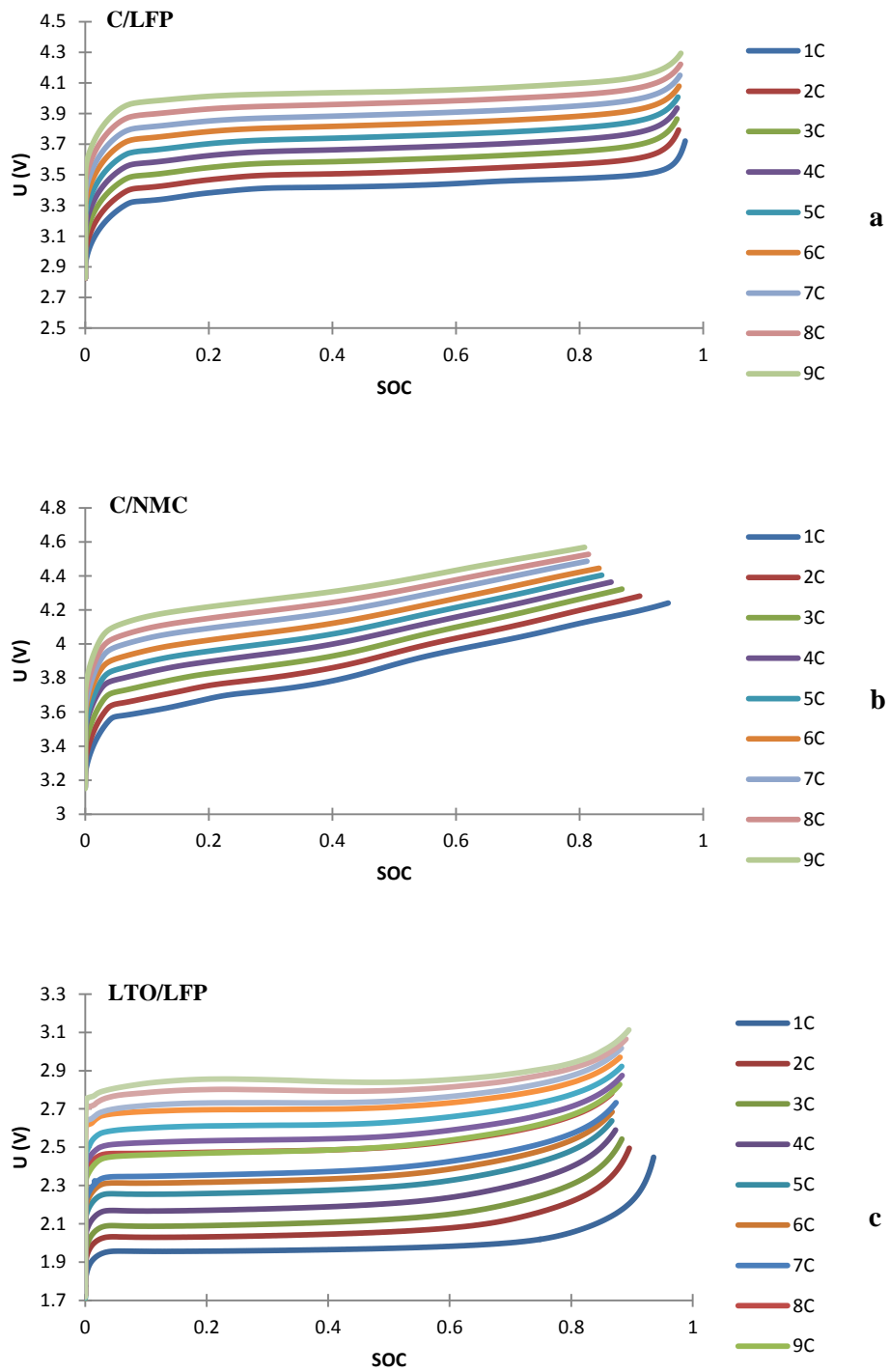


**Figure 3.18:** Battery voltage as function of SOC during CC stage for C/LFP, C/NMC and LTO/LFP batteries at different C-rates using ODC method (high level).

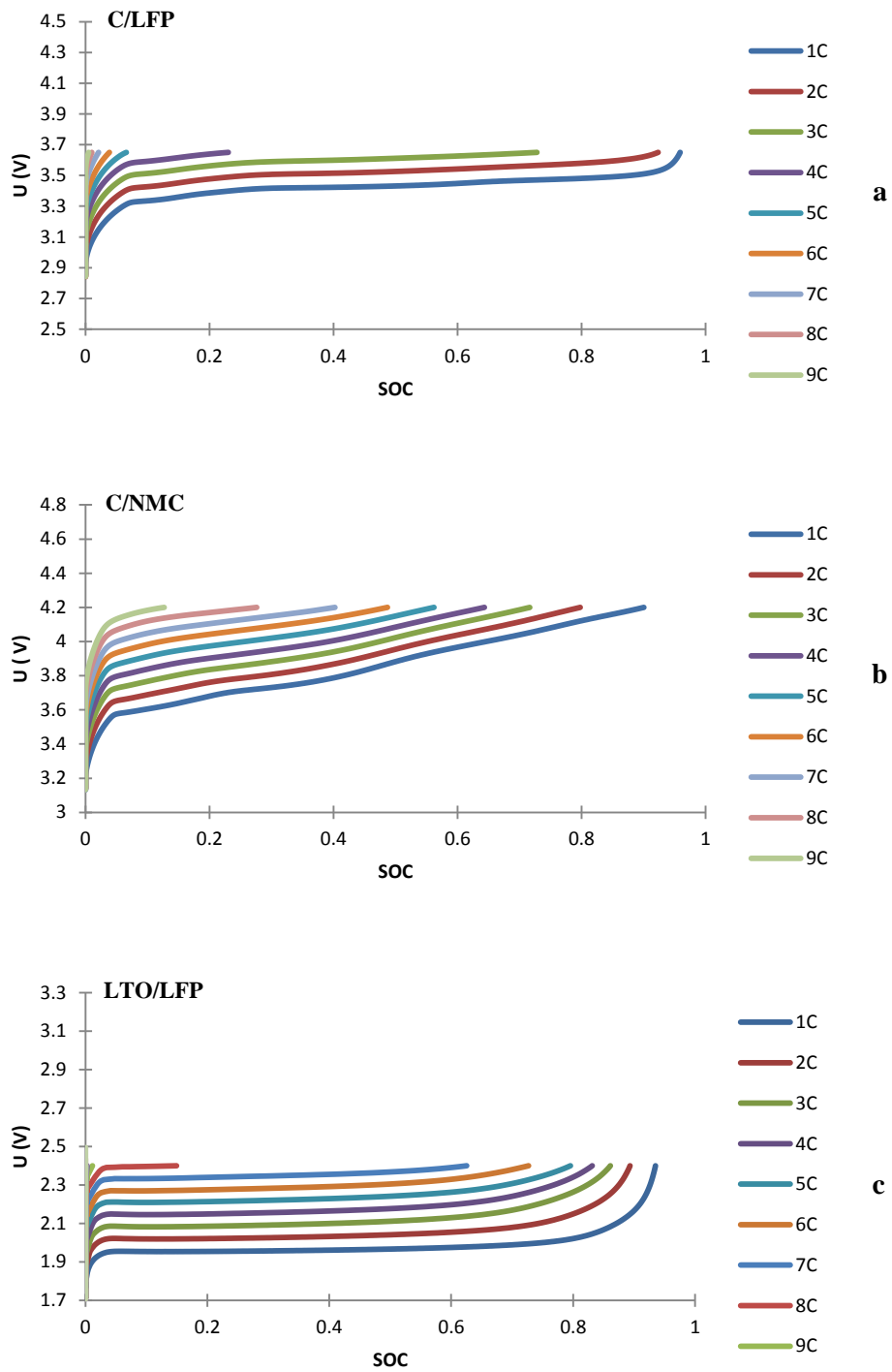


**Figure 3.19:** Battery voltage as function of SOC during CC stage for C/LFP, C/NMC and LTO/LFP batteries at different C-rates using normal method.

The curves from the C/NMC battery present more obvious differences from the other two batteries. The C/NMC voltage curves seem to have linear response for both methods. As stated earlier in the section above, there is no difference between both of the charging method and the ODC method does not really improves the charging process for this type of battery, at least in term of total charging time. But, it is interesting to point out that when using the ODC method, the C/NMC battery manage to reach at almost 80% of SOC at the end of CC stage constantly, for all the charging C-rates applied. So, this result is also quite an accomplishment considering this effect might be needed for some other applications for this type of battery using the ODC method.

On the other hand, the C/LFP and LTO/LFP batteries have quite similar voltage curves. It is worth to mention that C/LFP battery reaches approximately at the same SOC at the end of CC stage of ODC method while it is not really the case for LTO/LFP. Indeed, the LTO/LFP battery reaches more percentage of SOC during low C-rates approximately until 4C-rate before reaching up at a constant value of SOC at 86%. Moreover, if inspected closely, the curves response of the ODC method for C/LFP battery have steeper response towards the end of the CC stage. Meanwhile, the ones from LTO/LFP battery increase a little bit slowly at the end of the CC stage. This particular characteristic is most probably the reason where both of these batteries differ and it makes that the C/LFP battery is more consistent in term of SOC charged during CC stage compared to the LTO/LFP battery when using the ODC method.

When the normal method is used as fast charging method, the LTO/LFP battery proves to be the better option as it is able to hold longer during CC stage. Indeed, it manages to fill up the SOC between 73% and 93% only at CC stage when operating between 1C-rate and 6C-rate respectively. This is quite an achievement when comparing to the other two batteries which are not suitable at all for fast charging purposes using the normal method. However, LTO/LFP battery still cannot handle higher C-rate without using the ODC method as proved earlier.

## 6. Conclusions

Experiments were performed on 3 types of batteries to study the ohmic-drop compensation (ODC) for fast charging process. The ODC method was compared with the normal method for different C-rates at especially during the CC stage. The total charging time continues to decrease when the charging rate increases while it reaches a plateau for the normal method for all the batteries used.

The thermal behaviour for both charging methods is also studied for C/LFP battery. It turns out that the thermal behaviour was in accordance with both the C-rate and the duration of the CC stage. Indeed, the outer surface temperature of the battery continues to rise as the C-rate increases for the ODC method and exceeds the manufacture's temperature limit while the temperature stagnates for normal method when it reached its limit at 4C-rate. This temperature issue could be minimized either by low level ODC method or/and with forced air cooling. However, the CV stage of the latter method could prolong the charging process, thus results in a longer charging time.

Charging the battery cell with ODC method until 90% or 95% of SOC, coupled with forced air cooling is also a solution that could be considered. Even so, with this charging criterion, the battery needs to be slightly oversized for it to be reliable to deliver the necessary energy and capacity.

The ODC method has also been studied for C/NMC battery and LTO/LFP battery. The total charging time can be improved significantly when using the ODC method in the case of LTO/LFP batteries. The C/LFP battery is really consistent when using the ODC method while the LTO/LFP battery can go up further in term of C-rate compared to C/LFP. However, the ODC method has very little effect and improvement for C/NMC battery in term of total charging time compared to the normal method because this battery has linear voltage response during charging. It seems that the ODC method only suits for the battery that has a flat cell voltage such as the LFP batteries.

## 7. Reference

[1] X.H. Rui, Y. Jin, X.Y. Feng, L.C. Zhang, C.H. Chen, A comparative study on the low-temperature performance of  $\text{LiFePO}_4/\text{C}$  and  $\text{Li}_3\text{V}_2(\text{PO}_4)_3/\text{C}$  cathodes for lithium-ion batteries, *Journal of Power Sources*, 196(4) (2011), pp. 2109-2114.



# **Chapter 4: C/LFP Li-ion battery thermal modelling**

---



## 1. Introduction

In **Chapter 3**, the influence of the ODC method [1] has been assessed regarding the charging time and temperature increase. During fast charge, the Li-ion battery experiences an increase of temperature because of the reversible and irreversible heat sources. In the case of fast charge, the temperature could be significant and local temperature could exceed the maximal temperature of the battery leading to degradations. The integration of the Li-ion batteries in power systems requires the availability of dynamic models predicting the battery temperature under different operation profiles and thus fast charge

Modeling heat production and transport in a battery is a multi-physics problem. From a general point of view, the temperature distribution inside the cell is governed not only by the local heat source rate in the exothermic reaction zones and current density distribution, but also by the local heat removal rate, controlled by heat transfer rate with ambient air.

Most of the battery models consider a complex electrochemical approach [2]. Some of them are coupled with a thermal model to simulate the temperature profile of a battery under different operating conditions, geometries or cooling rate [3,4]. These models rebuild the full physicochemical processes including spatial resolution by means of a set of partial differential equations. Although, physicochemical models can accurately describe the voltage-response of the battery, they require a detailed understanding of the complex physical and chemical processes in the case of commercial batteries [5]. In addition, they need a massive computational power and, which is even more important, a high parameterization effort [6]. To reduce calculation effort, a homogeneous current distribution over the electrodes surface is often assumed [7, 8, 9] or/and the set of partial differential equations can be restricted to one spatial dimension [10], which leads to an inferior simulation precision.

This third chapter presents a simplified thermal model of our C-LFP cylinder cell. This approach is similar to the one proposed by *Forgez et al.* [11] and *Shadman Rad et al.* [12] but it was implemented in our case to investigate the temperature change of the battery during fast charges which highlight significant temperatures increase during the CC stage [1]. As the development of the electrochemical model is a very complex task, the experimental current and cell voltage recorded during the charge are used as input data. **Table 4.1** represents some of the literatures in which the thermal model simulation is carried out on different types of Li-ion battery using different approaches.

**Table 4.1:** Thermal model simulation

Author	Battery characteristics		Simulation type	Remarks
D. H. Jeon et. al.[13]	Sony-US18650, 1.5Ah, LiCoO <sub>2</sub> /C	Cylindrical	3D-axi- symetry	
M. Shadman Rad et. Al [12]	A123- ANR26650M1, 2.3Ah, LIFePO <sub>4</sub> /C	Cylindrical	2D-model	Lumped element model
C. Fogez et. al. [11]	26650-cell, LIFePO <sub>4</sub> /C	Cylindrical	1D-model	T-type thermocouple is inserted into the battery for measuring internal temperature
S. Al Hllaj et. al. [4]	Sony-US18650, 1.8Ah, LiCoO <sub>2</sub> /C	Cylindrical	1D-model	
Y. Inui et. al. [14]	Sony-US18650G3, 1.8Ah, LiCoO <sub>2</sub> /C	Cylindrical	2D and 3D- model	Prismatic type of battery cell is also simulated
E. Prada et. al. [5]	A123- ANR26650M1, 2.3Ah, LIFePO <sub>4</sub> /C	Cylindrical	1D-model	Electrochemical and thermal model
Y. Lai et. al. [15]	10Ah, LIFePO <sub>4</sub> /C	Prismatic /pouch	2D and 3D- model	Electrochemical and thermal model
K. Yeow et. al. [16]	A123- ANR26650M1, 2.3Ah, LIFePO <sub>4</sub> /C	Cylindrical and pouch	3D-model	

In this chapter, the simulation studies were carried out to predict the temperature change inside and on the outer surface of the battery cell during fast charge with ODC method at different C-rates. The input parameters of the thermal model (heat transfer coefficients and heat capacity) are determined from transient experiments (see **Chapter 2**). As the inner temperature of the battery strongly depends on the heat conductivity coefficient, a sensitivity analysis of this latter parameter is performed. Finally, the influence of the ambient temperature as well as air cooling is investigated

## 2. C/LFP Li-ion battery thermal model description

### 2.1 Battery Description

**Fig. 4.1** shows the structure of the C-LiFePO<sub>4</sub> cylinder cells manufactured by PHET (model: IFR13N0-PE1150) used in this study (see **Chapter 2**). Among the three classical battery cell geometries (i.e. cylindrical, prismatic and pouch cell), the cylindrical one is easier to manufacture and has a good mechanical stability. A cross-section along either the radius or the height of the battery is shown in **Fig. 4.1**. A jelly-roll is embedded within the cylindrical can and consists in repeating units of five layers: (1) negative current collector (copper), (2) negative electrode, (3) separator, (4) positive electrode and (5) positive current collector (aluminum) whose dimensions are about 240  $\mu\text{m}$ . The electrodes and the separator are porous media flooded with electrolyte where ionic transport takes place through their thicknesses. In contrast, the electronic charge transport in the cell occurs along the entire current-collector surfaces whose dimensions are several orders of magnitude greater than that of the battery-layer thickness. This multilayers structure is a multifunctional component where electrochemical reactions and current collection take place as well as heat generation and ensures the mechanical stability. The other components are not considered due to minor effect on the thermal analysis of small-size cylindrical battery.

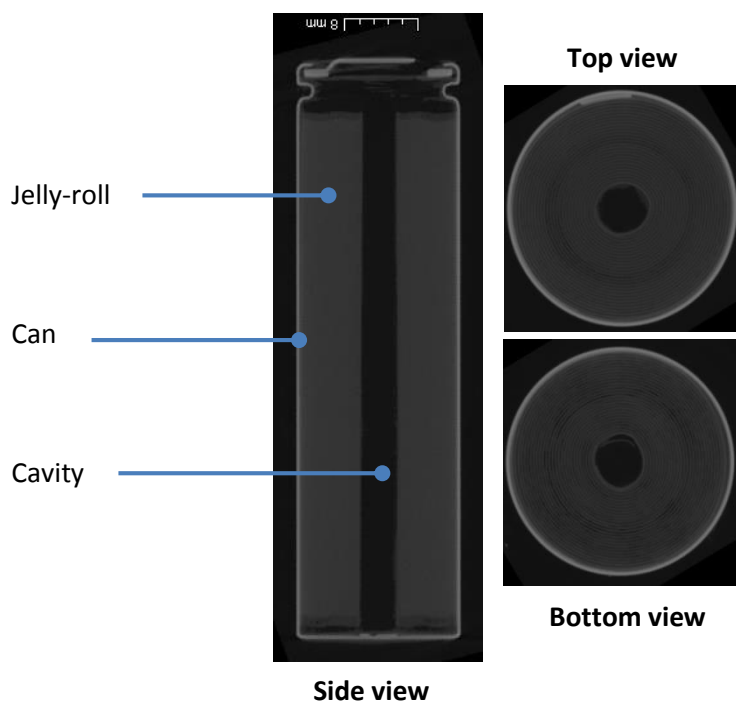


**Figure 4.1:** Jelly-roll architecture inside the battery: Side, top and bottom view.

All of the main battery parameters (geometry, capacity, mass, etc.) are summarized in **Table 4.2**. More information about this C/LFP battery can be found in **Chapter 2**. The battery consists of several components: organic electrolyte, dissolved lithium salts, polymer separator, current collectors, graphite and composite electrodes, supporting materials, metal casing, etc. So it is difficult to estimate the overall physical properties of the cell based on the physical properties of its constituents. So, experiments were performed in order to estimate the average value of the specific heat capacity ( $C_p$ ) of our Li-ion battery (see **Chapter 2**). Thanks to the Jelly-roll architecture of the battery, the average value for the thermal conductivity could be estimated. It will be discuss further in the next section below.

**Table 4.2. Battery cell specifications.**

Parameter	Value or description
Diameter, d [mm]	18.1
Height, h [mm]	65
Mass, m [g]	41
Nominal capacity, [mA.h]	1100

## 2.2 Development of the thermal model

Energy balance calculations are required for the design and thermal management of battery systems. A proper cell energy balance will give reliable predictions of thermal characteristics such as heat generation and temperature-time profiles. In this section, a general energy-balance equation for battery systems based on the approach proposed by *Bernardi et al.* [17] is presented. On the whole, the general energy balance for a battery system will be derived from the first law of thermodynamics. Whatever the battery shape and assuming a non-uniform temperature distribution, the energy balance equation can be written as:

$$\rho C_p \frac{d}{dt}(T) = -\text{div}(-\lambda \text{grad}(T)) + \dot{Q}_{in} \quad (4.1)$$

Where  $T$  is the temperature inside the cell,  $\rho$  the density of cell,  $C_p$  the specific heat capacity of the cell,  $\lambda$  the heat conduction coefficient and  $\dot{Q}_{in}(t)$  the local heat sources in the battery, which are distributed depending on heat generation mechanisms. The external surface is subjected to a natural convection toward ambient temperature (boundary condition):

$$\varphi = h(T - T_a) \quad (4.2)$$

Where  $h$  is the heat transfer coefficient and  $T_a$  the ambient temperature. In this study, the convective heat transfer coefficient was not considered as temperature dependent; its value remains constant. As for the battery surface, only the lateral surface was taken into account because both of the extremities of the battery cell were obscured from the environment by the clamp that held the battery (**Chapter 2, Fig. 2.1b**). At initial state, the cell temperature is equal to ambient temperature. Considering the differential energy balance (**Eq. 4.1**), the heat production is governed by different generation mechanisms: such as the reversible heat (or entropy) and internal losses (i.e. ohmic and overpotential) for lithium battery [18]. This latter parameter is a key issue for the development of thermal model of a Li-ion battery. To develop a mathematical model that describes the thermal behavior of the battery, the cell can be considered as a thermally homogenous body with effective thermophysical properties.

### 2.2.1 Heat sources in Li-ion battery during charge

The calculation of local heat sources in the cell is obtained from the total reaction's enthalpy ( $\Delta_r H$ ) in the battery. From a thermodynamic point of view, total reaction's enthalpy ( $\Delta_r H$ ) is given as the sum between the free Gibbs energy ( $\Delta_r G$ ) and the entropy ( $\Delta_r S$ ):

$$\Delta_r H = \Delta_r G + T\Delta_r S \quad (4.3)$$

$$\dot{Q}_{in} = I \left( \frac{\Delta_r H}{nF} + U \right) = I \left( \frac{\Delta_r G + T\Delta_r S}{nF} + U \right) = I \left[ (U - U_{OCV}) + \frac{T\Delta_r S}{nF} \right] \quad (4.4)$$

$U_{OCV}$  being the Open Circuit Voltage that depends on the State of Charge of the battery and equal to  $-\frac{\Delta_r G}{nF}$ . The difference between  $U$  and  $U_{OCV}$  is the cell overpotential which is an indicative of irreversibility such as ohmic losses ( $\eta^{ohm}$ ), charge-transfer overpotentials and mass transport limitations ( $\eta^+ + \eta^-$ ). The overpotential multiplied by the current is termed the polarization heat and is composed of the joule heating within the battery, as well as the energy dissipated in electrode overpotentials.

From **Eq. 4.4**, the heat production in the battery is the sum of reversible heating due to the entropy change:

$$\dot{Q}_S = I \frac{T\Delta_r S}{nF} \quad (4.5)$$

and the heat generated from resistive dissipation,  $\dot{Q}_R$  (i.e. irreversible loss):

$$\dot{Q}_R = I (U - U_{OCV}) \quad (4.6)$$

The latter is an exothermic dissipative heat ( $\dot{Q}_R > 0$ ) that heats the cell for both charge and discharge.

## 2.3 Determination of the model parameters

Since, two sources of heat generation have to be considered in the analysis of battery temperature increase during fast-charge, the chemical reaction of the cell called the “reversible” heat, as well as the heat effects of ohmic resistance and polarization called “irreversible” are estimated from experimental measurements depending on SOC and current to be implemented in the simulation.

### 2.3.1. Reversible heat source

Regarding the **Eq. 4.5**, the entropy change  $\Delta_r S(T)$  can be calculated by estimating the open circuit voltage change with temperature according to *Shadman Rad et al.* [12]:

$$\Delta_r S(T) = nF \left( \frac{\partial U_{OCV}}{\partial T} \right)_{\xi, P} \quad (4.7)$$

Where  $\xi$  represents, in general terms, the reaction progression. In our specific case, it is the SOC of the cell.

The open circuit voltage measurements were carried out at different temperature and SOC to determine the entropy change based on the method proposed by *Forgez et al.* [11]. The battery cell was put through various temperatures inside a climatic chamber ranging from 15° to 35°C at different SOCs. The cell was charged using a C/20 current at 25°C and the battery was subsequently allowed to relax for 3h at the same temperature, after which the thermal cycle (15°C, 3h; 28°C, 3h; 35°C, 3h; 25°C, 3h) was applied. **Fig. 4.2** depicts an example of that measurement at 20% of SOC

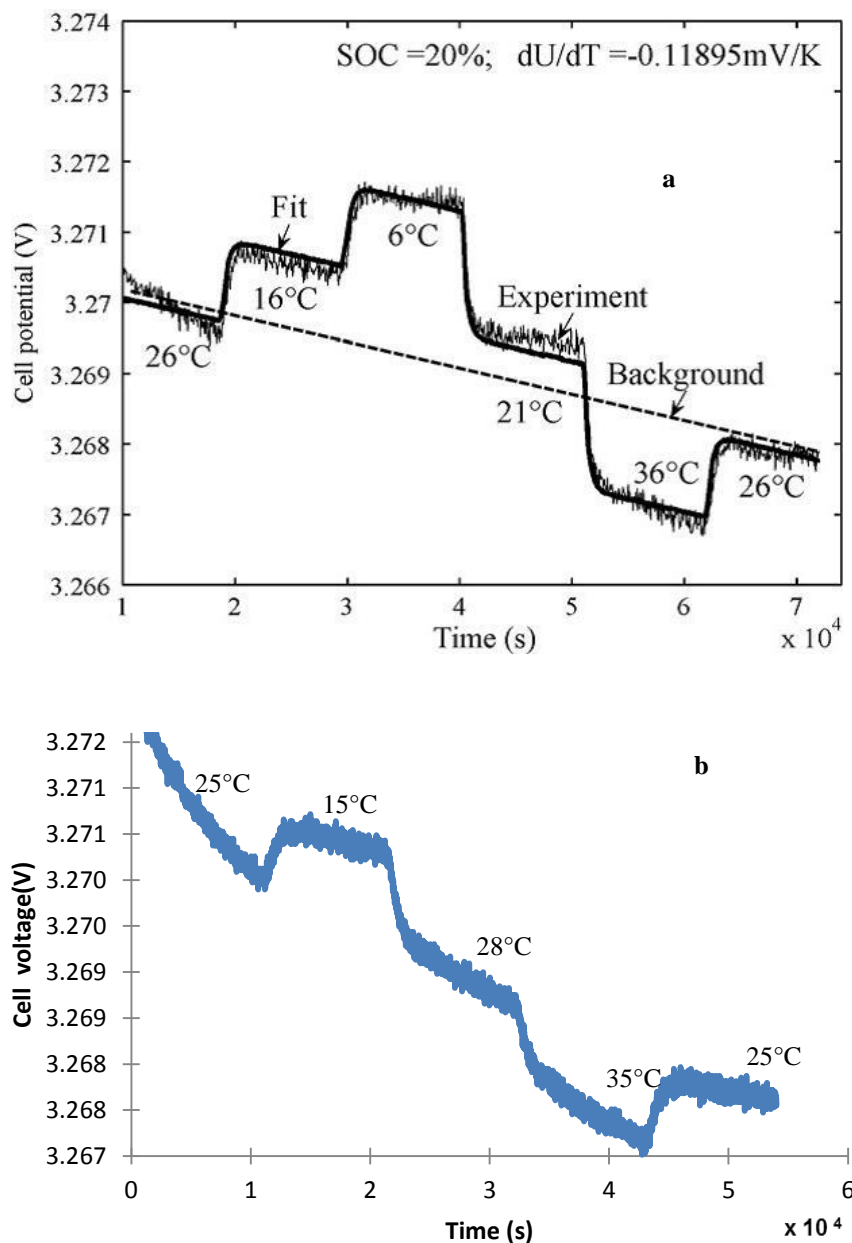


**Figure 4.2:** Example of the voltage variation during thermal cycle of 20% SOC for (a) *C. Forgez et al.* [11] and (b) C/LFP by PHET

The entropy changes ( $\Delta_r S$ ) obtained as a function of SOC is displayed in **Fig. 4.3**. The values obtained for entropy changes are in consistency with both previously reported values for LFP battery by *Forgez et al.* [11] and *Shadman Rad et al.* [12].

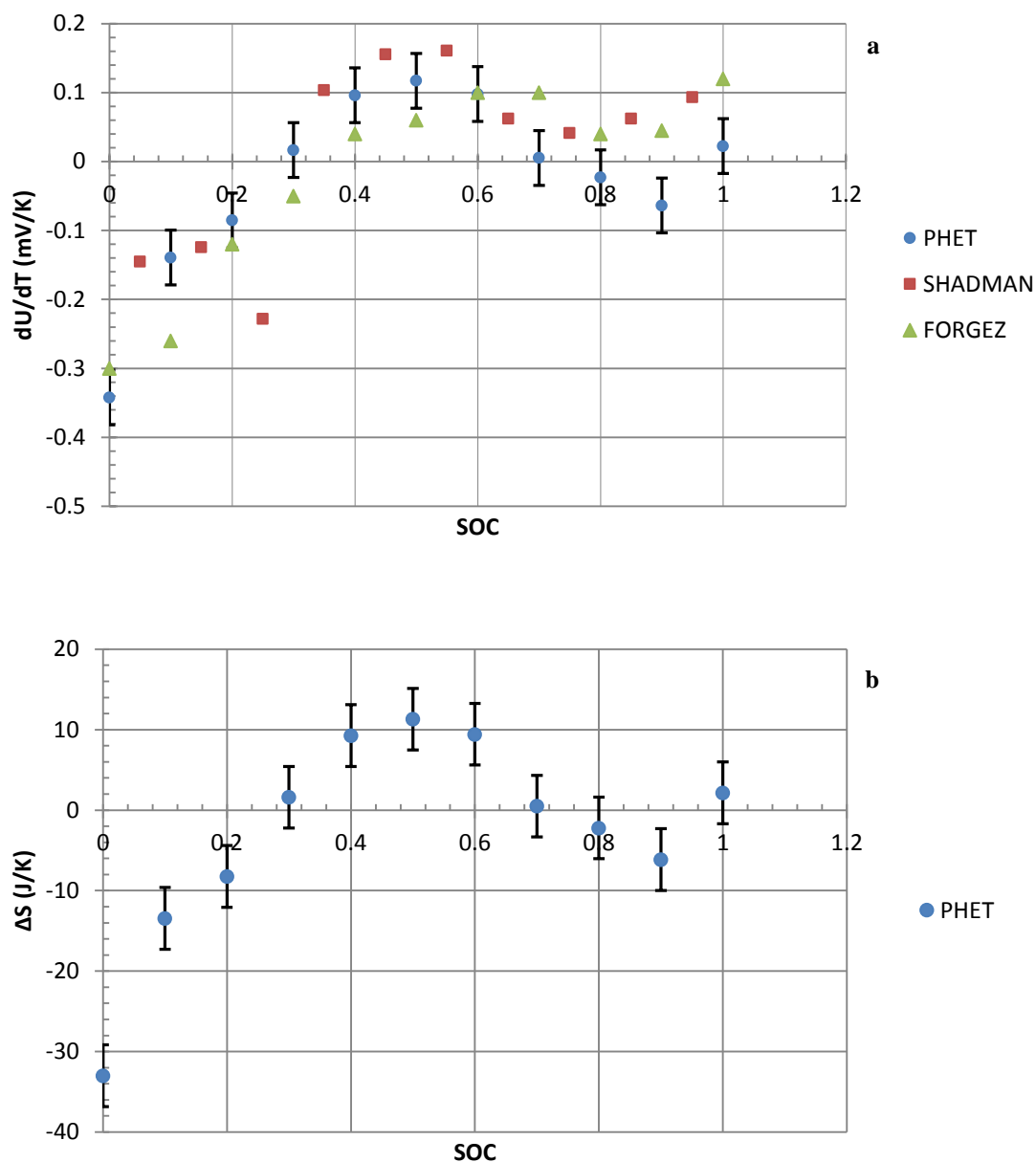


**Figure 4.3:**  $\frac{\partial U_{ocv}}{\partial T}$  values calculated as a function of SOC at 25°C and values reported at 25°C by (a) *Forgez et al.* [11] and *Shadman Rad et al.* [12] and (b)  $\Delta_r S$  values for the PHET battery

It is worth mentioning that the entropy change can be either negative or positive depending on the SOC. As a consequence, the reversible heat source acts as an endothermic term for SOC lower than 30% and becomes exothermic for higher SOC values. Moreover, negative values for the entropy change are observed for SOC close to 90% for our C-LFP battery technology (PHET) which is not the case for *Forgez et al.* [11] and *Shadman Rad et al.* [12]. The shape of this curve has been fully discussed by *Forgez et al.* [11]. Nevertheless, the reversible heat source term is most often not negligible as it is of the same order of magnitude as the irreversible term.

### 2.3.2. Irreversible heat source

The irreversible heat source term is directly estimated for each fast charging C-rates of the battery cell from the current and voltage values measurement thanks to the **Eq. 4.6**. **Fig. 4.4** represents the cell voltages of the battery cell during charging process (Fast charge with ODC method) at different C-rates as well as the OCV as functions of SOC. As expected, the cell voltage values increase linearly with the C-rate. This latter curve enables us to estimate the irreversible heat increase as the product of the current  $I$  by the cell voltage to OCV difference without the use of a complex electrochemical model as proposed by *Shadman Rad et al.* [12] for the battery discharge.

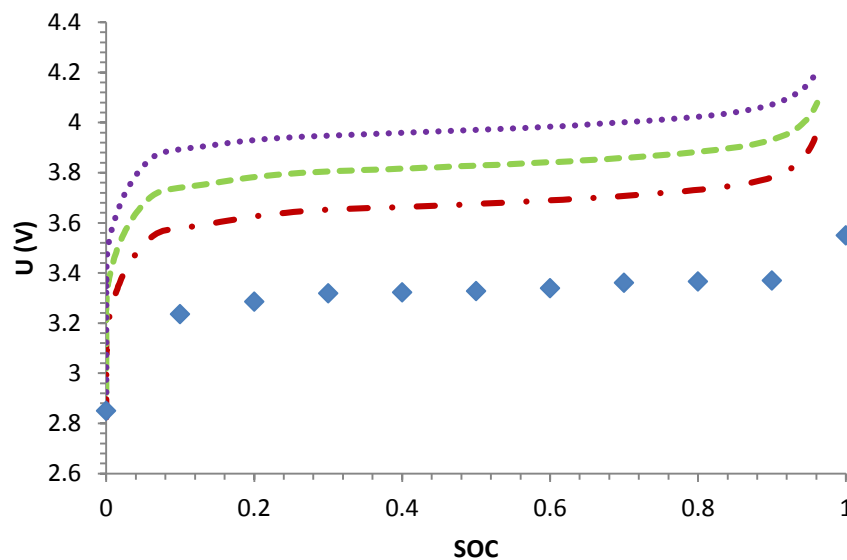


**Figure 4.4:** OCV curve  $\blacklozenge$  as a function of SOC along with the cell voltage curves as functions of SOC for 4C-rate  $- \cdot - \cdot -$ , 6C-rate  $- \cdot - \cdot -$  and 8C-rate  $\cdot \cdot \cdot \cdot \cdot \cdot$ .

## 3. 0D thermal model of Li-ion battery

### 3.1. Thermal model description

Three-dimensional thermal models have been used in order to provide a better insight about the thermal behavior of the battery cell [16]. Nevertheless, the prediction of the internal temperature distribution strongly depends on the cell architecture and the heat conductivity of the cell materials.

As the exact geometry of the cell is very difficult to implement, we have first considered a 0D thermal model for the Li-ion battery cell considering that the thermal conductivity is really high enough to observe a uniform temperature inside the battery. In other words, the battery cell is considered thermally thin (low Biot number). With this latter hypothesis, the full 3D battery model simplifies as a 0D model as proposed by *Rao and Newman* [19]:

$$mC_p \frac{d}{dt}(T) = \dot{Q}_{in} - hS(T - T_a) \quad (4.8)$$

Where  $m$  is the mass of the battery cell,  $S$  the lateral surface of the battery cell,  $T$  the temperature of the battery and  $T_a$  the ambient temperature. This thermal model of the cell is solved considering an initial condition assuming that the battery temperature is equal to ambient temperature:

$$T(0) = T_a \quad (4.9)$$

The Runge-Kutta method is used to solve the partial differential equation using Matlab software. The parameters of the model can be found in **Table 4.2** and also in **Chapter 2**. Note that during the CC stage the current  $I$  is constant whereas in the CV stage the latter decreases until the cut-off current value (see **Fig. 4.5**). This variation changes from C-rate to another. Accordingly to the current change, voltage varies during the CC stage while it is maintained constant during the CV stage equal to 3.65V. The heat generation  $\dot{Q}_{in}$ , which is the sum of irreversible heat  $\dot{Q}_R$  and reversible heat  $\dot{Q}_S$  as presented earlier in the section above, is calculated as a function of the battery SOC and current/cell voltage profiles. Namely, the irreversible terms is deduced from the experimental cell voltage curves (see **Fig. 4.4**) and battery current thanks to the **Eq. 4.6**. The procedure consists in calculating the difference between the cell voltage and the OCV whatever the SOC and multiplying this quantity by the battery current. For the reversible terms, the procedure is simpler and requires the determination of the entropy as a function of the battery SOC.

### 3.2. Simulation results and validation

**Fig. 4.5** allows comparing the predicted battery temperature with the 0D model to experimental data for the fast charge of the battery using the ODC method when the C-rate ranges from 4C to 8C.

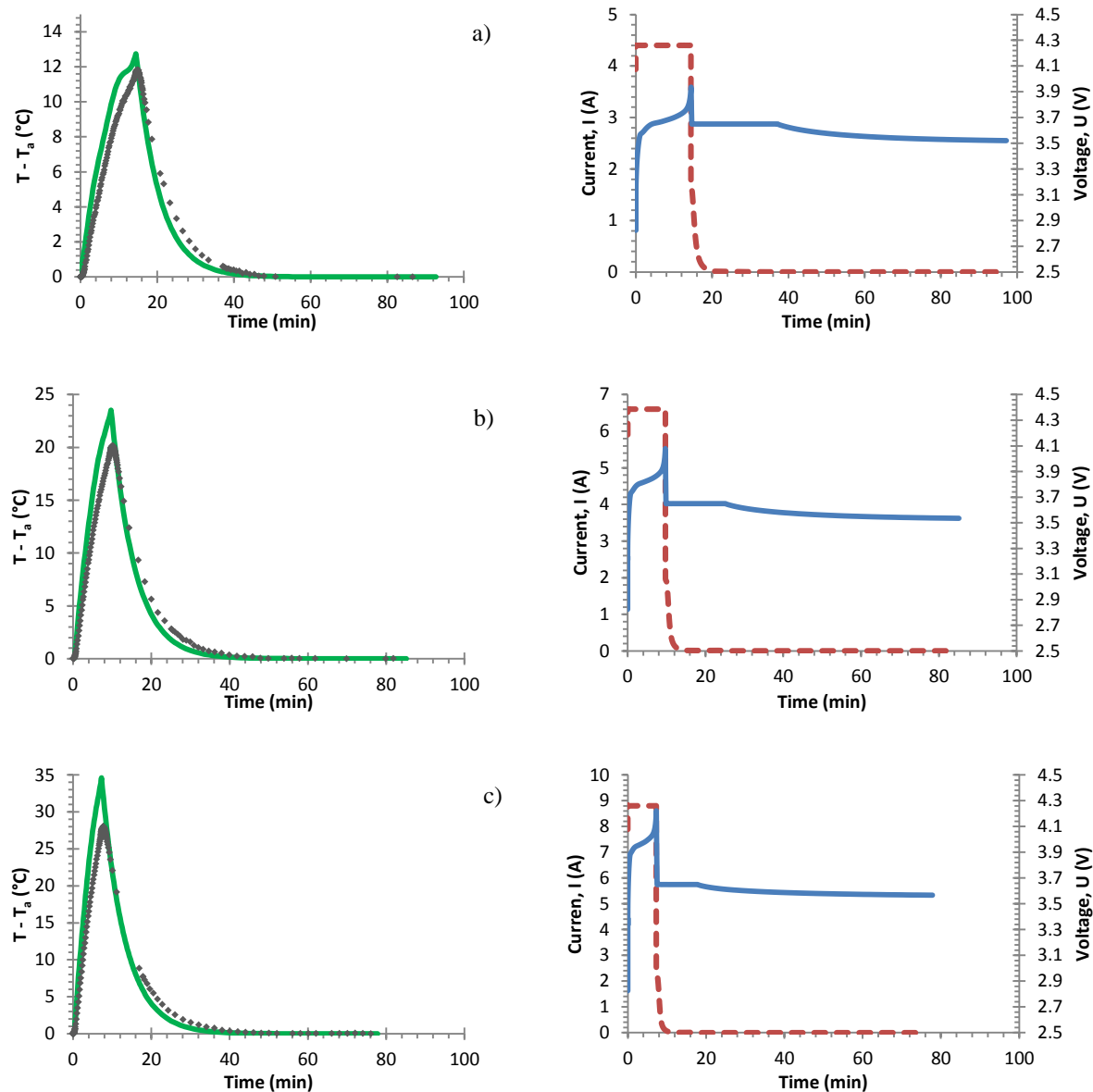


**Figure 4.5:** Simulated and experimental temperature changes of battery cell during fast charge with ODC for (a) 4C, (b) 6C and (c) 8C-rates along with their corresponding measured current and cell voltage curves with  $T_a = 25.5^\circ\text{C}$ . The green lines are simulated temperature results while the black dots are experimental results.

The battery cell temperatures are displayed as a function of time for both measured and simulated data. The corresponding experimental cell voltages and battery currents are also presented with the temperature curves. Even if a very simple model is used to simulate the thermal behavior of the battery, a quite good agreement is observed between the simulated and experimental results. Whatever the C-rate, the temperature of the battery first increases during the CC-stage to reach the maximum temperature at the end of CC-stage during charging process. During the next CV-stage, the battery temperature drops accordingly to the battery current decrease. These latter results are

neither surprising nor inconsistent with the literature. Nevertheless, the maximal battery temperature for C-rate higher than 6C exceeds the higher temperature limit given by the manufacturer during charging process (i.e. 45°C). This phenomenon worsens when the C-rate increase. For example, the battery temperature attains a value of about 55°C for 8C-rate. This phenomenon may accelerate battery ageing and capacity faded.

Nonetheless, the maximum temperature rise during CC-stage is more prominent for the simulated results than for the experimental ones. Moreover, these temperature differences between experiment and model amplify as the C-rate increase. However, the relative error of the gap is not really huge; about 2%, 7% and 12% for 4C, 6C and 8C respectively. Indeed, the parameters used in the 0D model allow predicting the temperature change of the battery with a quite good accuracy. It is worth mentioning that no fitting procedure has been used to determine the model parameters. Nevertheless, the gaps observed for the higher C-rate are likely related to possible temperature gradient inside the battery volume. So, the next section proposes a 2D axi-symmetric model of the Li-ion battery in order to investigate the possible impact of temperature change inside the battery.

## 4. “3D” thermal model of Li-ion battery

### 4.1. 2D axi-symmetric battery model

**Fig. 4.6** presents a schematic illustration of cylindrical Li-ion. The basic unit is composed of spirally-wounded jelly-roll and can. Although the jelly-roll is designed with cylindrically spiral type, the model represents it as a continuous media with an equivalent thermal conductivity for sake of simplicity. The simplified model enables two-dimensional description of the problem by adopting a cylindrical coordinate as shown in **Fig. 4.7**. Since the temperature distribution inside the battery is expected symmetric, axisymmetric heat transfer elements are employed for the simulation.

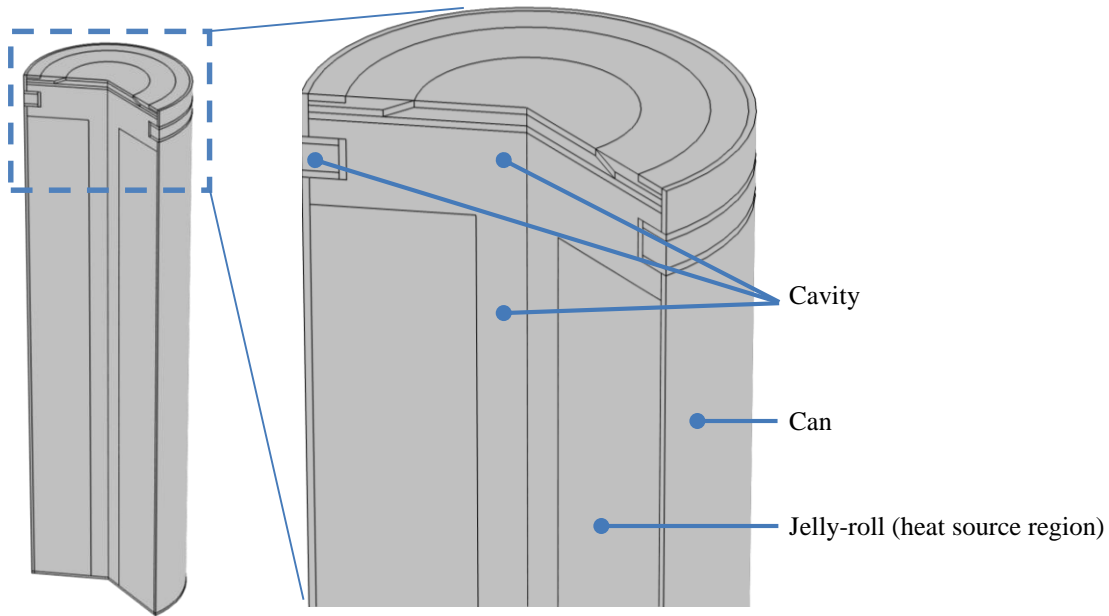


**Figure 4.6:** Schematic illustration of cylindrical Li-ion

From the 3D thermal model of the battery cell which has been described earlier in **Chapter 2, Section 2.2** along with all of its input parameters and boundary conditions, energy balance (**Eq. 4.1**) in cylindrical coordinate are given for:

- The Jelly-roll with heat source region:

$$\rho C_p \frac{d}{dt}(T) = \dot{q}_{in} + \frac{\lambda}{r} \frac{\partial}{\partial r} \left( r \frac{\partial T}{\partial r} \right) + \lambda \frac{\partial^2 T}{\partial z^2} \quad (4.10)$$

$\dot{q}_{in}$  [W/m<sup>3</sup>] being the internal heat source generation per unit volume expressed as follows:

$$\dot{q}_{in} = \frac{I \left[ (U - U_{OCV}) + \frac{T \Delta S}{nF} \right]}{V} \quad (4.11)$$

Where  $V$  is the battery volume.

- As well as the can and the cavity without heat source region:

$$\rho C_p \frac{d}{dt}(T) = \frac{\lambda}{r} \frac{\partial}{\partial r} \left( r \frac{\partial T}{\partial r} \right) + \lambda \frac{\partial^2 T}{\partial z^2} \quad (4.12)$$

Where  $r$  and  $z$  are radial and axial coordinates respectively and  $\lambda$  the “effective” thermal conductivity. Note that derivatives with respect to the tangential coordinate are absent since the considered problem possesses radial symmetry.

Axi-symmetric and convective heat transfer boundary conditions are applied to the inside and outer surface respectively. The heat transfer,  $\varphi$  from the battery surface to the ambient air can be calculated by the **Eq. 4.2**. The initial temperature condition for this model is that all the materials are at the ambient temperature initially.

The thermal model is simulated using Comsol Multiphysics. The above governing equations are discretized by the numerical simulation method. The simulated region is the two dimensional cross-section of the battery. It is constructed using axi-symmetric heat transfer element. The model is meshed up with mapped meshing using the free triangular-shaped elements as shown in **Fig. 4.7**. To simplify the simulation, the effect of the Jelly-roll structure of the battery on the distributions of the electrical properties is assumed to be negligible and the heat source region is considered to be uniformly distributed. Moreover, the thermal conductivity of the Jelly-roll is also considered uniform along and across the battery volume.

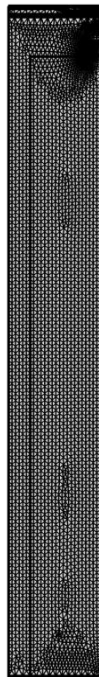


**Figure 4.7:** Schematic illustration of free-triangular mesh of cylindrical Li-ion battery

The thermal model of cylindrical Li-ion battery simulates the temperature change during the fast-charging with ODC method at various C-rates (i.e. 4C, 6C and 8C-rates) using time-dependent method.

## 4.2. Sensibility analysis of the thermal conductivity

As invoked earlier, the thermal conductivity of the battery cell is really hard to determine. The battery cell is made up from many materials with different thermal characteristic and a complex cylindrical design (see **Fig. 4.1**). **Table 4.3** summarizes the thermal conductivities for each layer of a C/LFP battery cell [20] and the corresponding thickness.

**Table 4.3.** Thermal conductivity of C-LFP battery cell [20]

	Thickness (mm)	Thermal conductivity, $\lambda$ (W/(m.K))
Electrolyte	-	0.45
Separator	0.014	0.334
Graphite electrode (+ collector Cu)	0.083	1.04 (385)
LiFePO <sub>4</sub> electrode (+ collector Al)	0.145	1.48 (205)
Aluminum can	0.3	205
Plastic wrap	0.1	0.2 - 0.5

In the literature [20], the effective thermal conductivity of C/LFP battery cell ranges widely from 0.2 to 1.48 W/(m.K). Different methods have been used to determine this latter parameter for a cylindrical battery cell such as internal thermocouple strategy [11], heat flux measurement methods [21,22], Xenon-Flash method [22], and thermal impedance spectroscopy [23]. However, these methods are generally extensive, cost-intensive, cell destructive and time consuming.

However, the effective value of thermal conductivity for the jelly-roll can be estimated considering that it consists in sandwich of 5 foils. The resistance of the sandwich is then the sum of the 5 thermal conduction resistances that depends on both the foils thickness and the thermal conductivities of the materials:

$$R_{Sand} = \left(\frac{e}{\lambda}\right)_{LFP} + \left(\frac{e}{\lambda}\right)_{Al} + \left(\frac{e}{\lambda}\right)_{Graphite} + \left(\frac{e}{\lambda}\right)_{Cu} + \left(\frac{e}{\lambda}\right)_{separator} \quad (4.13)$$

Where  $e$  and  $\lambda$  are the thickness and thermal conductivity of the materials accordingly. The effective thermal conductivity ( $\lambda_{eff}$ ) is finally obtained considering the total thickness ( $e_{sand}$ ) of our sandwich of 5 foils and given by:

$$\lambda_{eff} = \frac{e_{Sand}}{R_{Sand}} = 1.35 \text{ W/(m.K)} \quad (4.14)$$

It is worth mentioning that this latter value is in the range of the values given by the literature. Nonetheless, this value is certainly overestimated neglecting the contact resistance between each foil.

Owing to the dependence of the inner temperature gradient to this parameter, a sensibility analysis of the thermal conductivity is performed on the 2D thermal model by varying its value from 0.2 to 3. **Fig. 4.8** shows the maximum temperatures at the center of the battery (internal) and the minimum at the lateral surface (external) for different values of thermal conductivity. It is worth mentioning that this maximal temperature difference is reported at the end of the CC stage.

As expected, the temperature difference between the inner and the outer temperature strongly depends on this effective thermal conductivity. As the thermal conductivity value rises, both of the maximum temperatures lean towards a plateau value. However, their variations are inversed from each other. Indeed, the inner temperature decreases while the outer temperature increases as the thermal conductivity rises. As expected, the internal temperature gradient becomes insignificant for effective thermal conductivity larger than 2 but remains significant for a value lower than 1. As an effective thermal conductivity ranging from 0.2 to 1.48 W/(m.K) is expected for our battery, significant temperature gradients are likely observed.

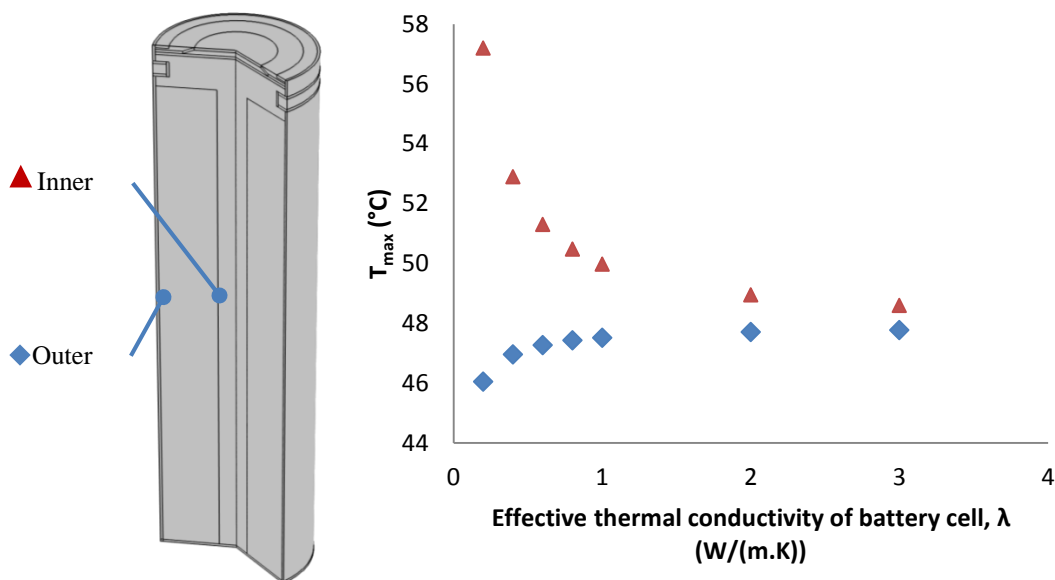


**Figure 4.8:** Simulated maximum temperatures at the center of the battery  $\blacktriangle$  and minimum at the lateral surface (external)  $\blacklozenge$  of the cylindrical Li-ion battery for different values of the effective thermal conductivity for the Jelly-roll in the case of a fast-charge at 6C-rate with ODC method.

**Fig. 4.9** shows the simulated surface temperature profile for fast-charge rate at 6C. The temperature change is significant in this operation condition because of the large amount of heat produced at high current. The comparison between experimental and simulated results shown in **Fig. 4.9** indicates that the thermal conductivity should be about 0.2 W/(m.K) in order to observe a good concordance between them. Nevertheless, this value is quite low compared with the value proposed by the literature and would predict very significant internal temperature increase up to 58°C. Conversely, higher value such as the one calculated from the material properties (i.e. 1.4 W/(m.K)), would forecast lower inner temperature up to 50°C. One study done by *Fleckenstein et al.* [23] used the thermal impedance spectroscopy (TIS) method to determine the thermal conductivity. It is interesting to point out that their C/LFP cylindrical battery cell and ours are very similar in terms of dimension. Considering this circumstances, we assumed that our thermal conductivity has to be close to their value of 0.35 W/(m.K). Moreover, *Shadman Rad et al.* [12] used a thermal conductivity value of 0.4 W/(m.K) for thermal simulations of a bigger cylindrical C/LFP battery. These latter values for the thermal conductivity of the jelly-roll are three times lower than the one calculated earlier. As the matter of fact, that calculated value does not take into account thermal resistances linked to the contact of the material inside the sheet of the jelly-roll, and also between the sheets themselves are unknown. So, in reality the exact value of thermal conductivity should be lower than the value estimated with **Eq. 4.14**.

So, according to this sensibility analysis, considering all the circumstances, the value of the effective thermal conductivity in our case is set to 0.35 W/(m.K) to have a good accuracy in regard of all the relative error of all other parameters.

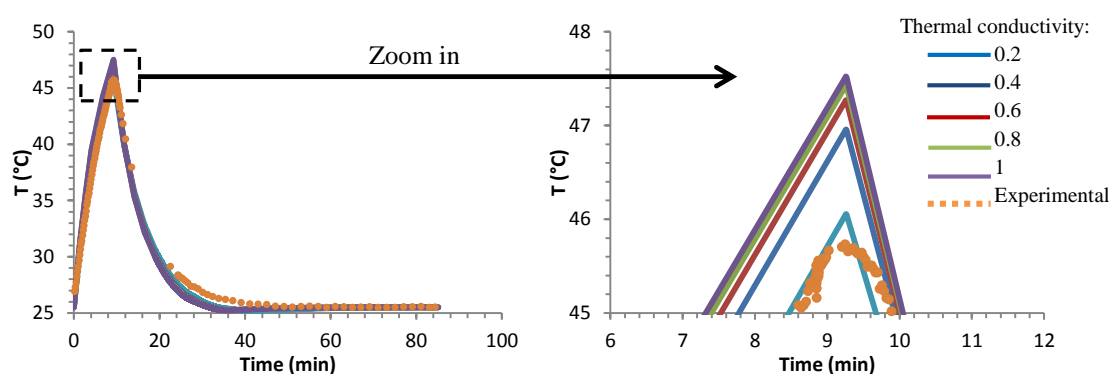


**Figure 4.9:** Experimental and simulated surface temperature curves during fast-charging with ODC method at 6C-rate for different value of thermal conductivity.

**Fig. 4.10** shows the simulated surface temperature changes of the battery as well as the experimental ones during fast-charging with ODC method at 4C, 6C and 8C-rates for the chosen

thermal conductivity. Similarly to the 0D result presented previously, the model is able to predict the temperature increase during the CC-stage of the charging process to reach the maximum temperature at the end of CC-stage as well as the temperature drop during the CV-stage. The simulated results match the experimental one whatever the C-rates. However, even if the model has been improved taking into account the internal temperature gradient, the simulated surface temperatures remain a little bit higher than the experimental ones. Nonetheless, compared to the 0D study, these results are much more accurate even if the gap rises as the C-rate increase. Obviously, a very good agreement between experiment and simulation is recorded for 4C and 6C-rate. However, model forecasting worsens for higher C-rates (i.e. 8C). Indeed, the maximum temperature gap is still quite substantial and it is about 3.5°C for this 2D model whereas it is about 10°C for the 0D model. The gap between experiment and simulation values most probably due to the contact thermal resistance between the thermal sensor and the can. The contact thermal resistances cannot be taking into account in the simulation process.

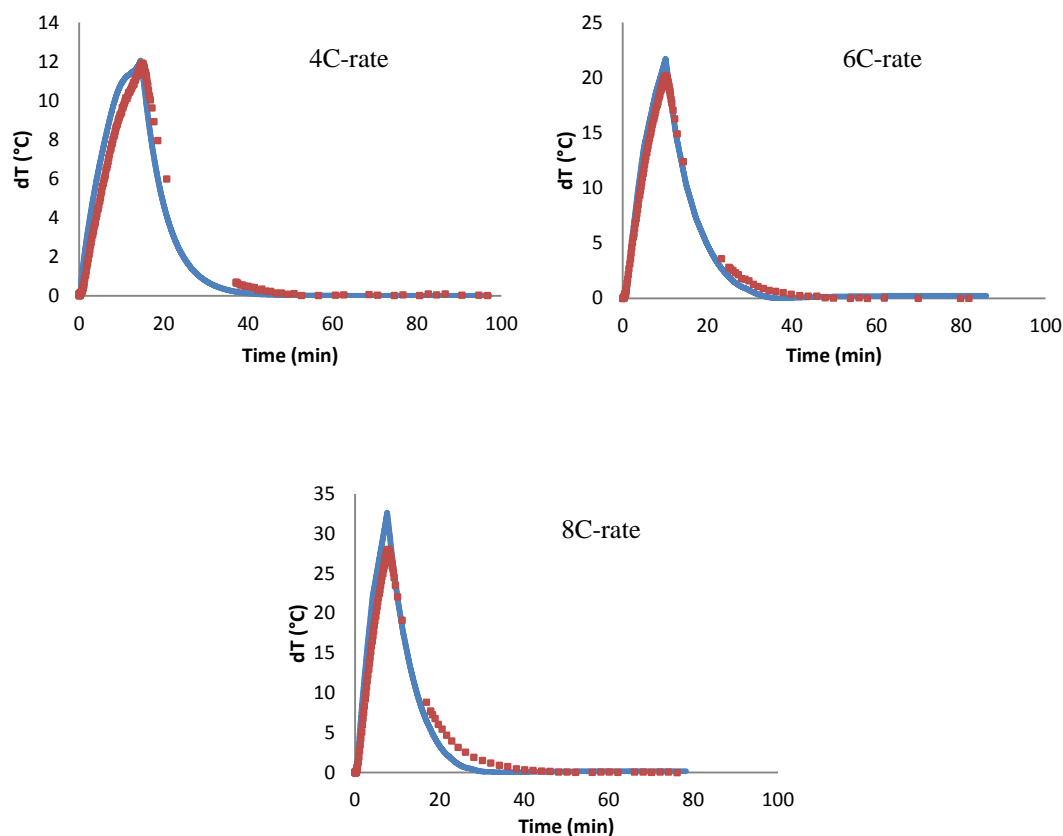


**Figure 4.10:** Surface temperature curves of measured  $\blacklozenge$  and simulated  $\text{—}$  values for 4C, 6C and 8C-rates as functions of time.

Although the gap is still present notably at higher C-rate (e.g. 8C-rate), this result also indicates that the 3D model is more precise than the 0D model and has a more similar tendency with the experimental data.

### 4.3. Simulation of internal gradient of temperature

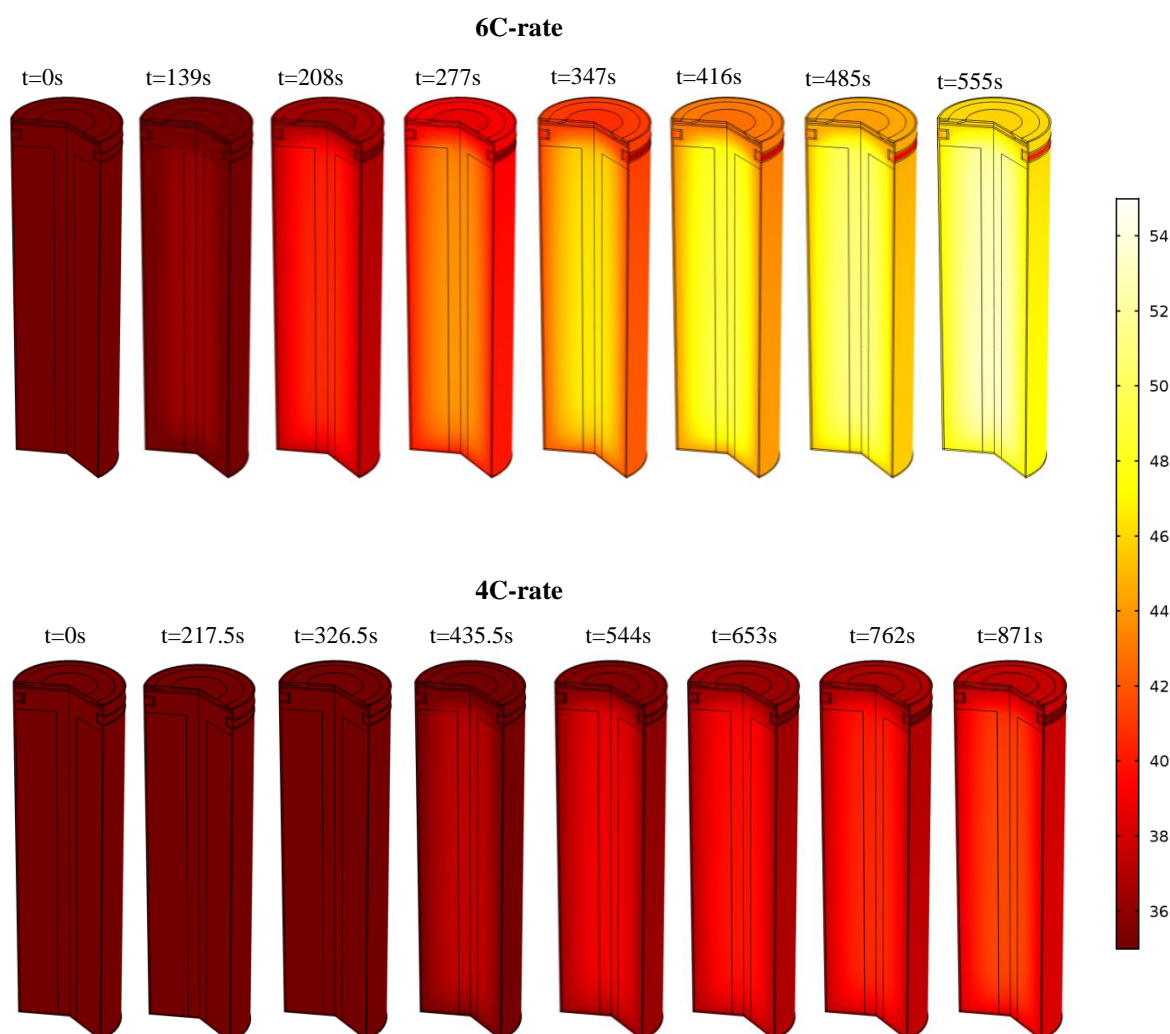


**Figure 4.11:** Temperature distribution of cylindrical Li-ion battery cell at different simulation sequence during the CC-stage for fast-charging ODC method of 4C-rate and 6C-rate.

The predicted temperature distributions inside cylindrical Li-ion battery cell at different time-step (during the first 10 minutes of the charge corresponding to the CC-step) are illustrated in **Fig. 4.11** during the CC-step of fast charging at 4C and 6C-rates (high level). At the beginning of fast-charging

process, the battery has uniform temperature distribution i.e. 0 s. As the charging time increased, it becomes non-uniform due to the heat production and the heat dissipation at the surface caused by air convection. The non-uniformity across the battery is not really significant at the beginning. However, this situation change as the battery heats up more during the charging process as shown for  $t=227$  s and  $t=347$  s for examples at 6C-rate. High temperature is observed inside the battery since the heat generation occurs at the jelly-roll. Moreover, as the C-rate increase, the heat generation inside the jelly-roll rises significantly, contributing to higher elevation of battery temperature. Indeed, the temperature elevation for 4C-rate is less prominent than the one for 6C-rate. Conversely, for higher C-rate, the battery undergoes higher temperature increase.

**Fig. 4.12** depicts a cross-section radial temperature of the battery cell at the end of the CC-step for fast charge with ODC method (low and high compensation rates) as well as the reference method at 25 and 45°C. It is worth mentioning that the inner temperature profiles have parabolic shape for fast charge showing a significant internal temperature gradient. Conversely, the inner temperatures are nearly homogeneous in case of the reference method. In the case of fast charge with ODC method, the inner temperatures clearly exceed the recommended of 45°C whatever compensation level at 6C-rate. Indeed, the simulated external surface temperature is 46.9°C while the maximal internal temperature reaches about 52.9°C for high level. If the battery is charge with the reference method at 1 C at 25 and 45°C, the heat production is quite low and the battery experiences a very low temperature increase up to 27°C and 47°C respectively.

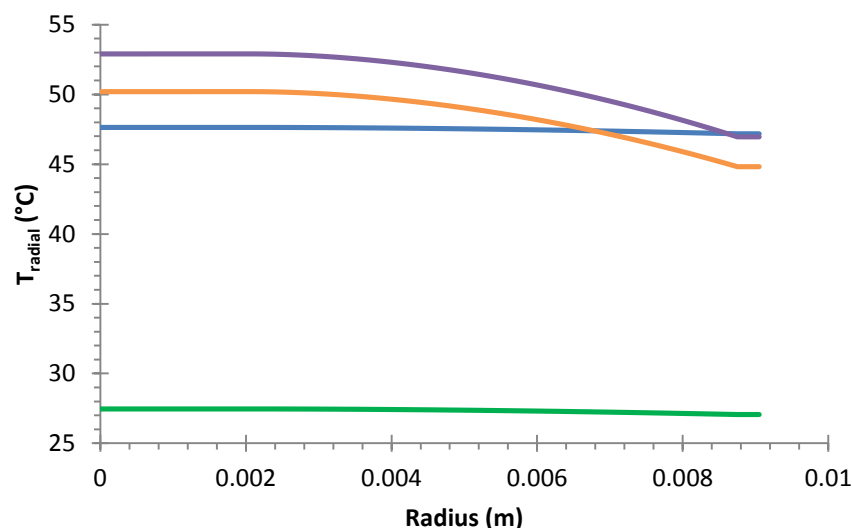


**Figure 4.12:** Simulated cross-section radial temperature of the battery at the end of the CC stage for high level — and low level — ODC method at 6 C-rate and reference method at 25°C — and 45°C — .

Consequently, the temperature range observed during charge with the reference method at 45°C and fast charge with ODC method are quite similar. The significant internal temperature increase for fast charge with ODC method and reference method at 45°C may accelerate ageing of the Li-ion battery. Post-mortem analysis is performed in the next chapter to investigate this phenomenon.

#### 4.4. Influence of the ambient temperature

The battery could operate at low or high ambient temperature depending on the application. The influence of this latter parameter is performed by considering an ambient temperature equal to either 25 or 45°C. In both conditions, the simulation results match with experimental data. As the battery is charge with the reference method, the heat production is quite low and the battery experiences a very low temperature increase up to 27°C and 47°C respectively. The results are shown in **Fig. 4.13**.

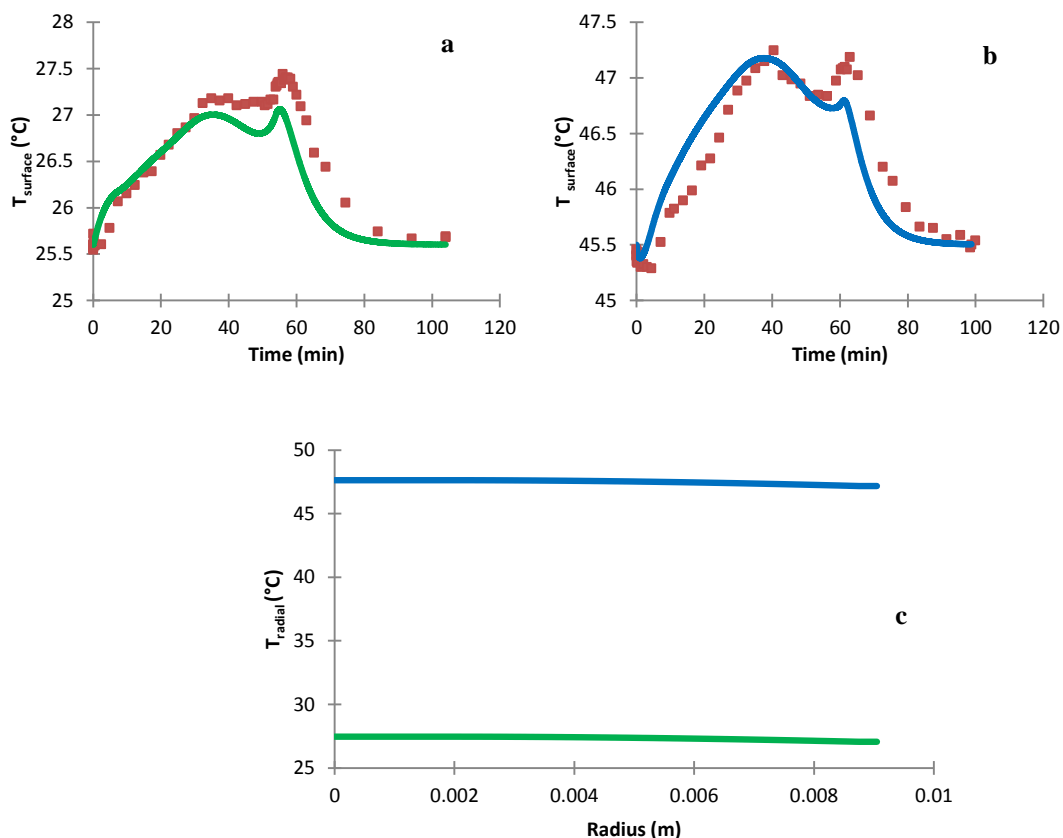


**Figure 4.13:** Surface temperature curves of measured ■ and simulated ones for different value of ambient temperature at (a)  $T_a = 25^\circ\text{C}$  — and (b)  $T_a = 45^\circ\text{C}$  — and also their (c) simulated cross-section radial temperatures using the reference method.

#### 4.5. Influence of the battery cooling

As shown above, a significant temperature rise is expected at high charging rates with ODC method. Cooling the battery could be effective in depressing the temperature. As presented in **Chapter 2**, the cooling system consists of an air canal and a fan to simulate a forced air convection situation around the battery for cooling purpose. The use of that cooling system allows a significant decrease in the outer surface temperature. Indeed, with a ventilation system, a substantial amount of heat is evacuated and the battery cools down to a maximal surface temperature about 36.4°C while a maximal temperature of 47°C was measured without cooling. In this section, the thermal model is used to forecast the temperature of battery during the fast charging process in presence of air cooling. **Fig. 4.14** presents the simulated surface temperature change for two different values of the heat exchange coefficient ( $h=44$  and  $88 \text{ W}/(\text{m}^2\cdot\text{K})$ ) with the 0D and the 3D models as well as the measured surface temperature.

In **Chapter 2**, the value of heat transfer coefficient inside the air canal has been estimated about to  $44 \text{ W}/(\text{m}^2\cdot\text{K})$ . Using that same value for simulation purpose, the results are not actually accurate. As shown in **Fig. 4.14**, the predicted temperature profiles are always higher than the experimental whatever the model. Indeed, the maximum surface temperature reaches about 41°C and 42.5°C for 0D and 3D simulation respectively while experimental shows that the maximum surface temperature reach a peak at 35°C. Considering the simulation result in the section above, the sole difference here is the value of heat transfer coefficient. The value of heat transfer in **Chapter 2** is calculated using a correlation while the one used in the above section is from experimental results. In our opinion, the one deduced with the experimental results is more accurate than the one obtained from a correlation. So, a sensitivity analysis to the heat transfer coefficient has been performed in order to determine a more convenient value.

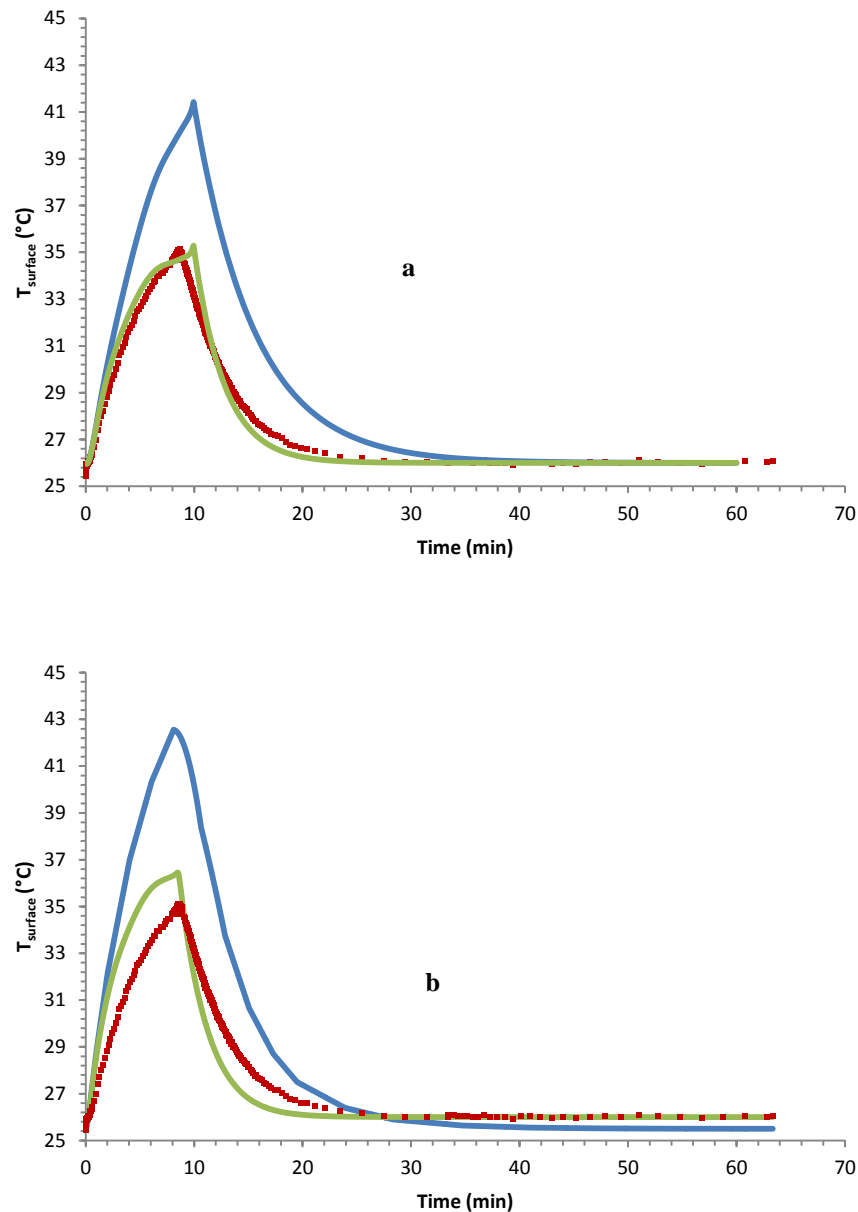


**Figure 4.14:** Surface temperature curves of measured  $\blacklozenge$  and simulated ones for different value of heat transfer coefficient ( $h=44 \text{ W}/(\text{m}^2\cdot\text{K})$  — blue — and  $h=88 \text{ W}/(\text{m}^2\cdot\text{K})$  — green —) for (a) OD (MATLAB) and (b) 3D (COMSOL) thermal models at 6C-rates as functions of time.

If considering a higher value of heat transfer coefficient of about two times of the previous value, the results are more accurate. Indeed, with a heat transfer coefficient of  $88 \text{ W}/(\text{m}^2\cdot\text{K})$ , a better agreement between simulated and experimental results is observed. Now, the maximum surface temperatures recorded are about  $35.3^\circ\text{C}$  and  $36.4^\circ\text{C}$  for OD and 3D simulation respectively. The OD simulation has less deviation and less relative error when compared to the experimental temperature curves. However, the one for the 3D simulation has a more prominent deviation. As depicted in **Fig. 4.14**, the surface temperature climb is steeper than the experimental one before

reaching the maximum value. This trend is also observed during the temperature drop where it drops faster than the experimental data. Considering that this result is valid for our purpose, the internal temperature for this experiment situation could be determined by using the 2D model.

**Fig. 4.15** shows the temperature curves of a cross-section radial temperature of the battery cell at the end of the CC-stage for 6C-rate of fast charging ODC method (high level) with and without air cooling system. As previously presented in the above section, the temperature curves have parabolic shape in the both cases. However, compared to the one without the cooling system, the temperature is lowered in cooling condition. Indeed, the temperature increases from 36.4°C up to 45.3°C respectively at the surface and in the battery center with air cooling. This result highlights that the battery could be cooled down thoroughly of about 10°C with a simple air cooling system. It should be noted, however, that the use of a cooling system also results in a higher temperature gradient (0.99°C/mm compared to 0.61°C/mm).

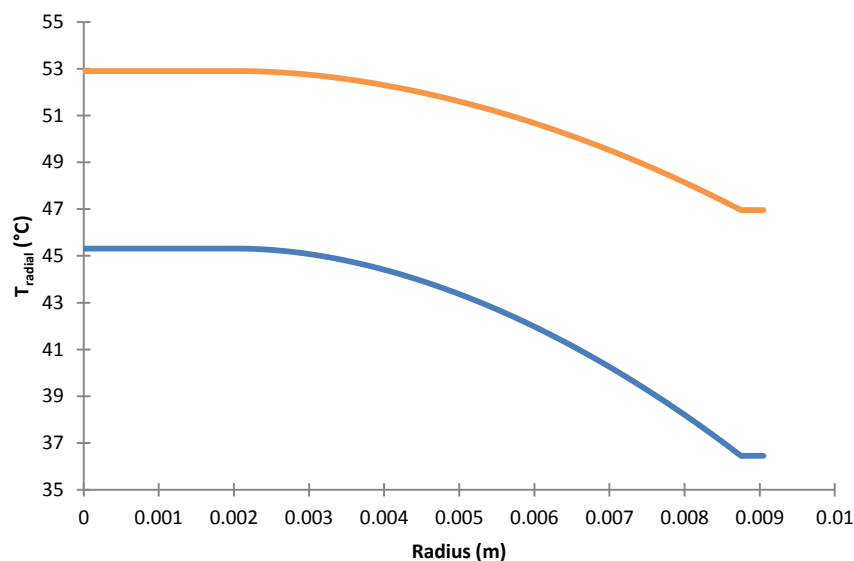


**Figure 4.15:** Temperature curves of a cross-section radial temperature of the battery cell at the end of the CC-stage for 6C-rate of fast charging ODC method with air cooling system with  $h=88 \text{ W}/(\text{m}^2.\text{K})$  — and without cooling system at  $h=27 \text{ W}/(\text{m}^2.\text{K})$  —.

## 5. Conclusion

The experiments conducted to deduce the battery cell thermal parameters such as the heat transfer coefficients,  $h$  and the heat capacity,  $C_p$  appear to be quite successful. However, the overall thermal conductivity,  $\lambda$  of the battery is really hard to measure and to calculate because of the lack of apparatus and also the fact that the battery cell is made up of layered multi-material jelly-roll. So, a sensibility analysis using the 2D thermal model is performed to estimate the most effective value of the latter. Other parameter like the entropy has also been measured and our results are very similar with others. With all that parameter values, the thermal simulations come out to have a really good agreement with the experimental result.

In the 0D thermal model using Matlab, for lower C-rate, for example at 4C-rate, the simulation results have a more similar tendency with the experimental data compared to higher C-rates and this indicates that the thermal parameters used are close to the real value. So, to go further, the thermal simulations have also been conducted in simplified 2D thermal model. Even though the thermal model is simplified, the results are really encouraging and important in this study because they allow us to make a good estimation of the internal temperature of the battery cell, which is the real objective of this chapter.

As expected, the internal temperature of the cylindrical C-LFP battery can be determined using the 2D thermal model successfully, especially at maximum temperature elevation during fast charging ODC method. With this information in hand, a more rigorous study concerning the ageing of the battery caused by the heat generation of the battery can be conducted. The latter will be discussed further in the next chapter. On the whole, the thermal model that has been developed and also the method to get there can be really useful to forecast the internal temperature of the cylindrical battery cell during fast charging using ODC method.

## 6. References:

- [1] M. H. Noh, P. X. Thivel, C. Lefrou, Y. Bultel, Fast-charging of lithium iron phosphate battery with ohmic-drop compensation method, *Journal of Energy Storage*, 8(2016), pp.160 - 167.
- [2] B. Wu, V. Yufit, M. Marinescu, G. J. Offer, R. F. Martinez-Botas, N. P. Brandon, Coupled thermal-electrochemical modelling of uneven heat generation in lithium-ion battery packs, *Journal of Power Sources*, 243(2013), p.544 - 554.

- [3] P. M. Gomadam, R. E. White, J. W. Weidner, Modeling heat conduction in spiral geometries. *Journal of The Electrochemical Society*, 150(10)(2003), pp.A1339 - A1345.
- [4] S. Al Hallaj, H. Maleki, J. S. Hong, J. R. Selman, Thermal modeling and design considerations of Lithium-ion batteries, *Journal of Power Sources*, 83(1)(1999), pp.1 - 8.
- [5] E. Prada, D. Di Domenico, Y. Creff, J. Bernard, V. Sauvant-Moynot, F. Huet, Simplified electrochemical and thermal model of LiFePO<sub>4</sub>-graphite Li-ion batteries for fast charge applications, *Journal of The Electrochemical Society*, 159(9)(2012), pp.A1508 - A1519.
- [6] M. Ecker, T. K. D. Tran, P. Dechent, S. Käbitz, A. Warnecke, D. U. Sauer, Parameterization of a physico-chemical model of a lithium-ion battery I. determination of parameters, *Journal of The Electrochemical Society*, 162(9)(2015), pp.A1836 - A1848.
- [7] M. Doyle, J. P. Meyers, J. Newman, Computer simulations of the impedance response of lithium rechargeable batteries, *Journal of The Electrochemical Society*, 147(1)(2000), pp.99 - 110.
- [8] T. F. Fuller, M. Doyle, J. Newman, Simulation and optimization of the dual lithium ion insertion cell, *Journal of The Electrochemical Society*, 141(1)(1994), pp.1 - 10.
- [9] V. R. Subramanian, V. Boovaragavan, V. Ramadesigan, M. Arabandi, Mathematical model reformulation for lithium-ion battery simulations: Galvanostatic boundary conditions, *Journal of The Electrochemical Society*, 156(4)(2009), pp.A260 - A271.
- [10] K. A. Smith, C. D. Rahn, C. Y. Wang, Control oriented 1D electrochemical model of lithium ion battery, *Energy Conversion and management*, 48(9)(2007), pp.2565 - 2578.
- [11] C. Forgez, D. V. Do, G. Friedrich, M. Morcrette, C. Delacourt, Thermal modeling of a cylindrical LiFePO<sub>4</sub>/graphite lithium-ion battery, *Journal of Power Sources*, 195(9)(2010), pp.2961 - 2968.
- [12] M. Shadman Rad, D. L. Danilov, M. Baghalha, M. Kazemeini, P. H. L. Notten, Adaptive thermal modeling of Li-ion batteries, *Electrochimica Acta*, 102(2013), pp.183 - 195.
- [13] D. H. Jeon, S. M. Baek, Thermal modeling of cylindrical lithium ion battery during discharge cycle. *Energy Conversion and Management*, 52(8)(2011), pp.2973 - 2981.
- [14] Y. Inui, Y. Kobayashi, Y. Watanabe, Y. Watase, Y. Kitamura, Simulation of temperature distribution in cylindrical and prismatic lithium ion secondary batteries, *Energy Conversion and Management*, 48(7)(2007), pp.2103 - 2109.

- [15] Y. Lai, S. Du, L. Ai, L. Ai, Y. Cheng, Y. Tang, M. Jia, Insight into heat generation of lithium ion batteries based on the electrochemical-thermal model at high discharge rates, *International Journal of Hydrogen Energy*, 40 (2015), pp.13039 - 13049.
- [16] K. Yeow, H. Teng, M. Thelliez, E. Tan, 3D thermal analysis of Li-ion battery cells with various geometries and cooling conditions using Abaqus, In proceedings of the SIMULIA Community Conference (May 2012).
- [17] D. Bernardi, E. Pawlikowski, J. Newman, A general energy balance for battery systems, *Journal of The Electrochemical Society*, 144(8)(1997), pp.2697 - 2704.
- [18] K. Onda, T. Ohshima, M. Nakayama, K. Fukuda, T. Araki, Thermal behavior of small lithium-ion battery during rapid charge and discharge cycles. *Journal of Power sources*, 158(1)(2006), pp.535 - 542.
- [19] T. Rao, J. Newman, Heat-generation rate and general energy balance for insertion battery systems, *Journal of The Electrochemical Society*, 144(8) (1997), pp.2697 - 2704.
- [20] G. Guo, B. Long, B. Cheng, S. Zhou, P. Xu, B. Cao, Three-dimensional thermal finite element modeling of lithium-ion battery in thermal abuse application, *Journal of Power Sources*, 195(8)(2010), pp.2393 - 2398.
- [21] E. W. Brooman, J. McCallum, Thermal conductivity measurements of nickel-cadmium aerospace cells Part I: Cell conductivities, *Journal of The Electrochemical Society*, 118(9) (1971), pp.1518 - 1523.
- [22] H. Maleki, S. Al Hallaj, J. R. Selman, R. B. Dinwiddie, H. Wang, Thermal properties of lithium-ion battery and components, *Journal of The Electrochemical Society*, 146(3)(1999), pp.947 - 954.
- [23] M. Fleckenstein, S. Fischer, O. Bohlen, B. Bäker, Thermal impedance spectroscopy - a method for the thermal characterization of high power battery cells, *Journal of Power Sources*, 223(2013), pp.259 - 267.



# **Chapter 5: Ageing study of C/LFP battery**

---



## 1. Introduction

In **Chapter 3**, the Ohmic-Drop Compensation method (ODC) was investigated for fast charge of graphite-LiFePO<sub>4</sub> battery. This latter ODC method is performed on Li-ion battery considering a higher upper-bound voltage limit,  $U'_f$  of the CC stage when taking into account the ohmic-drop resistance of the battery. In order to minimize the risk of side reactions in the case of over-compensation, a rate of compensation,  $\alpha$  is defined as a percentage of the internal resistance measured of the battery. In this condition, the new upper-bound limit voltage is given by:

$$U'_f = U_f + \alpha R_i I \quad (1)$$

Where  $\alpha$  is the compensation rate and  $R_i$  the internal battery resistance.

This latter fast-charge method highlights that, even though the high level ODC method saves a lot of total charging time, a temperature rises well beyond the constructor limit of 45°C is observed. As a consequence, the fast-charge may involve side reaction occurrence as well as higher cell temperature increase that induce fast ageing.

Regarding our fast charging with ODC, loss of lithium inventory may be induced by SEI growth or electrolyte/binder decomposition. These both degradation mechanisms are accelerated at high cell voltage and temperature. Especially at high voltage or high temperature, electrolyte could form gas bubbles inside the cell [1, 2]. Moreover, electrolyte additive components may also react leading to gas generation in the cell [3]. The second cause of capacity fade is the modification of the electrode's materials which results from the electrode particle cracking graphite exfoliation, structural disordering as well as loss of electric contact of the electrode when increasing the current load. The latter cause is the loss of active material (LAM).

Whatever the route for the capacity fade discussed in **Chapter 1**, loss of lithium inventory (LLI) or loss of active materials (LAM), they are mainly due to either the cell voltage or the temperature rise during fast charge with ODC. Thereby, the aim of this chapter is to investigate the impact of fast charging with ohmic-drop compensation method on graphite-LiFePO<sub>4</sub> battery ageing. Experimental setups as well as the test bench are detailed in the second chapter of the manuscript.

## 2. Cycling ageing

To study the impact of the ODC method on the battery life time, an ageing study is also carried out on graphite-LiFePO<sub>4</sub> cylinder cells manufactured by PHET (model: IFR13N0-PE1150) used in this study. All of the main battery parameters (geometry, capacity, mass, etc.) are summarized in **Chapter 2**. Two charging methods are compared. The reference charging method in which the battery is charge at 1 C-rate with an upper-bound voltage limit of  $U_f=3.65$  V. The ODC charging method, in which the battery is charged with a 6 C-rate until an upper-bound voltage limit of  $U'_f$  taking into account the ohmic-drop resistance of the battery ( $R_i = 70$  m $\Omega$ ) and a compensation rate ( $\alpha$ ) of 57% (low level) or 93% (high level). It is worth mentioning that the CV step is always performed at 3.65 V until a cut-off current of 10 mA whatever the charging method. After each charging process, the battery is discharged at a constant current of 1.5 C-rate until the lower-bound cut-off voltage is reached at 2V. When this cut-off voltage is reached, the discharging process is finished. The relax time between charges/discharges is set at 1 hour for the battery to cool down.

The ageing test is carried out, on one hand, for reference charge at 1 C-rate at ambient temperature and at  $T = 45^\circ\text{C}$  and, on the other hand, for the ODC method with two levels of compensation (low and high) at 6C-rate as well as high level ODC method with forced air convection. The result of the cycling process with these five protocols is shown in **Fig. 5.1** and **Table 5.1** summarizes the number of cycle to reach the EoL criterion and the duration of the cycling whatever the cycling protocol. The standard ISO 12405-02 defines battery end of life (EoL) as the point at which a specific test protocol or method cannot deliver more than 80% of its nominal capacity [4, 5, 6, 7]. In other words, the battery is considered to have reached its EoL criterion if the capacity fade is 20% of its nominal capacity according to its state of health, SOH.

As shown in **Fig. 5.1**, the SOH of the reference cycling process at ambient temperature shows a really slow diminution of its capacity. As expected, this reference method will prolong the battery life cycles as suggested by the manufacturer. The battery that sustains the high level ODC and the low level ODC methods reach their EoL criterion at about 320 and 1500 cycles respectively. As expected, the EoL criterion of the reference cycling process at ambient temperature is achieve for a number of cycles much higher than 1500 and exhibits a really slow diminution of its capacity. For the ageing test with the reference method at  $45^\circ\text{C}$ , EoL is achieved at a value of about 1300 cycles. For the same number of cycles, the capacity fade is only about to 2% at ambient temperature. The capacity loss for the low level ODC are quite similar to the one observed during the battery cycling at  $45^\circ\text{C}$ . This suggests that at low level ODC, the temperature is the main parameter leading to the cell

ageing. For the high level ODC, the capacity fade is more severe with an EoL after only 300 cycles and a cell maximal temperature of 47°C, close to 45°C. This result highlights the significant impact of the compensation rate. The fast ageing of the cell at high level ODC may be related to overcompensation and side reactions occurrence. These results highlight likely the effects of overcompensation as well as temperature on accelerated cell ageing. In order to mitigate the impact of the cell temperature, the high level ODC method with forced air convection is investigated. The battery's maximum temperature was kept well below 45°C at about 35°C with forced air convection. In this case, the capacity degrades almost two times slower and the cell reaches the EoL criterion at about 580 cycles. So, the presence of airflow around the battery charged at 6C with a high level of compensation mitigates the temperature impact and allows extending the life of the battery from 320 up to 580 cycles. Regarding these results, even though the ODC method allows saving a lot of total charging time, it also impacts the battery cell life cycle. As explained in the introduction, the main degradations of the Li-ion batteries are related to either the current-voltage or the temperature increase.

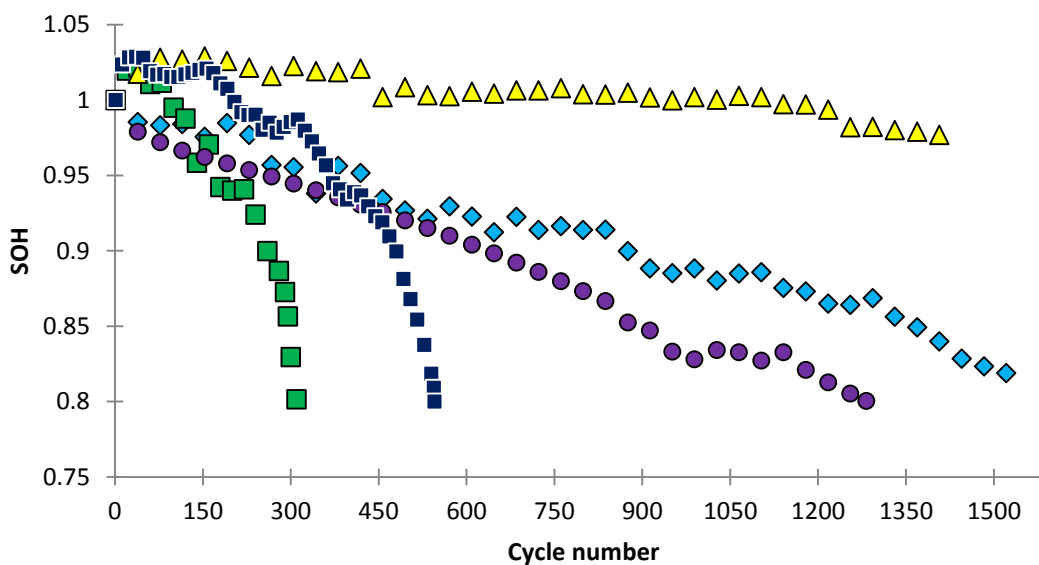


**Figure 5.1:** Life cycle test; the evolution of the battery's SOH of high level ODC method at 6C-rate ■, low level ODC method at 6C-rate ◆, high level ODC method at 6C-rate with air force convection ■, reference method inside 45°C enclosure ●, and reference method at ambient temperature ▲.

**Table 5.1:** Number of cycles to reach the EoL criterion

Charging method	Number of cycles to reach the EoL criterion	Duration of the cycling (days)
Reference method at ambient temperature	>> 1500	>> 500
Reference method inside 45°C enclosure	1300	184
Low level ODC method at 6C-rate	1500	217
High level ODC method at 6C-rate	320	42
High level ODC method at 6C-rate with air forced convection	580	50

**Fig. 5.2** presents the discharge curves for un-aged cell and aged cells at 80% State Of Health (SOH) with different charging protocols (high ODC level and reference method at 45°C). Even though the aged cells underwent two different charge procedures, the discharge curves for the same SOH loss (SOH = 80 %) are very similar. As the shape of their discharge curves does not change significantly during ageing, no information about the ageing mechanism can be distinguished.

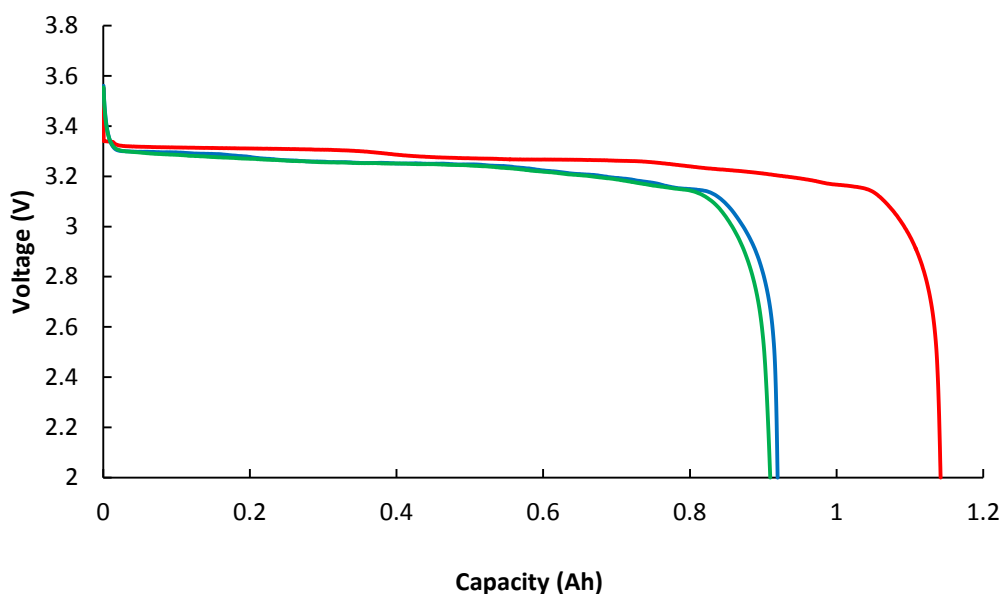


**Figure 5.2:** Discharge curves of un-aged cell (red), 45°C standard aged cell (SOH=80%) (blue) and 6 C- high level ODC aged cell (SOH=80%) (green).

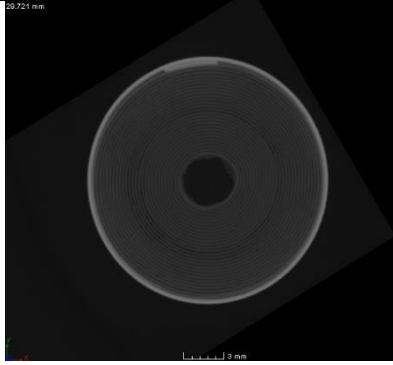
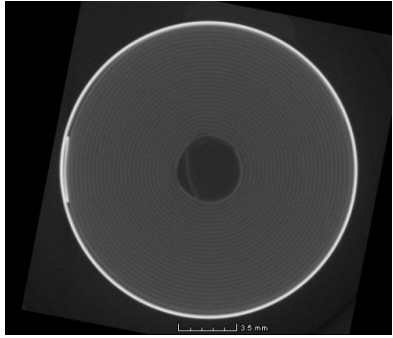
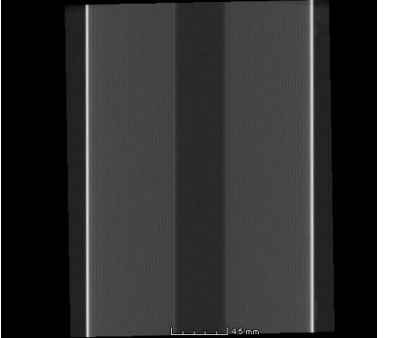
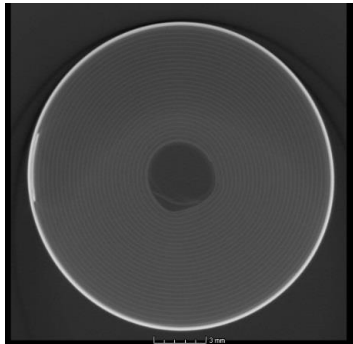
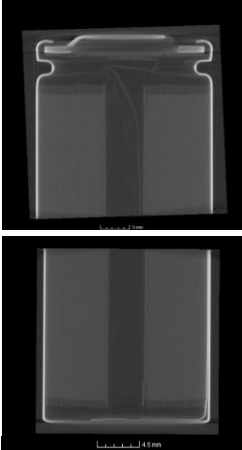
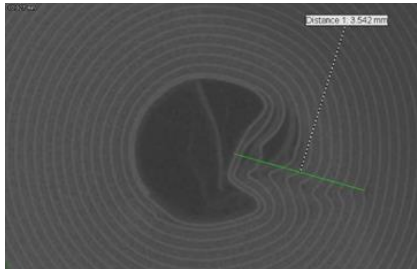
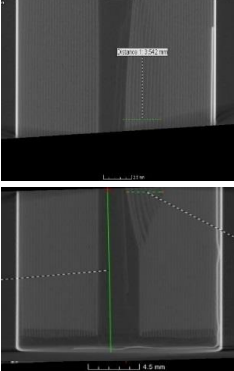
Regarding these results, even though the ODC method allows saving a lot of total charging time, it also impacts the battery cell life cycle. As explained in the introduction, the main degradations of the Li-ion batteries are related to either the current-voltage or the temperature increase. So, characterization of un-aged cell and aged cells in different conditions as well as nondestructive

inspection are performed and compared in order to determine the likely mechanism degradation due to fast charge with ODC.

### 3. Characterization of the aged LFP batteries

#### 3.1. X-Ray tomography photographs of batteries

It was demonstrated that, during fast charge, the battery exhibits high surface temperature changes and, according to the model, the battery experiences significant temperature gradients. For example, the predicted inner battery temperatures reach maximal values of 50°C and 53°C respectively for the low and high compensation rates at 6C-rate (see **Chapter 4**). At the same time, the cell voltage reaches highest value at the end of the CC stage. Regarding the capacity fade mechanism, these both effects may induce internal degradations resulting in a more or less rapid loss of capacity according to the chosen charging protocol. To go further in the ageing investigation and in the internal modification of the battery materials, X-Ray tomography has been completed on these batteries (**Fig. 5.3**). First, we can notice that the cell aged under reference condition does not exhibit significant change with regard to the un-aged cell. Indeed, the roll is regular and no defect can be observed on the image. In contrast, the 6C-high level ODC aged cell has a big defect in its roll. Namely, photography highlights that the roll has been deformed into the middle of the cell due to the absence of mandrel there. This is the only way for the winding to decrease the possible excess of pressure. So this kind of deformations reveals an increase of the internal pressure during ageing. This latter phenomenon may be related to the formation of gas bubbles. Moreover, it is worth mentioning that no deformation is observed for the cell aged with the reference method even at 45°C. The formation of gas bubbles conceivably comes from the oxidation of the electrolyte or electrolyte additive components at high voltage and high temperature (more than 45°C). The fast ageing of the cell seems to be related to the concomitant effect of cell voltage higher than 3.65V during fast charge with ODC and temperature higher than 45°C. Such gas emission has been already reported in the literature [1, 2, 3].

	Cross section	Longitudinal cross section
Un-aged cell		
Reference aged cell		
45°C aged cell		
6 C- high level ODC aged cell		

**Figure 5.3:** X-Ray tomography photographs of un-aged cell, reference aged cell, 45°C aged cell and 6 C- high level ODC aged cell.

### 3.2. Internal visual inspection of the batteries

As it has been shown on the X-ray tomography photographs, the 6C-high level ODC aged cell exhibits deformations of its winding and the consequences on the electrodes are shown on the pictures of **Fig. 5.4** after the cell has been dismantled. For useful comparison, an un-aged cell has been also dismantled. The deformations are clearly visible on the pictures of the aged cell by comparison to un-aged one. The induced folds have caused, at some places, delamination of the active material of the graphite electrode. Moreover, the upper and lower extremities of the electrode exhibit another aspect compare to the middle. It seems that, on these areas, the active material has been delaminated and stuck on the separator which turned black. Indeed, the gas bubbles increase the pressure on some parts of the roll and the electrodes were in a deep contact with the separator which facilitate the interpenetration of active material and caused the observed coloration.

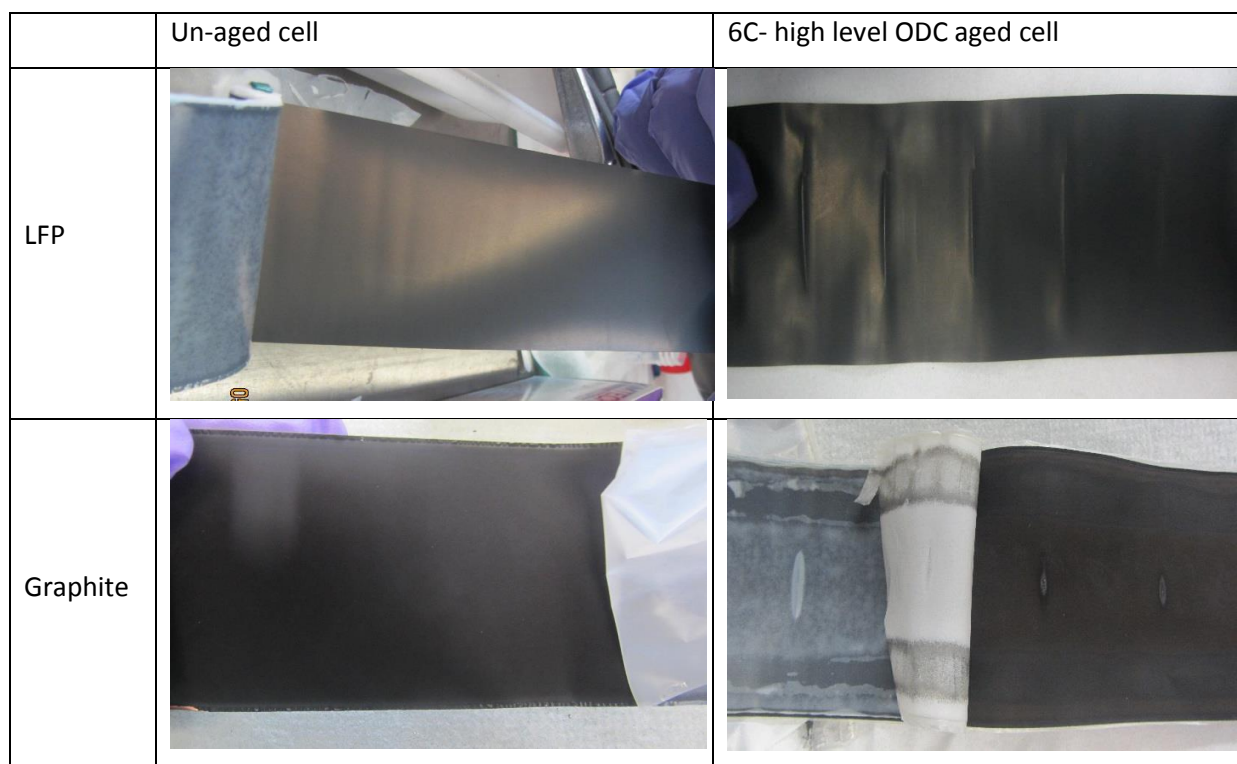
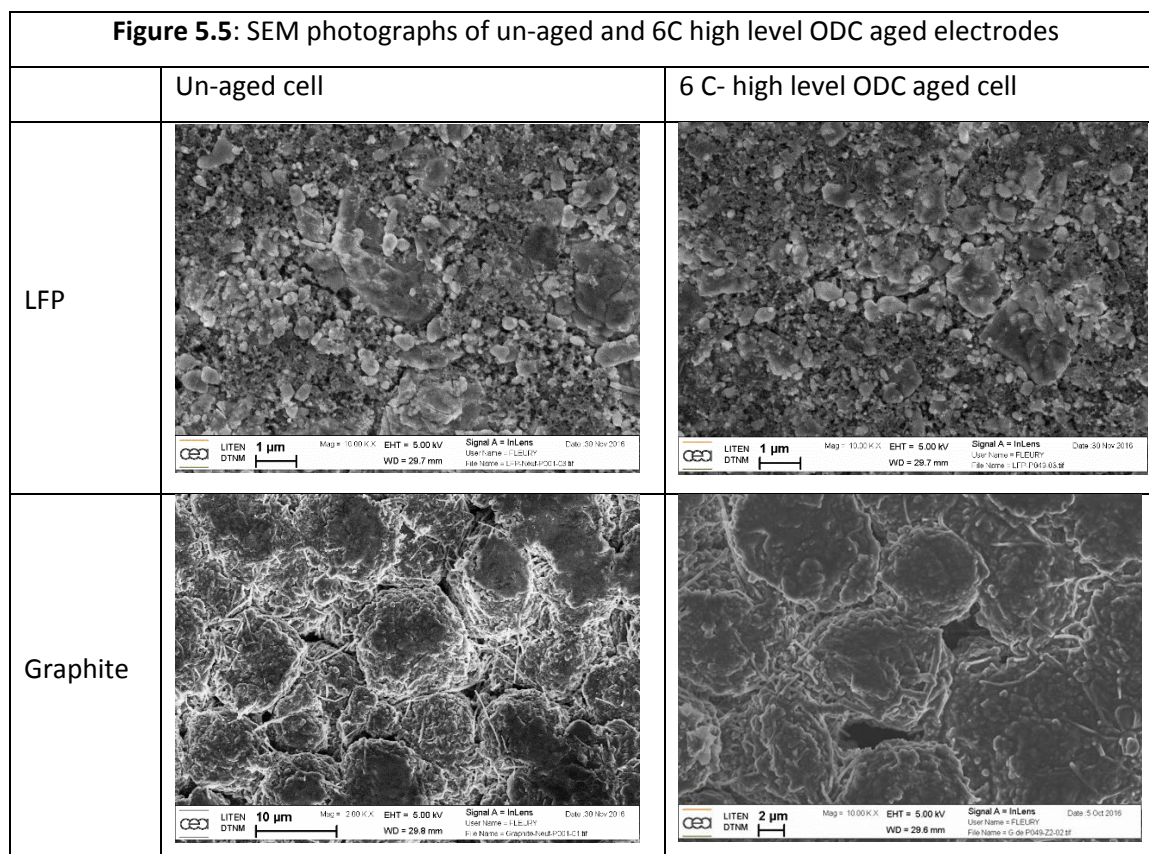


**Figure 5.4:** Visual inspection of the un-aged cell and the 6C-high level ODC aged cell

To go further on the identification of the origin of the deformation observed during the fast charge, the electrodes and the electrolyte were analyzed. The SEM photographs (**Fig. 5.5**) of the un-aged and the 6C-high level ODC aged cells show that there is absolutely no morphological difference. These observations are made in a zone free of white deposit. The size distribution, the shape and the surface aspect are quite similar for both LFP and graphite particles before and after ageing. These observations are substantiated by the XRD analyses made on electrode materials (not shown) which show same diffractometers for LFP and Graphite aged and un-aged electrodes. At the end, no

morphological and structural difference can be observed between aged and un-aged electrodes. No particle cracking or porous material structure degradation is observed during ageing as well as no lithium plating.



#### 4. Post-mortem electrochemical characterisation

Electrochemical tests were performed in coin cell system in order to establish the capacity of the aged and un-aged electrodes. Coin cells are made of harvested electrodes from un-aged and aged cells. Note that the batteries are fully discharged before dismantling. **Table 5.3** presents the delithiation capacity of graphite electrode and lithiation capacity of LFP during the first cycles and the second one. First of all, no significant difference is observed on cycle 2 between un-aged and aged cells. This point is also illustrated through figure 6 and discussed below. The first delithiation of the graphite during the first cycle shows that the negative electrodes are fully discharged before dismantling. Conversely, the first lithiation of the LFP exhibits that the positive electrodes are not fully lithiated. On one hand, the additional lithiation capacity for the un-aged positive electrode

(0.45 mAh) may be related to the SEI formation on the negative electrode at the beginning of life of the battery in normal usage. On the other hand, aged positive electrodes underwent a sharper increase of the additional lithiation capacity (i.e. 0.78 mAh for 45°C standard aged and 0.88 mAh for 6 C- high level ODC aged cell). This higher complementary lithiation capacity may be related to the capacity fade (i.e. 0.33 mAh for 45°C standard aged and 0.43 mAh for 6 C- high level ODC aged cell) due to the charge procedures. A part of Lithium ions amount are likely consumed by parasitic reactions and are no longer available for cycling between the positive and negative electrodes.

**Table 5.3:** Capacities in coin-cell, Li/LFP electrode and Li/graphite electrode

Cycle	Li/LFP electrode Lithiation capacity (mAh)		Li/Graphite electrode Delithiation capacity (mAh)	
	Cycle 1	Cycle 2	Cycle 1	Cycle 2
Unaged LFP electrode	0.45	2.25	0	2.03
45°C standard aged LFP electrode	0.78	2.31	0.01	2.01
6 C- high level ODC aged LFP electrode	0.88	2.24	0.01	1.94

**Fig. 5.6** presents the voltage curves of the un-aged and aged electrodes (Graphite and LFP) face to lithium for the second cycle. Even if aged cells show a significant decrease of their reversible capacities (**Fig. 5.2**) that corresponds to the EoL criteria of 20% of capacity loss (i.e. SOH=80%), no significant reversible capacity decrease can be observed for electrodes themselves (**Fig. 5.6**) considering the cycle 2 in lithiation for positive electrode and in delithiation for negative electrode. Indeed, aged electrodes (LFP and graphite ones) are able to insert or disinsert enough lithium ions to recover their initial capacities. As a consequence, the origin of the full cell capacity fading can therefore be attributed to the loss of lithium inventory (LLI) instead of loss of active materials (LAM) that is indirectly observed. This loss of lithium inventory is probably due to electrolyte decomposition and SEI growth at high cell voltage and/or temperature during fast charge with ODC.

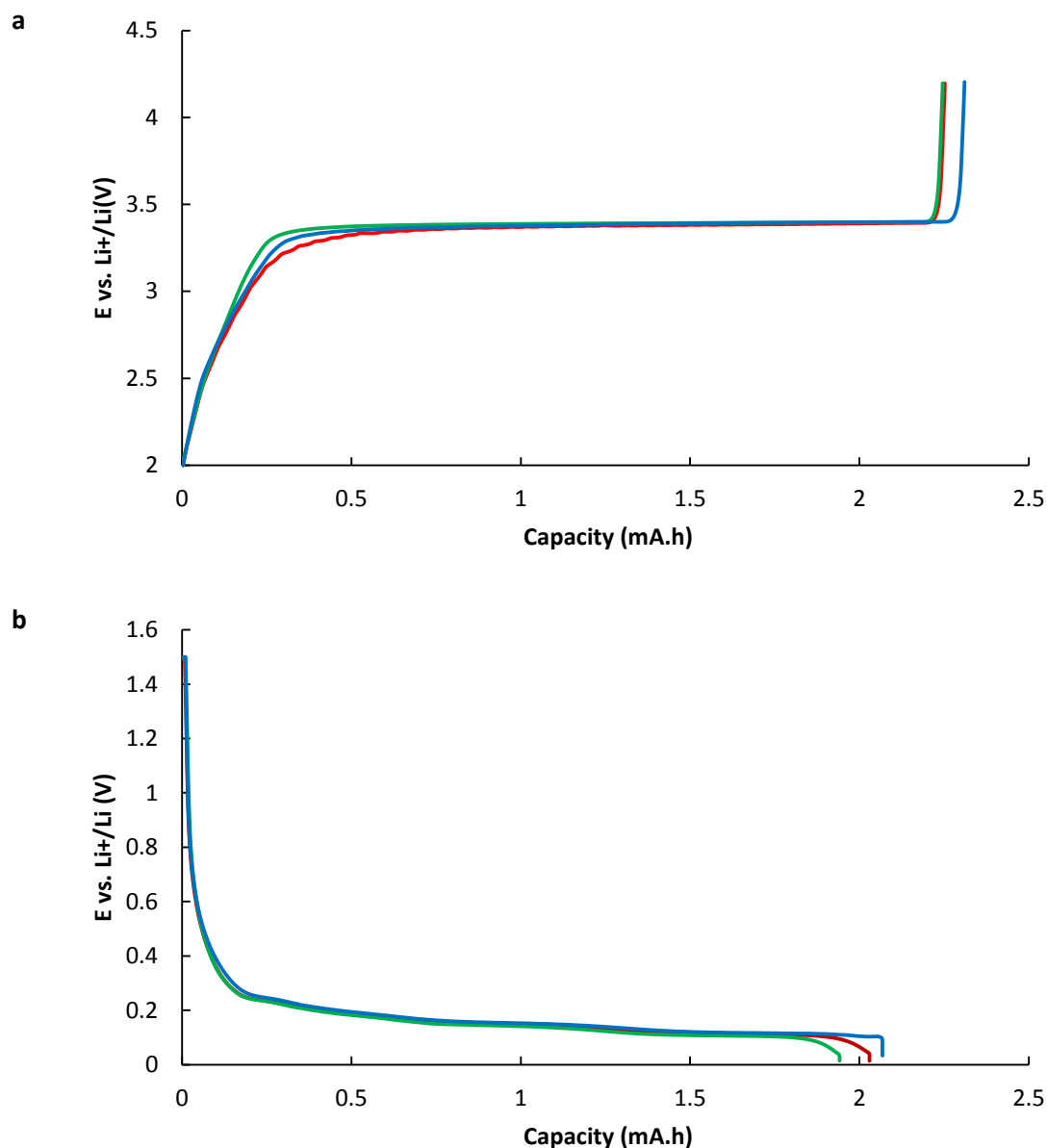


**Figure 5.6:** Capacities of unaged cell (red), 45°C standard aged cell (blue) and 6 C- high level ODC aged cell (green) for half-cells with LFP (a) and Graphite (b) electrodes face to lithium metal.

**Fig. 5.7** illustrates the loss of lithium inventory mechanism accordingly the model proposed by Birkel et al. [18]. **Fig. 5.7a** shows the capacity loss of the electrodes for aged cells as a result of the degradation compared to un-aged cell. The bars symbolise the negative electrode (NE, in blue) and the positive electrode (PE, in red). The areas of the bars represent the electrodes capacities. The golden area represents the cyclable lithium, which corresponds to the cell capacity, in this case intercalated in the PE in a fully discharged cell. The 20% of loss of lithium inventory is illustrated by the shift of the bars to the top **Fig. 5.7a** and the positive electrode potential to the left in **Fig. 5.7b**. This slippage is symbolised in **Fig. 5.7b** by shifting the positive electrode potential (**Fig. 5.6a**) to left subtracting the lithiation capacity measured at the cycle 1 for un-aged and aged cell. It can explain

almost entirely the capacity loss of the cells. It is worth mentioning that the loss of lithium inventory is four times faster for the 6C-high level ODC aged cell than for 45°C standard aged cell (see table 2). This difference may be related to the fact that the cell voltage of the former cell is maintained at high level during a longer time for fast charge with ODC. Thus, further analyses have been carried out on electrolyte of both cells to evaluate their levels of degradation.

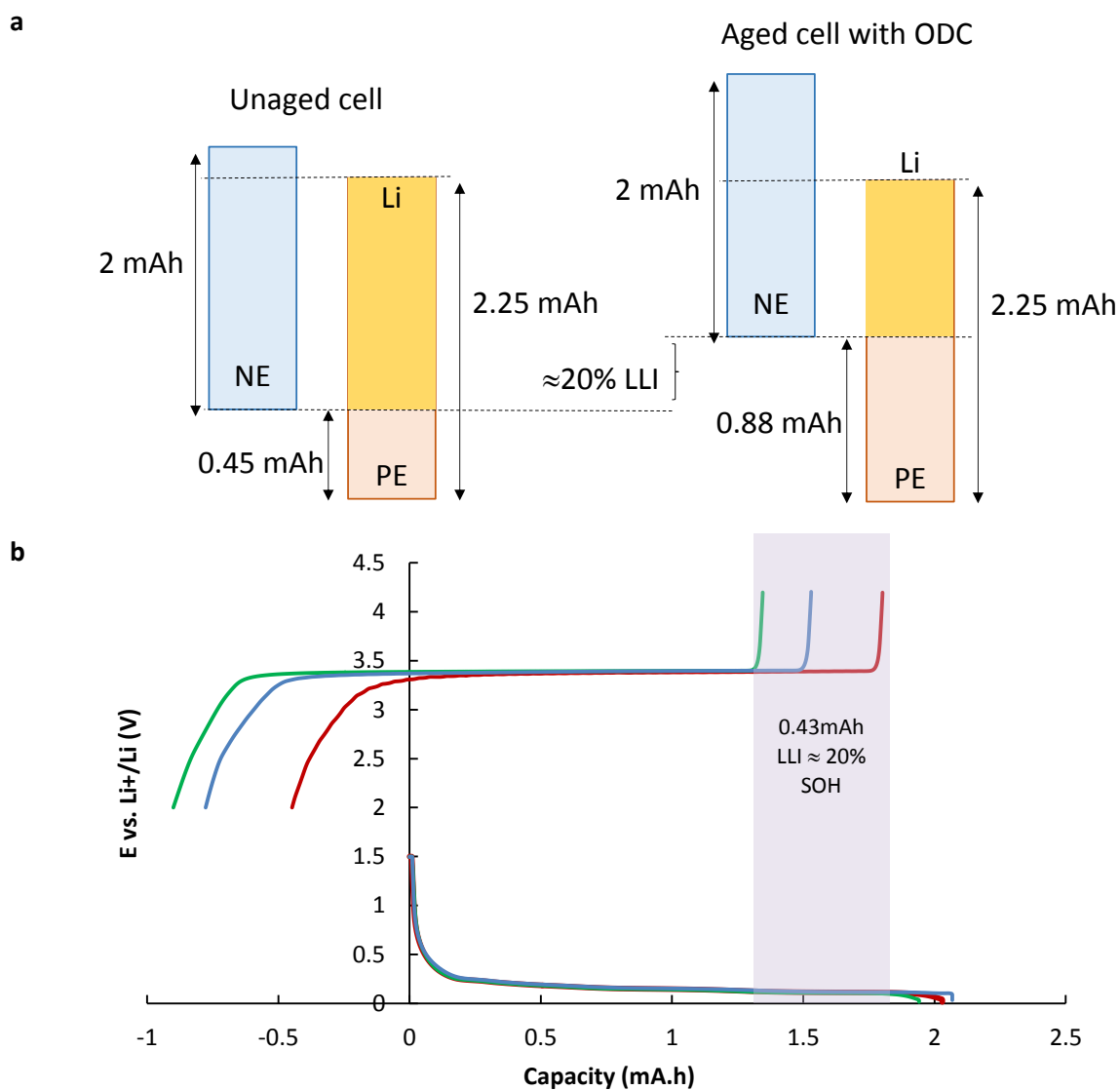


**Figure 5.7:** Simulation of the loss of lithium inventory: (a) Illustration of the electrode utilization as a result of LLI and (b) Electrodes potential for unaged cell —, Electrodes potential for 45°C standard aged cell — and Electrodes potential for 6 C- high level ODC aged cell —.

## 5. Post-mortem analysis of the electrolyte by GC-MS

Electrolyte of the unaged cell, the 6C-high level ODC aged cell and the 45°C standard aged cell has been characterized by GC-MS analysis (**Table 5.4**). The results show that the electrolytes of the 6 C-high level ODC aged cell is more deteriorated than the other ones. Indeed, for this cell, the addition of the amount of degraded products (called DEG: DMDOHC, DEDOHC and EMDOHC) is equal to 10.6% of the amount of EC (%/EC) against 3.6%/EC for the 45°C aged cell and 2.7%/EC for the unaged one. It is well-known that all these compounds are the degradation products of the electrolyte solvents. It is important to note that the amounts of these degradation products are given comparatively to the amount of EC because no calibration of these species is possible in GC-MS. Furthermore, DEC is known as another degradation product coming from the decomposition of other solvents. The same trend can be observed for the amount of this compound which increases up to 1.7% for the 6C-high level ODC aged cell against 0.6% for the 45°C standard one and 0% for the unaged one. These values do not include the salt degradation (DEGSALT) amount because the GC-MS induces an uncertainty on these values because of the vaporisation of the electrolyte for the analyses which deteriorate the salt.

**Table 5.4** : GC-MS analysis of electrolyte

	Un-aged		6 C- high level ODC		45°C standard	
	%	%/EC	%	%/EC	%	%/EC
EC	68.8		68.5		63.0	
PC	15.2		16.9		14.8	
DMC	6.3		6.1		8.4	
EMC	9.7		6.9		13.2	
DEC	0.0		1.7		0.6	
DEGSALT		1.9		1.1		1.2
DEG		2.7		10.6		3.6

The observation of degradation products (DMDOHC, EMDOHC, DEDOHC) for the aged cell at 6C-high level ODC is concomitant with both high cell voltage (>3.65V) and high temperature (>45°C). In contrast, less degradation product are measured for aged cell at 45°C in standard condition. These latter results confirm that electrolyte components oxidation at high potential and temperature higher than 45°C leads to the formation of gas bags which can cause deformation of the battery winding and, finally, a decrease in the performance.

## 6. Conclusion

The development of fast charging method for lithium batteries remains a key point of their deployment. Saving the charging time can be damaging to the life of the battery. Indeed, fast charging with ODC induces accelerated capacity fade due to degradation mechanisms at high cell voltage and temperature. Namely, this study showed that the internal temperature of the battery could reach levels above 50°C, in the worst case (i.e. fast charge with a high level of compensation). Based on post-mortem analysis, the formation of gas pockets in the jelly-roll has been observed and correlated with degradation of the electrolyte. Postmortem analysis allow the exclusion of both active materials degradation and show that the capacity fade is only caused by the loss of lithium inventory, which may be related to the electrolyte and binder decomposition at high temperature and cell voltage. Moreover, SEI decomposition and growth can be also involved. So, the lithiated graphite electrode reactivity towards the electrolyte is reinforced at low potential leading to the consumption of exchangeable lithium ion and the decrease the cell capacity. In this mechanism, Lithium ions are consumed by parasitic reactions and are no longer available for cycling between the positive and negative electrodes. Nonetheless, at 6C with a low level of ODC, a good compromise between charging time and life cycle can be achieved.

## 7. References

- [1] S.S. Zhang, K. Xu and T.R. Jow, A thermal stabilizer for LiPF<sub>6</sub>-based electrolytes of Li-ion cells, *Electrochemical and solid-state letters*, 5(9)(2002), pp. A206 - A208.
- [2] N. Nagasubramanian, Comparison of the thermal and electrochemical properties of LiPF<sub>6</sub> and LiN(SO<sub>2</sub>C<sub>2</sub>F<sub>5</sub>)<sub>2</sub> salts in organic electrolytes, *Journal of power sources*, 119(2003), pp. 811 - 814.
- [3] J. Garche, C. K. Dyer, P. T. Moseley, Z. Ogumi, D.A. J. Rand and B. Scrosati, *Encyclopedia of Electrochemical Power Sources, Secondary Batteries - Lithium Rechargeable Systems/ Electrolytes: Nonaqueous*, Elsevier Science (2009), pp. 80 - 81.
- [4] G. S. Popkirov, A technique for series resistance measurement and ohmic-drop correction under potentiostatic control, *Journal of Electroanalytical Chemistry*, 359(1-2)(1993), pp. 97 - 103.

[5] C. H. Lin, C. L. Chen, Y. H. Lee, S. J. Wang, C. Y. Hsieh, H. W. Huang and K. H. Chen, Fast charging technique for Li-Ion battery charger, IEEE International Conference on Electronics, Circuits and Systems, (2008), pp. 618-621.

[6] C. H. Lin, C. Y. Hsieh, K. H. Chen, A Li-Ion Battery Charger With Smooth Control Circuit and Built-In Resistance Compensator for Achieving Stable and Fast Charging, IEEE Transactions on Circuits and Systems - I: Regular Papers, 57(2)(2010), pp. 506-517.

[7] R. Saint-Pierre, A Dynamic Voltage-Compensation Technique for Reducing Charge Time in Lithium-Ion Batteries, IEEE The 15<sup>th</sup> Annual Battery Conference on Applications and Advances, (2000), pp. 179 - 184.

# General conclusion

---



## General conclusion

The objective of this thesis consists of the studies of fast-charging Lithium-ion battery with ohmic-drop compensation (ODC) method intended for electric vehicles. To achieve this objective, the understanding of that particular method regarding the total charging time, thermal behavior and also ageing mechanism is essential.

For this purpose, first, a literature review has been carried out concerning different types of lithium-ion battery technologies and other fast-charging method to comprehend the basics of fast-charging. The most suitable battery technologies for electric vehicle utilization are the lithium-ion batteries thanks to their higher density of energy. Furthermore, most of the studies concerning fast-charging methods were implemented onto lithium-ion technologies.

There are many ways to achieve fast charging. There are pulsing current method, multistage current method, high C-rate method, the ODC method and many more. All of these methods have their advantages and inconvenients. In this thesis, the ODC method was implemented on three different types of 18650 battery cells. These batteries are C/LFP, C/NMC and LTO/LFP. Each battery has its own characteristics and the most notable differences between them are their positive and negative electrode materials. As shown in this work, C/LFP and LTO/LFP batteries perform really well during ODC fast-charging method implementation as the total charging time was reduced significantly. Notably, a reduction of total charging time of about 70% in comparison with the classical method was observed. However, it is not the case for C/NMC where the ODC method has no considerable impact in term of charging time. A preliminary conclusion was that the ODC fast-charging method would only work on lithium-ion batteries which present a plateau or a flat voltage response during charging process.

With that, some further studies had been executed on C/LFP batteries to understand the thermal effect and also the ageing mechanism of the ODC method. As revealed by other studies, the main drawback of fast-charging methods is the high temperature elevation during their implementation. Moreover, the internal temperature of a battery cell is hard to measure. So, many researchers turned to numerical simulation method strategy for a solid prediction of internal temperature, including us.

Internal temperatures of the battery when using the ODC method is the key to understanding the capacity fade, hence the ageing mechanism. Indeed, the C/LFP battery aged a lot faster when underwent the charging/recharging cycle using the ODC method compared to the reference cycle. The same situation was also observed for the reference cycle at 45°C which endured just about twice more compared to ODC method cycle. So, the internal degradation related to high temperature is one of the main culprits for lithium-ion battery ageing. However, other factors such the parasitic/side reactions cannot be ruled out as shown in the post-mortem analysis performed in this work because of high cell voltage at the end of charge. These factors induce the loss of lithium inventory (LLI) for this battery technology.

In conclusion, the ODC fast charging method is one of many other fast charging protocols that could be implemented onto electric vehicles. This method by no means, is to replace or to diminish other fast-charging methods but in contrary, it is a really good complementary and alternative for the existing fast charging methods to be used in the automotive sector principally. However, this thesis is just the tip of the iceberg regarding the potential of this ODC method. Indeed, up until now, this method has just been studied on a single battery cell level and a lot of information can be acquired from that alone. In perspective, it would be interesting to further this study more deeply in the several following directions:

- Exploring other types of lithium-ion batteries technologies,
- Further evaluation of this ODC method on a battery-pack level,
- To use more advance battery cycling protocol where it reflects the daily use of an electric vehicle,
- To combine ODC method with other potential fast charging method into one charging protocol (ex: Multistage + ODC method...),
- Further studies for a better understanding of this ODC method at low temperature (i.e. winter weather).



## Abstract

The aim of this thesis is to study fast-charging of lithium-ion, battery using the ohmic-drop compensation (ODC) method. The latter method theoretically will reduce the total charging time of the batteries considered. In this thesis, the ODC method was implemented on three different types of 18650 battery cells. These batteries are C/LFP, C/NMC and LTO/LFP. This method shows a good result for C/LFP and LTO/LFP batteries with a reduction of total charging time of about 70% in comparison with the classical method. Nevertheless, there are some issues regarding this method; the temperature elevation of the battery is high during fast-charging. Indeed, almost all fast-charging procedure experiences the same problem concerning that matter. Moreover, with ODC fast-charging method, high current rate and high voltage worsen the situation. Regarding the ODC fast-charging method, both performance and durability of the batteries are key points in this study. Particularly, we have demonstrated that C/LFP battery underwent internal degradation as a mechanical deformation of the active materials and degradation of electrolyte.

## Résumé

L'objectif de cette thèse est l'étude de la charge rapide de batteries lithium-ion basée sur la méthode de la compensation chute ohmique. Cette méthode permet théoriquement de réduire le temps total de charge des batteries. Dans cette thèse, cette méthode a été mise en œuvre sur trois types différents de cellules de format 18650 : C/FP, C/NMC et LTO/LFP. Cette méthode montre de bons résultats pour les batteries C/LFP et LTO/LFP avec une réduction du temps de charge total d'environ 70% par rapport à la méthode classique. Néanmoins, cette méthode présente des inconvénients comme notamment l'élévation de la température interne de la batterie pendant la charge rapide. De plus, cette méthode implique un courant élevé et conduit à des potentiels élevés qui peuvent engendrer également des dégradations. En particulier, nous avons démontré que la batterie C / LFP subissait des dégradations internes notamment une déformation mécanique de l'enroulement et une dégradation de la composition d'électrolyte.

---